Failure of Cerebral Aneurysms and Arterial Tissues

by

Chao Sang

B.S., Southeast University, 2013

M.S., University of Pittsburgh, 2014

Submitted to the Graduate Faculty of the

Swanson School of Engineering in partial fulfillment

of the requirements for the degree of

Doctor of Philosophy

University of Pittsburgh

2020

UNIVERSITY OF PITTSBURGH

SWANSON SCHOOL OF ENGINEERING

This dissertation was presented

by

Chao Sang

It was defended on

September 18, 2020

and approved by

Spandan Maiti, Ph.D., Associate Professor, Department of Bioengineering, Department of Mechanical Engineering and Materials Science

Sachin Velankar, Ph.D., Associate Professor, Department of Chemical Engineering

William S. Slaughter, Ph.D., Associate Professor, Department of Mechanical Engineering and Materials Science

Dissertation Director: Anne M. Robertson, Ph.D., Professor, Department of Mechanical Engineering and Materials Science

Failure of Cerebral Aneurysms and Arterial Tissues

Chao Sang, PhD

University of Pittsburgh, 2020

A cerebral aneurysm (CA) is most commonly a saccular enlargement in the wall of a cerebral artery. Aneurysm rupture is associated with high morbidity and mortality and hence there is a pressing need to better understand the disease progression and rupture mechanisms. Clinically useful metrics for assessment of rupture risk can be identified based on this information.

Accurate measurements of mechanical properties of arterial tissues is essential for rupture risk assessment and development of more realistic mathematical models. Although uniaxial tensile testing is commonly used to evaluate failure properties of vascular tissue, there is no established protocol for specimen shape or gripping method. We developed a new uniaxial testing approach that can achieve consistent failure in the mid-region of small specimens, even for vessels from older individuals and small cerebral aneurysm tissues and used this approach to analyze the failure process in human cerebral and sheep carotid arteries.

Collagen is the major passive load bearing component in arteries including cerebral artery and aneurysmal walls. To maintain a sustainable level of intramural loads and avoid rupture, the collagen fabric must adapt in response to the temporally evolving cerebral aneurysm geometry. To study the remodeling of collagen structure during disease progression as well as its role in failure of arterial tissue, 22 elastase-induced rabbit aneurysms were studied using multiphoton microscope (MPM) imaging and mechanical testing. The results were also compared to human aneurysm data.

Inclusions such as calcification can affect the stress distribution and strength of arterial walls. The role of calcification in failure of cerebral arterial tissues remains unknown. The high

prevalence of calcification in cerebral aneurysms has been shown previously. To better understand the role of calcification in cerebral arterial tissues, the prevalence of calcification in cerebral arteries was investigated. A methodology was developed and preliminary data obtained to analyze the interaction between collagen fibers and calcification during mechanical loading.

Table of Contents

List of Tables

List of Figures

Preface

I would like to express my deepest gratitude to my advisor Dr. Anne M. Robertson for her continued support and guidance throughout this research work. She is a great scientist and an exceptional mentor. Her creativity, enthusiasm and a wealth of knowledge have always been inspiring me. I am grateful to another lesson I learned from her: always focus on the positive side and make the positive efforts.

I would like to thank my committee members, Dr. Spandan Maiti, Dr. Sachin Velankar, Dr, William Slaughter for their guidance and insightful comments.

My sincere thanks also go to our collaborators. Dr. Maiti and Ronald are always ready to help and have provided great insight on computational approaches. Dr. Kallmes and Dr. Kofler provided the samples used in this study and Dr. Watkins provided technical support for microscopic imaging.

I am grateful to my fellow lab mates, Xinjie, Fang, Piyusha, Yas, Ron, Mike, Sarah, Mehdi, Ricardo and Eliisa, for their collaborations, help, stimulating discussions and fun we have had in the last few years. It was a wonderful experience to work with them. I would also like to thank Deb for her patience, kind help and delightful talks. I also wish to acknowledge Patrick for his diligence and passion. I wish to thank Mehdi and Ronald for the collaborative efforts in the last Chapter.

Lastly, but by no means least, I would like to thank my parents for their tremendous support, love and encouragement. They motivated me to pursue my own value and helped me to get stronger after every setback.

I am indebted to all the love, support and joy I received along the way.

1.0 Introduction

An intracranial aneurysm (IA) is a focal dilatation in the wall of a cerebral artery that is generally saccular in shape. Although aneurysms may remain stable for years, there are a small percentage that rupture during the fifth to seventh decades of patient life [1]. The rupture rate of IAs is estimated to be 1.3% per year [1] and rupture can lead to subarachnoid hemorrhage which is associated with high rates of morbidity and mortality (40-65%) [2]. Current treatment for IAs majorly focuses on isolating the aneurysm wall from the circulation. Theses treatment strategies include placing mechanical clips at the neck, inserting coils into the aneurysm sac and other endovascular procedures. As risks associated with current treatments are substantial, there is a pressing need for improved treatment and risk assessment.

Current risk assessment mainly depends on aneurysm size. However, the limitation of this approach is that most ruptured aneurysms are smaller than the critical size, 7 mm [1,3,4]. Hence, size is insufficient for risk stratification. Other factors, such as aneurysm location, irregularity of geometry, alcohol consumption, cigarette smoking, are also used to assess the risk of rupture [5–9]. A confounding factor of most risk assessment approaches is that they use the characteristics of ruptured aneurysms as features of high risk unruptured aneurysms. Moreover, uses a binary approach to categorizing aneurysms as either ruptured (high risk) or unruptured (low risk). This single categorization of unruptured aneurysms is clearly not ideal, as even unruptured aneurysms display substantial heterogeneity in wall structure. For example, three different types of walls with great variability were found in unruptured aneurysms based on cellular content and structure [10] and a range of collagen fiber architecture was also reported in unruptured aneurysms [11,12]. This simple approach to assessing risk is unavoidable to some degree due to the dearth of clinical data

tracking patients over time from prerupture to rupture. However, some recent work has looked at aneurysm growth [13–16] and the formation of blebs on the aneurysm wall [17–19] as a method of assessing risk distinctly from rupture.

The strength of aneurysm walls has been directly evaluated recently [11,20,21]. Instead of using rupture status, non-binary wall strength was included to identify aneurysm characteristics, such wall geometry and hemodynamics. It is critical to have knowledge of the temporal nature of changes of the wall during aneurysm progression and the diverse physical causes of diminished wall strength. It is vital to have such information for developing effective metrics for risk assessment and novel treatments to stabilize the aneurysm or strengthen the wall. It is well accepted that mechanical factors have fundamental roles in the rupture of aneurysms and rupture occurs where the local stress level exceeds the wall local strength. However, the underlying failure mechanism of cerebral aneurysms still remains unknown.

The mechanical properties of cerebral arterial tissues, both healthy and pathological, are needed for evaluating wall integrity as well as understanding the effects of pathologies. Uniaxial tensile testing is a common approach to evaluate failure properties of vascular tissues as well as other soft tissues. Ideally, specimens should fail in the middle section to avoid the confounding clamp-related artifacts. Additionally, with consistent midregion failure, studies can be designed to image the sample during failure testing for even small vascular samples. Such studies would provide valuable quantitative information about changes to collagen and elastin structure during the failure process. However, there is no established protocol for specimen shape or gripping method, especially for small specimens from cerebral arterial tissues.

The passive mechanical response of cerebral arterial tissues is largely determined by the properties and organization of the elastin and collagen fibers within the wall. Elastin fibers are

highly elastic and engaged to load bearing during the low stiffness toe region of the loading curve for healthy arteries. Their great extensibility enables the vessel to return to its original state under cyclic loading. In contrast, collagen fibers are generally in an unloaded wavy state at low loads and engage in load bearing only at the end of the toe region of the loading curve. Collagen fibers are stiffer and stronger than elastin fibers. In contrast to cerebral arteries, elastin is nearly always absent in IA walls and in fact, the loss of elastin is considered an early event in aneurysm formation. Therefore, the stiffness, strength, and organization of the collagen fibers are critical in defining the failure properties of arteries. During the progression of cerebral aneurysms, the geometry of the arterial wall changes in time, generally increasing in diameter. In order to maintain a sustainable level of intramural loads and avoid rupture, the collagen fabric must therefore also adapt in time. This can be seen even from a simple force balance using the Law of Laplace.

Although collagen remodeling is a key factor in understanding the evolution of strength of the arterial wall and determining rupture risk such as intracranial aneurysms, few studies have directly evaluated the collagen fibers or their architecture in IAs [11]. As a result, many fundamental questions remain unanswered that are important for evaluating the capacity of an IA. While intracranial aneurysm tissue can be harvested following treatment by surgical clipping and have provided valuable information about the heterogeneity in the wall among patients. A challenge is that harvested aneurysms tissue can only represent one time point in the progression of the disease. Animal models for IAs provide a means of studying multiple time points in disease progression. The temporal data provided by studies with animal are crucial for understanding the effective or ineffective remodeling process.

Moreover, the strength of aneurysm wall, i.e., the ability of the aneurysm wall to bear load, can be impacted substantially by physical inclusions such as calcifications and lipids. For example,

calcification can cause local stress concentrations and affect the mechanical stiffness of the wall. However, our prior work has demonstrated that calcification displays a wide range of sizes, morphology and location, as well as physical relationship to the collagen fibers. The role of calcification in failure of cerebral arteries as well as aneurysms remains unknown. While the prevalence of calcification in IAs was reported to be between 1.7 to 29% [22–24], a recent study from our group reported a much higher prevalence (78%) of calcification in IAs [25]. The lower prevalence reported in the earlier studies is likely due to the lower resolution on the clinical computed tomography (CT), with typical voxel resolution between 250 μm to 300 μm. In contrast, the resected human aneurysm tissues were scanned by a high resolution micro-CT scanner with a resolution of 3 μm. In this more recent, high resolutions study, ruptured IAs were found to have a lower calcification fraction with only nonatherosclerotic micro and meso-calcification compared to unruptured cases. This finding suggests larger calcifications could play a protective role. However, it remains unclear whether the increased prevalence of calcification develops as part of the pathology of IAs, or whether the high prevalence is already present in the wall of the cerebral vessels. The answer to this question can help us to better understand the role of calcification in the rupture of aneurysms.

The overall objective of the current study is to determine the failure properties of cerebral arteries and understand the various types and causes for this failure. This objective was further broken down into the following three aims:

1. **Develop a uniaxial testing approach for consistent failure in the middle of small specimens, even for arteries from older individuals**

Different gripping methods and specimen shapes were tested on both sheep carotid arteries and human basilar arteries. Dogbone shaped specimens with soft grips can achieve midsample

failure in 94% of the specimens of only 6 mm in length. In addition to assessing rupture location, failure modes were evaluated and the mechanical response curves were also analyzed and classified.

2. Understand how the collagen fibers remodel during aneurysm progression

To study the evolution of collagen during aneurysm progression, 22 elastase-induced rabbit aneurysm samples at four different time points after creation were included. Multiphoton microscope imaging was used to study the collagen structure and elastin content. Uniaxial and biaxial testing systems compatible with MPM enable the evaluation of collagen during the loading process. The mechanical properties and failure strength of aneurysms and control arteries were assessed by uniaxial testing using the same approach as described in Chapter 1. These results were also compared with human aneurysms.

3. Investigate the prevalence of calcification in human cerebral arteries and identify the relationship between calcification and collagen fibers

To achieve this specific aim, 20 internal carotid artery (ICA) segments from different individuals were scanned using high resolution micro-CT with a resolution of 3 μm. The calcifications and lipids were identified after 3D reconstruction of CT scanning. Their size and location distributions were analyzed and then compared with results from human aneurysms. The relationship between calcification and collagen fibers was then studied in several cerebral arteries stained with Osteosense solution and imaged under Multiphoton microscope.

2.0 A Uniaxial Testing Approach for Consistent Failure in Vascular Tissues

The work in this chapter was largely reproduced from the following manuscript [26] with permission granted by American Society of Mechanical Engineers (ASME):

Sang, C., Maiti, S., Fortunato, R., Kofler, J., and Robertson, A. M., 2018, "A Uniaxial Testing Approach for Consistent Failure in Vascular Tissues," *Journal of Biomechanical Engineering*, **140**(6), p. 061010.

2.1 Introduction

Mechanical failure of vascular tissues, such as rupture of abdominal aortic aneurysms and cerebral aneurysms, arterial dissections and cerebral vessel damage due to head injury, can cause severe health issues or even death [27–32]. Accurate measurements of mechanical properties and an understanding of the failure process itself are vital for improving diagnostic tests and treatment of these diseases. Uniaxial tensile testing is a common approach to evaluate failure properties of vascular tissue as well as other soft tissues. In such tests, both rectangular and dogbone specimens (also known as I-shaped and dumbbell shaped specimens) are widely used, as are an array of clamping methods, Table 1. Even though sample geometry and clamping methods are known to influence the stress and strain distribution within the sample, there are currently no clear guidelines for selecting sample geometry or clamping methods for vascular tissues during uniaxial testing.

Table 1 Uniaxial failure testing methods and clamp failure data for arterial tissue from representative published work

Study	Species	Tissue	Sample shape	Unclamped sample size (mm)	Clamping method	Quantity failed at clamp
Claes et al. [33]	Human	Coronary artery	Rectangle	7×1	Grip with cyanoacrylate glue	NF
Holzapfel et al. [34]	Human	Coronary artery	Rectangle	(7.21±1.21) ×(2.81±0.38)	Sandpaper with super-adhesive gel	Majority
Pichamuthu et al. [35]	Human	Ascending thoracic aortic aneurysm	Rectangle	NF	Sandpaper with cyanoacrylate glue	8.4% (15 out of 178)*
Raghavan et al. [36]	Human	Abdominal aortic aneurysm	Rectangle	40×10	Uneven clamp with glue	11.4% (10 out of 88)*
Raghavan et al. [37]	Human	Abdominal aortic aneurysm	Rectangle	Width: 4	NF	22% (32 out of 145)
Robertson et al. [11]	Human	Aneurysm, basilar and carotid artery	Rectangle	Minimum: 5×4	Clamp with fine-grade sandpaper	NF
Teng et al. [38]	Human	Atherosclerotic carotid artery	Rectangle	(9~15)×2	Rubber coated grips with sandpaper using super glue	37% (27 out of 73)
Vorp et al. [39]	Human	Aortic tissue	Rectangle	30×8	Clamp with cyanoacrylate glue	NF
Ferrara et al. [40]	Human	Dilated ascending aorta	Dogbone	NF	Fine grit sandpaper with super-adhesive gel	39% (160 out of 407)**
Forsell et al. [41]	Human	Abdominal aortic aneurysm	Bone	Length: 10~27 (neck: 4)	sandpaper with super-adhesive glue	20% (3 out of 15)
García-Herrera et al. [42]	Human	Ascending aortic tissue	Dogbone	18×5 (neck: 2)	Grip with cyanoacrylate glue	NF
Mohan and Melvin [43]	Human	Mid-thoracic descending aorta	Dumbbell	57.15×19.05 (neck: 6.35) 31.23×12.7 (neck:4.57)	Low-mass air-piston grips	5.3% (2 out of 38)*
Okamoto et al. [44]	Human	Dilated ascending aorta	Dumbbell	35×10 (neck: 4)	Sandpaper	NF
Korenczuk et al [45]	Porcine	Abdominal aorta	Dogbone	10×5 (neck: 3)	NF	NF
Stemper et al. [46]	Porcine	Aorta	I-shaped	NF	NF	NF
Shah et al. [47]	Swine	Ascending thoracic aorta	Dogbone	20×5	NF	28%

Failure location was frequently not found (NF) in the publication. In some cases, clamp failure was reported in a group with other testing artifacts. These cases are denoted by *Failed at clamp or slipped from grips, **Failed near clamp, slipped from grips, or low quality of the stress-strain curve.

For uniaxial failure testing of rubber-like materials, the ASTM standard recommends dogbone shaped samples with long central regions where the stress field is relatively homogeneous and higher in magnitude, enabling consistent failure away from the grips [48]. Such long mid-regions are often impossible to achieve in vascular tissues due to insufficient sample length, or because the tissue is highly heterogeneous and so the region of interest is relatively short. The grips of tensile testing machines create stress concentrations and can even damage the specimen in the neighborhood of the clamped region [49–51] causing failure at the clamps even for samples where the mid-region is long, Table 1. To date, a protocol for uniaxial testing of vascular tissues with consistent failure away from the clamping region, has yet to be established.

Currently, some studies exclude data from specimens that failed at the clamps to avoid confounding the data with grip related artifacts while others pool data regardless of failure location, Table 1. Often, no information is given about inclusion/exclusion of such samples. While the more cautious approach would seem to be preferable, this can result in substantial waste of tissue samples, Table 1. Furthermore, failure at the grips precludes imaging of the tissue at the failure location during mechanical testing. If failure in the middle of the sample could be achieved consistently, the structural basis of failure could be analyzed using imaging modalities such as multiphoton microscopy [52].

The objective of the current study is to identify clamping conditions and sample geometry that can achieve consistent failure in the middle of small specimens, even for arteries from older individuals. We conjecture that dogbone shaped specimens with a short midsection, combined with soft grips can achieve this objective. To test this hypothesis, we assessed failure location during uniaxial testing of dogbone specimens from human cerebral and sheep carotid arteries using soft inserts between the grip face and tissue sample. For comparison with commonly used protocols

for uniaxial testing, we also tested two groups of rectangular shaped samples- those with sandpaper inserts and others with soft inserts. In addition to assessing rupture location, failure modes were evaluated (e.g. delamination, necking, cracking) and the mechanical response curves were also analyzed and classified.

In this work, extremely small samples of only 6 mm in length were chosen, motivated by the need to develop effective failure testing protocols for cerebral arteries, cerebral aneurysms and other small tissue samples. Successful testing protocols for small samples are not only valuable in situations where larger specimens are unavailable, but will also enable multiple specimens to be tested from a single larger specimen as needed for measurements of anisotropic material properties and also for studies of highly heterogeneous tissues.

2.2 Methods

2.2.1 Sample Acquisition

Human basilar arteries from five circles of Willis without severe visible calcification or atheroma were included in this study (Alzheimer's Disease Research Center Brain Bank, University of Pittsburgh) that were obtained post mortem using protocols approved by the Committee for Oversight of Research and Clinical Training Involving Decedents (CORID). The average subject age was 73.6 ± 4.3 years. Following harvest, the circles of Willis were snap frozen to -80˚C and then stored at -20˚C. Prior to testing, the circles were thawed at 4 ˚C for 24 hours, after which the basilar arteries were harvested. The average post mortem interval was 9.5 hours.

Three carotid arteries were harvested from 7-month old (juvenile) female sheep (Suffolk and Dorset sheep), stored in PBS at 4˚C after harvest and tested within 72 hours of sacrifice. Sheep arteries were provided for this study in compliance with protocols approved by the Institutional Animal Care and Use Committee (IACUC) of the University of Pittsburgh following NIH guidelines for the care and use of laboratory animals.

2.2.2 Study Population

Three test groups were considered for both the human basilar arteries and sheep carotid arteries, i) **DB-FT**: Dogbone shape specimens with a foam tape insert (n=17); ii) **Rect-FT**: Rectangular shaped specimens with a foam tape insert (n=11); and iii) **Rect-SP**: Rectangular specimens with a sandpaper insert (n=11). To facilitate discussion of the results, within a single tissue type (sheep carotid, human basilar), each specimen was given a numeric identifier (sample number).

2.2.3 Specimen Preparation

In preparation for uniaxial testing, arteries were cut open along the long axis of the vessel, Figure 1(a). Then, rectangular strips approximately 6 mm long and 2.4 mm wide were cut from the flayed vessel, with long axis aligned in the circumferential direction, Figure 1(b,c). Arterial regions with branch arteries and other visible non-homogenous factors such as plaque were avoided. For dogbone shaped samples, an additional step was added whereby a circular die (4.5mm in diameter) was used to mark an arc on each side of the rectangular strip such that the width of the middle region was approximately 1.2 mm. This arc was then excised using a #15 scalpel under

a dissecting scope, Figure 1(d). Prior to mechanical testing, wall thickness and width were measured at three positions in the mid-region of the unloaded sample using a 0-150 mm digital caliper (Marathon watch company Ltd) and then averaged.

2.2.4 Mechanical Testing

All rectangular and dogbone specimens were mechanically tested to failure using a custom-built uniaxial tensile testing system with displacement control [52], Figure 1 (e-g). Briefly, tissue specimens were held between metal grips located within a bath filled with 0.9% (w/v) saline at room temperature, Figure 1(g). Prior to loading, insert materials (sandpaper or foam tape) were attached to the face of the metal clamps to prevent slippage of the specimen during loading, Figure 1(f). Sandpaper inserts were glued to the grip face (Loctite 414, Henkel) prior to clamping the specimen. The adhesive on the foam tape (7626A213, Multipurpose Foam Tape, McMaster-Carr) was fixed to the face of the clamp and a few droplets of the same glue were applied between the sample and insert materials.

After mounting, samples were preconditioned with three cycles to 20% extension and then tested to failure. The zero strain configuration was defined as the sample configuration under 0.005 N load. To approximate quasi-static deformation, displacement of the left grip was set at 20 μm/s using a high performance linear actuator (ANT-25LA, Aerotech Inc, Pittsburgh, PA) with simultaneous force measurements obtained using a 5 lb load cell (MDB-5, Transducer Techniques, Rio Nedo Temecula, CA), Figure 1(B). Images of the tissue were recorded using a high resolution CMOS camera mounted above the uniaxial system (EO-5012C, Edmund Optics, Barrington, NJ) at a frame rate of 1 fps with a pixel size of 2.2 microns, Figure 1(D).

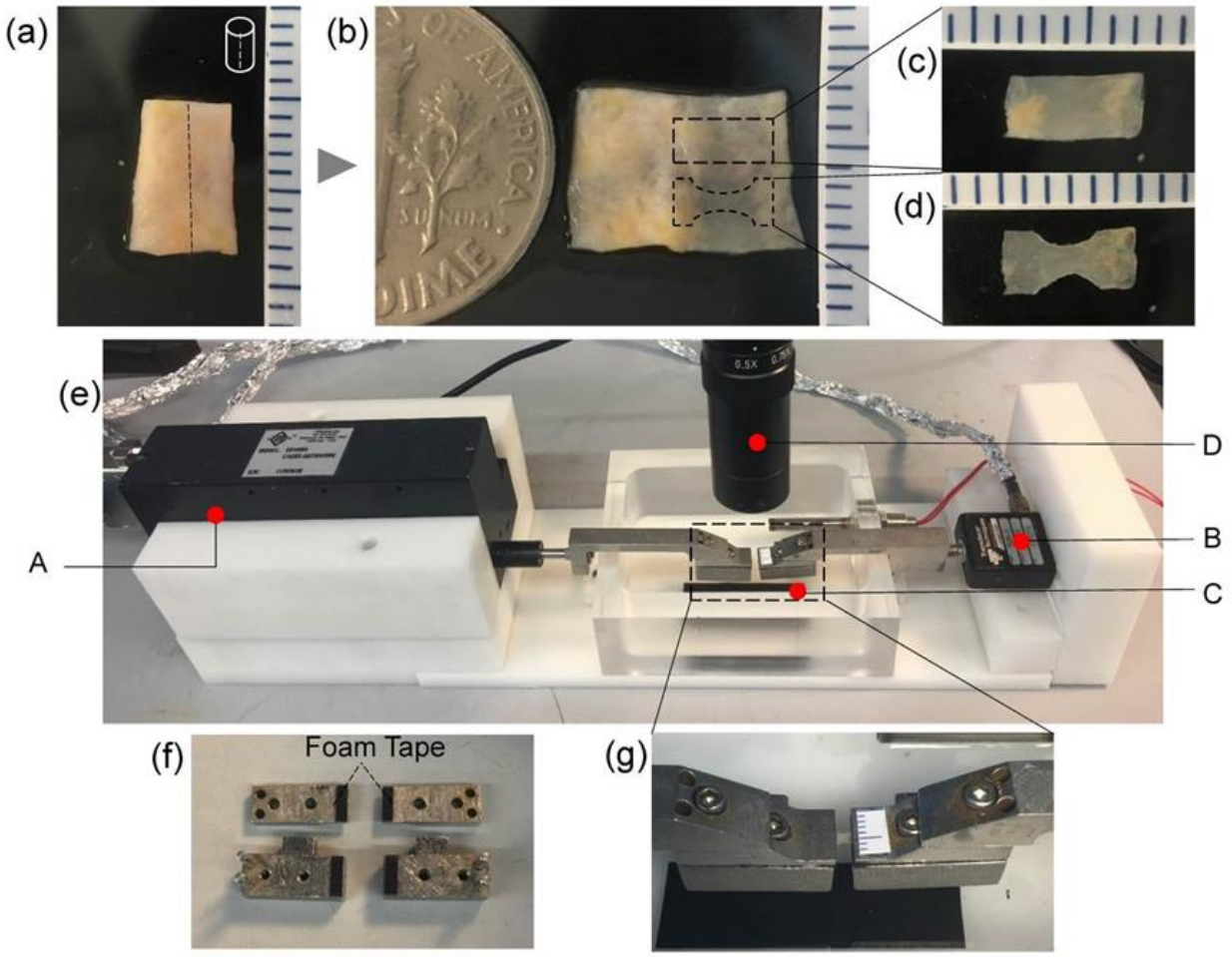

Figure 1 Sample preparation and experimental setup for failure testing. (a) Arterial segment, (b) Sample opened longitudinally with schematic of dogbone and rectangular shaped specimens, (c) Rectangular specimen, (d) Dogbone specimen, (e) Custom mechanical testing system with (A) linear actuator, (B) the load cell, (C) metal clamping system, and (D) CMOS camera. In (f) foam tape attached to underside of both grips on all four surfaces and (g) enlarged image of clamps showing grip region.

The applied stretch (λ) was calculated as the ratio of the current to unloaded grip to grip distance. The non-zero component of the Cauchy stress (σ) was calculated as the external load (F) measured by the load cell, divided by the current cross-sectional area in the test region, (A). The current cross-sectional area A was defined as the unloaded cross-sectional area (A_0) in the middle of the sample (unloaded width times thickness) divided by the stretch, where in doing so, the deformation was approximated as isochoric (material idealized as incompressible).

2.2.5 Classification of Failure Location and Failure Mode

Based on the videos obtained during mechanical testing, the failure locations were classified into three groups, "Clamp", "Middle" and "Transition". In particular, specimens that failed within 0.5 mm of the edge of the grips were defined as "Clamp" failure. Those that failed in the middle 50% of the sample were defined as "Middle" failure. Failure in between these two regions was considered a "Transition" region failure. Locations were defined in the deformed configuration.

Three failure modes i) cracking, ii) necking and iii) delamination were defined for each specimen based on the following definitions:

Cracking mode: Visible crack is seen to initiate and then propagate across the width of the sample as a through-thickness crack, ending in sample failure.

Delamination mode: A visible tear starts in a single layer and then propagates across the width of the sample. Often a retraction of this layer follows. As the applied stretch increases, the crack ultimately proceeds in both layers across the sample width, until complete sample failure is seen.

Necking mode: The width of the middle region of the sample narrows without cracking until complete failure of the sample is seen.

2.2.6 Classification of Failure Process as Abrupt or Gradual

The failure process was categorized as abrupt or gradual based on the nature of the mechanical loading curves. In particular, an R factor [53] was defined as Equation 2-1 and it was used to distinguish between abrupt and gradual failure, Figure 2.

$$R = \frac{Area\ under\ the\ Cauchy\ stress\ stretch\ curve\ after\ ultimate\ stress}{Total\ area\ under\ the\ Cauchy\ stress\ stretch\ curve} \qquad \textbf{2-1}$$

Abrupt failure: Once the ultimate Cauchy stress (σ_U) is reached, stress rapidly drops down in a 'brittle' manner. Specifically, loading curves with an R factor less than 1/3 (0.33) are categorized as having abrupt failure.

Gradual failure: The stress diminishes over a relatively long stretch. This was defined quantitatively by an R factor greater than 1/3.

Gradual failure was further classified in three different groups, Figure 2,

G-1. The stress displays a single maximum σ_U and drops down gradually to zero after this single peak.

G-2. There are multiple peaks before complete sample failure.

G-3. The stress drops down abruptly after σ_U followed by a plateau before stress falls to zero gradually.

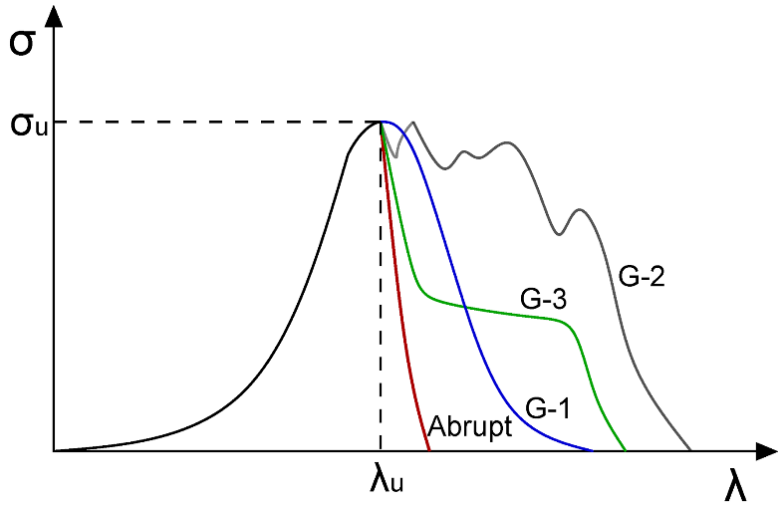

Figure 2 Illustration of abrupt and gradual failure in mechanical loading curves. Shown are idealized loading curves to illustrate nature of abrupt failure and the three types of gradual failure (G-1, G-2, G-3).

2.2.7 Statistical Analysis

Statistical analysis was conducted with SAS Analytics (SAS Institute Inc.). The association between testing methods and the failure location of the sample was evaluated using Fisher's exact test. This test was also used to compare the failure process in three failure modes. Analysis of variance (ANOVA) was utilized to test whether the ultimate stress and stretch between test categories were statistically different. Differences were considered significant if the p value was less than 0.05.

2.3 Results

The mechanical curves along with sample images for representative cases from each of the three test categories (DB-FT, Rect-FT, Rect-SP) are shown in Figure 3 (sheep carotid) and Figure 4 (human basilar). Images were chosen to show the specimen at stretches of interest including low stretch, ultimate stretch and post ultimate stress prior to complete failure. The associated data for all cases are provided in Table 2 (sheep carotid) and Table 3 (human basilar).

Good control of the desired specimen dimensions was achieved during sample preparation yielding unloaded rectangular specimen dimensions of 6.0 ± 0.2mm × 2.4 ± 0.3 mm and width of the mid-region of the dogbone samples of 1.2 ± 0.15 mm, Figure 1(c,d). The average thickness of human basilar artery samples was 322 ± 28 um and the average thickness of the sheep carotid arteries samples was 548 ± 19 um.

There were no "Transition" failure cases as all samples fell into either the "Middle" or "Clamp" failure categories. While "Middle" failure was defined as the middle 50% of the sample, in fact, for the sheep carotid arteries, all "Middle" failure cases failed within 10% of the center of the sample. For the human basilar arteries, the "Middle" failure cases always occurred within 45% of the center.

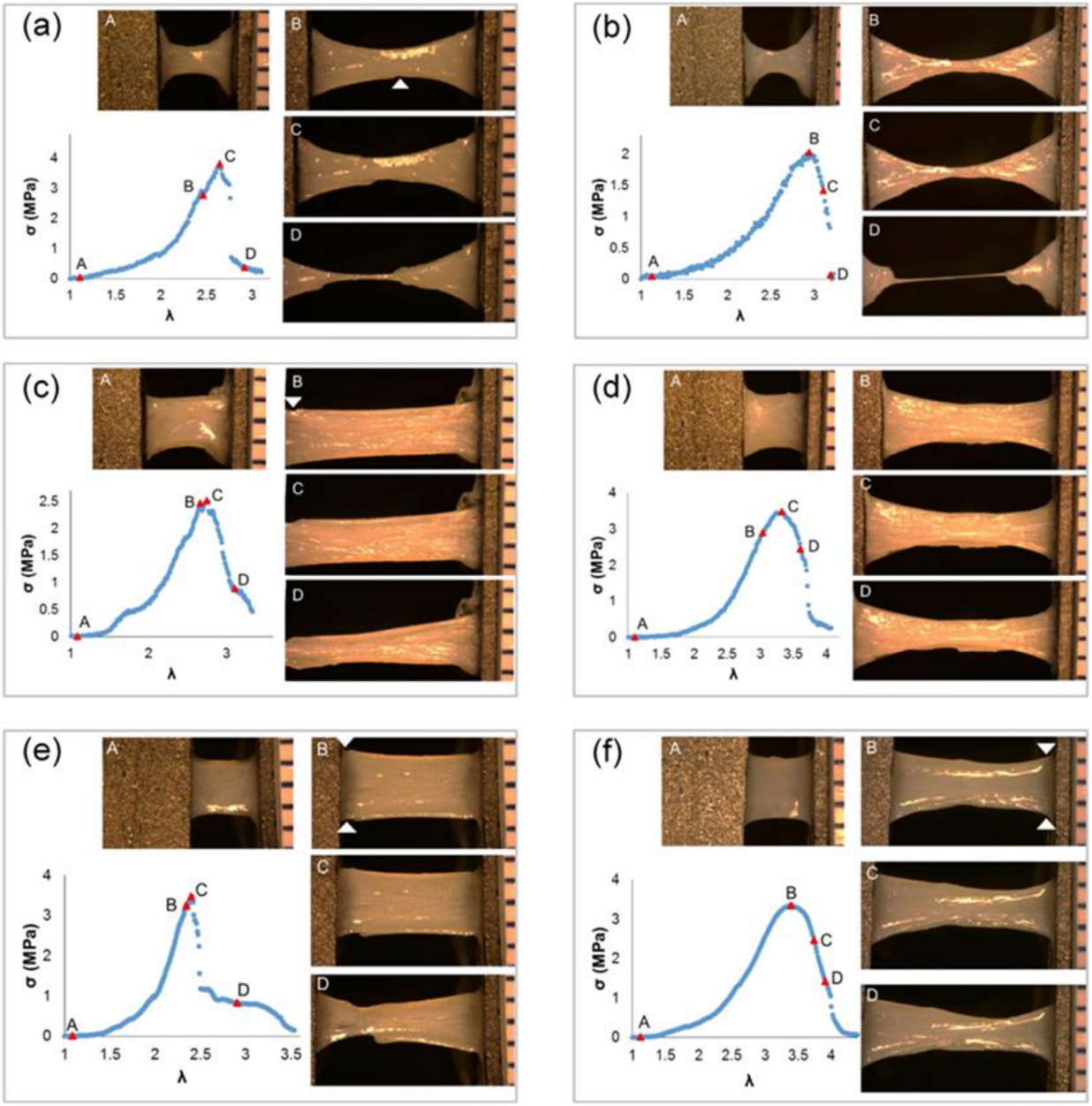

Figure 3 Failure process in sheep carotid artery specimens. Four levels of deformation during loading to failure are shown: Row 1: DB-FT for (a) #S2 and (b) #S7; Row 2: Rect-FT for samples (c) #S13 and (d) #S15; as well as Row 3: Rect-SP for (e) #S19 and (f) #S21. Location of crack that led to catastrophic failure is marked by a white arrowhead, where identifiable. Adventitial side of specimen is facing camera.

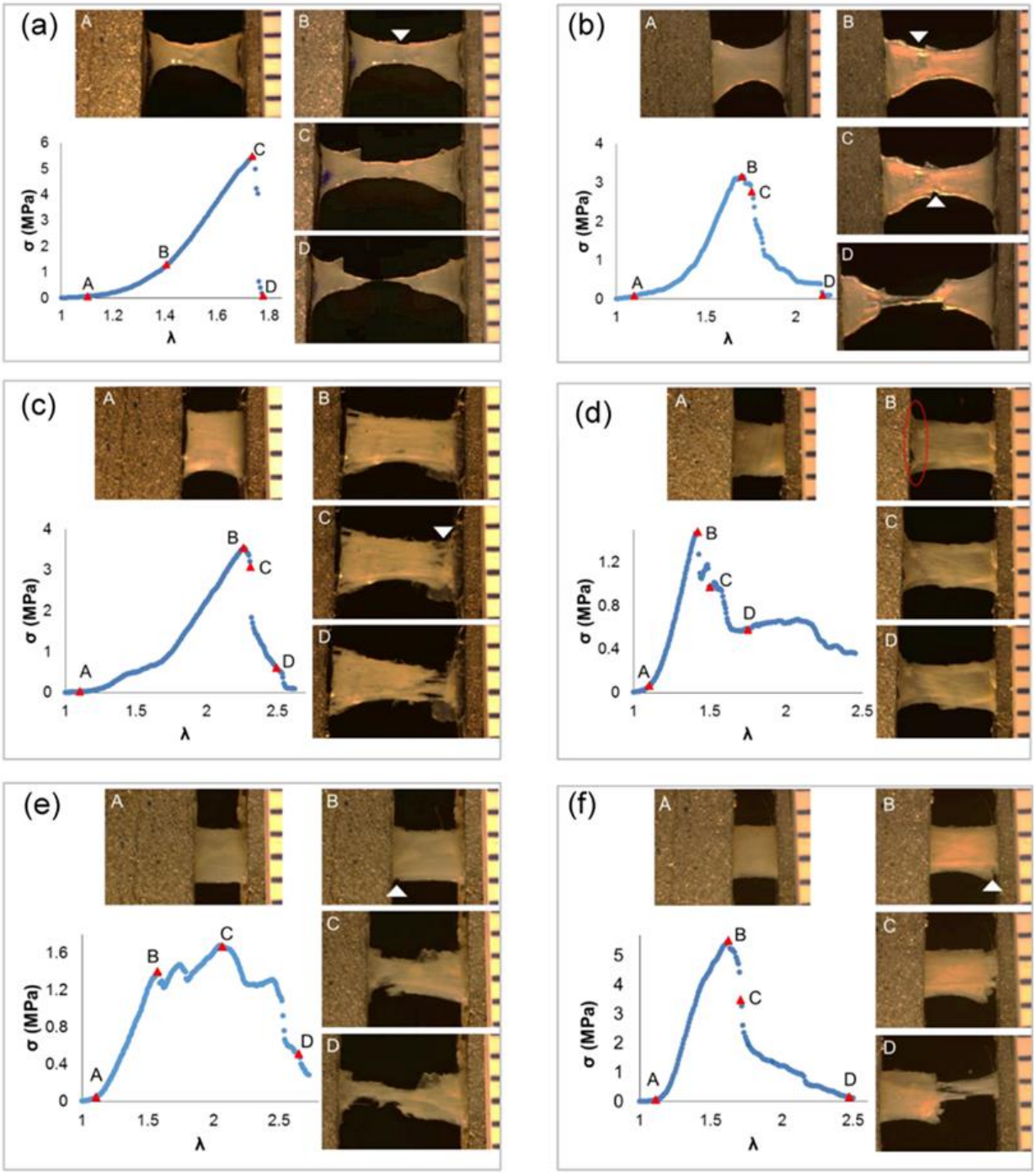

Figure 4 Failure process in human basilar artery specimens. Four levels of deformation during loading to failure are shown. Row 1: DB-FT for (a) #H2 and (b) #5; Row 2: Rect-FT for (c) #H8 and (d) #H11; as well as Row 3: Rect-SP for (e) #H14 and (f) #H17. Location of tear that led to catastrophic failure is marked by a white arrowhead or circled in red, where identifiable. Adventitial side of sample is facing camera.

Table 2 Results of failure testing for sheep carotid artery specimens. The notation N/A is used for cases where there was no visible initial crack before total failure.

		Failure initiation location		Ultimate failure location		Ultimate stress (MPa)	Ultimate stretch	Stress drop caused by	Failure Mode	Failure Process	
	#	Clamp	Middle	Clamp	Middle					Gradual	Abrupt
DB-FT	S1		√		√	N/A	N/A	total breakage	Cracking		A
	S2		√		√	3.83	2.65	total breakage	Cracking		A
	S3		√		√	4.81	3.2	media tear partially	Delamination	G-1	
	S4		√		√	4.35	2.85	total breakage	Cracking		A
	S5		√		√	3.85	2.62	total breakage	Cracking		A
	S6	N/A			√	1.15	2	total breakage	Necking		A
	S7	N/A			√	2.03	2.94	total breakage	Necking		A
	S8	N/A			√	1.89	2.66	total breakage	Necking		A
	S9	N/A			√	2.34	2.53	total breakage	Necking		A
	S10		√		√	3.11	2.51	media tear initiated	Cracking		A
Rect-FT	S11	√		√		2.63	2.49	media tear initiated	Delamination	G-2	
	S12	√		√		2.49	2.48	outside FOV	N/A	G-1	
	S13	√		√		2.51	2.75	media tear partially	Delamination	G-1	
	S14	√		√		3.91	3.08	media tear partially	Delamination	G-1	
	S15		√		√	3.49	3.33	necking	Necking	G-1	
	S16		√		√	2.9	2.92	partial tear	Necking	G-1	
Rect-SP	S17	√		√		4.5	2.43	media tear partially	Delamination	G-1	
	S18	√		√		2.55	2.59	media tear partially	Delamination	G-1	
	S19	√		√		3.48	2.41	media tear partially	Delamination	G-3	
	S20	√		√		2.96	2.44	media tear initiated	Delamination	G-3	
	S21	√		√		3.35	3.4	partial tear	Necking	G-1	
	S22	√		√		3.07	2.45	media tear initiated	Delamination	G-1	

Table 3 Results of failure testing for human basilar artery specimens

		Failure initiation location		Ultimate failure location		Ultimate stress (MPa)	Ultimate stretch	Stress drop caused by	Failure Mode	Failure Process	
	#	Clamp	Middle	Clamp	Middle					Gradual	Abrupt
DB-FT	H1		√		√	4.72	1.7	total breakage	Cracking		A
	H2		√		√	5.48	1.74	total breakage	Cracking		A
	H3		√		√	6.21	2.09	total breakage	Cracking	G-1	
	H4	√		√		6.26	1.98	total breakage	Cracking		A
	H5		√		√	3.16	1.7	total breakage	Cracking	G-1	
	H6		√		√	3.79	1.67	total breakage	Cracking		A
	H7		√		√	3.43	1.77	total breakage	Cracking		A
Rect-FT	H8	√		√		3.54	2.27	partial breakage	Cracking		A
	H9	√		√		7.77	2.86	media tear	Cracking		A
	H10	√		√		3.88	1.77	partial tear	Necking	G-3	
	H11	√		√		1.48	1.42	media tear	Delamination	G-3	
	H12	√		√		1.54	2.13	partial tear	Necking	G-2	
Rect-SP	H13	√		√		2.62	2.1	media breakage	Delamination	G-1	
	H14	√		√		1.68	2.04	media breakage	Delamination	G-2	
	H15	√		√		2.85	1.9	media breakage	Delamination	G-3	
	H16	√	√		√	5.72	1.89	total breakage	Cracking		A
	H17	√		√		5.51	1.63	partial breakage	Cracking	G-1	

2.3.1 Dogbone Specimen Failure Testing

Tests on the dogbone specimens showed great consistency. Sixteen out of 17 dogbone samples failed in the mid-region of the sample, supporting the hypothesis underlying this work. Loading beyond the maximum Cauchy stress was associated with immediate tissue failure (total breakage) in 15 out of 17 cases.

The DB-FT sheep carotid artery specimens showed substantial uniformity in failure location and process. All dogbone sheep samples failed in the middle (n=10) and all but one of the specimens failed abruptly (n=9). The cause of failure was due to cracking (n=5, e.g. Figure 3(a)) or by necking (n=4, e.g. Figure 3(f)).

Six of the 7 human basilar arteries failed in the middle. All 7 of these specimens failed due to cracking, e.g. Figure 4(a,b). Two of the 7 samples displayed gradual failure, though with relatively low R factor values of 0.36 and 0.42, e.g. Figure 4(b).

2.3.2 Rectangular Specimen Failure Testing

In contrast to the dogbone samples, most (19/22) of the rectangle strips failed in the clamp region, suggesting the artifacts at the grip often dominated the failure process in rectangular samples, even in the presence of a soft insert. More precisely, the failure location was not significantly affected by insert material (Rect-SP versus Rect-FT, p=1 for human and p=0.4545 for sheep), Figure 5. In all 19 cases, the failure process initiated at the clamp.

In rectangular shaped samples all three failure modes were seen: cracking (Figure 4(c,f)), delamination (Figure 3(c,e), Figure 4(d,e)) and necking (Figure 3(d,f)). In contrast to the dogbone

specimens, most rectangular samples displayed gradual failure (19/22), e.g. Figure 3(c-f), Figure 4(d-f).

For the sheep carotid artery, 10 out of 12 of the rectangular samples failed at the clamp. When the sandpaper insert was used, the most common failure mode was delamination (5/6 cases), while with the soft foam tape insert, failure was mixed between delamination and necking. Delamination always initiated with a tear on the lumenal side (intima/media), regardless of the insert material. The drop from ultimate stress was never associated with complete failure, rather the drop most frequently occurred when only minor tears to the medial layer were visible, Figure 3(c,e).

For the human basilar arteries, only one rectangular sample failed in the middle (1/11).

2.3.3 Comparison of Dogbone and Rectangular Specimens

Middle failure was achieved in 94% of the dogbone specimens and only 14% of the rectangular samples. Furthermore, the failure location differed significantly between DB-FT and Rect-FT specimens, (human basilar $p=0.0152$; sheep carotid artery $p=0.0082$), Figure 5.

The choice of specimen shape and insert material did not significantly impact the ultimate stress or ultimate stretch in either human or sheep samples, despite the significant differences in failure location, Figure 6, with average ultimate stress of 4.1 MPa ± 1.84 MPa for human basilar arteries across all protocols. These are consistent with values of ultimate stress reported in the literature for cerebral arteries with reported average Cauchy stress from 3.0 MPa to 4.75 MPa [11,54]. The ultimate stress across protocols for the sheep carotid arteries was 3.01 MPa ± 0.92 MPa. No prior results were found in the literature for failure of sheep carotid arteries.

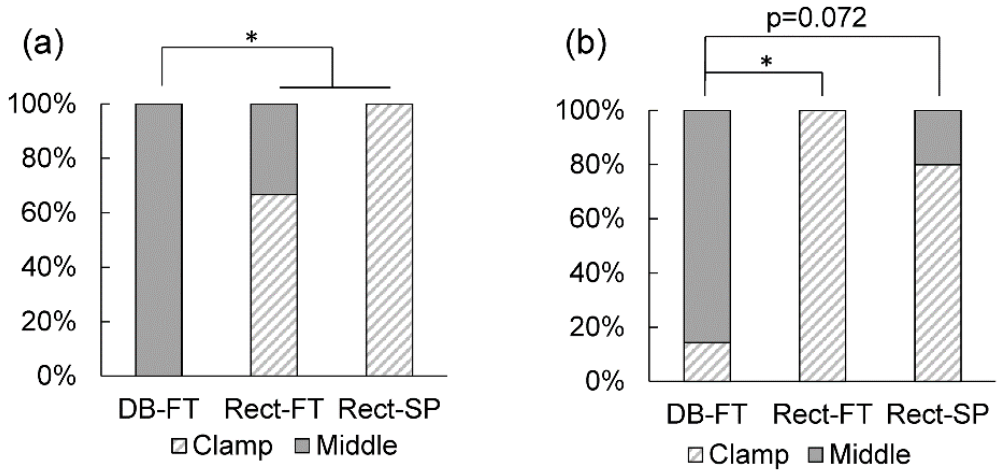

Figure 5 Middle failure consistently achieved in dogbone specimens with foam tape. Distribution of clamp versus middle failure for three test groups for (a) sheep carotid artery and (b) human basilar artery. No samples failed in the Transition region.

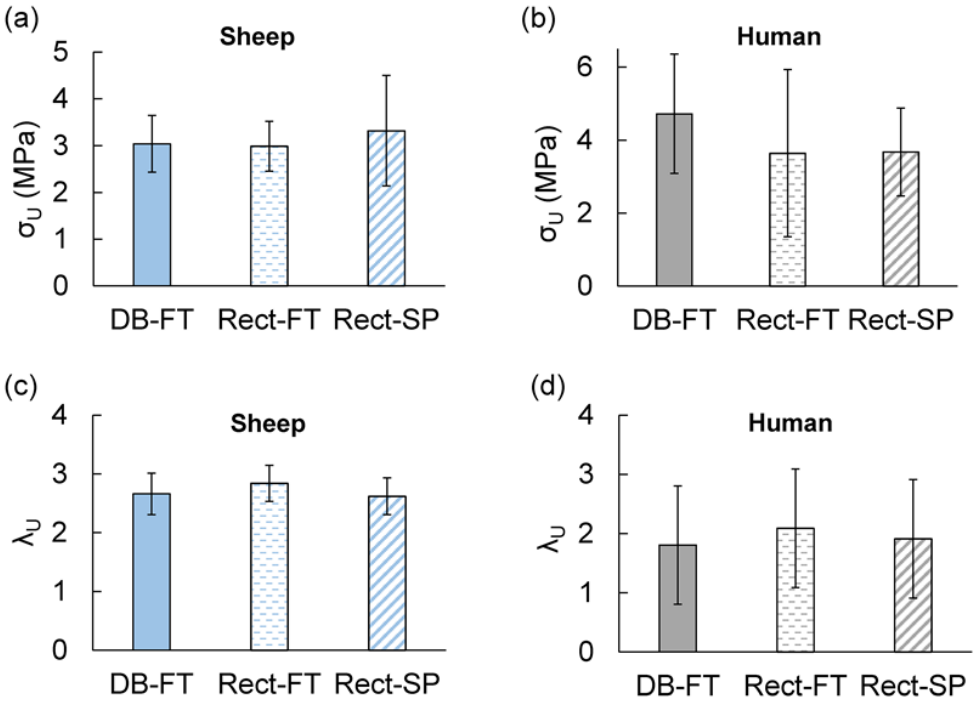

Figure 6 No significant difference in ultimate stress or strain for different testing methods. Row 1: Ultimate stress in (a) sheep carotid and (b) human basilar arteries: Row 2: Ultimate strain in (c) sheep carotid and (d) human basilar arteries. The bars show average ultimate failure stress and stretch with standard deviation**.**

2.3.4 Relationship between Failure Mode and Mechanical Response

The failure process (abrupt versus gradual) differed with failure mode ($p<0.0001$), Figure 7(a). In cracking mode, the stress decreased abruptly after the ultimate stress was reached for most cases, Table 2 and 3. In contrast, materials failing in a delamination mode always showed gradual failure. Those showing necking displayed a mix of abrupt and gradual failure process.

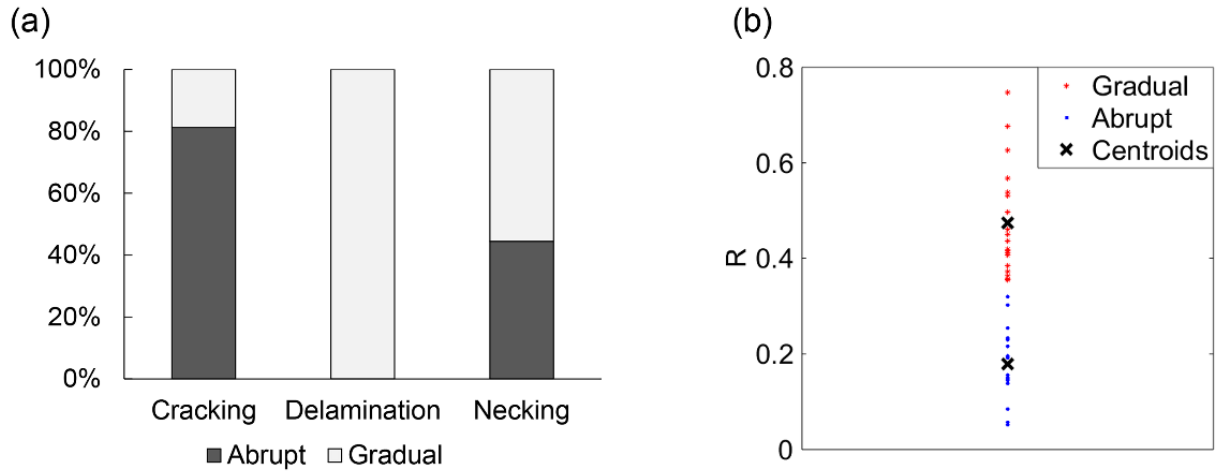

Figure 7 Failure process differs significantly between failure modes. (a) Distribution of abrupt and gradual failure are significantly different for three failure modes in ensemble of 39 samples of vascular tissue ($p<0.0001$), (b) Cluster diagram showing distribution of samples into abrupt and gradual failure groups based on areas under mechanical loading curve using the R factor.

2.4 Discussion

This work has shown that failure in the central region of even small vascular samples can be achieved consistently using dogbone shaped specimens with soft grip inserts, avoiding grip associated artifacts and, in the future, will enable imaging of the changes to the collagen fibers during the failure process. In contrast, less than 14% of rectangular specimens failed in the middle region, with no significant improvement from soft insert material. These conclusions are based on uniaxial testing in 39 specimens of only 6 mm in length from the carotid arteries of young sheep as well as from cerebral vessels of older adults (mean age 73.6 ± 4.3 years).

Despite an increasing focus on failure for a wide range of vascular tissues [3,26,32–35], prior to the current study very little quantitative information was available on failure location or mode for uniaxial testing of vascular tissue, Table 1. Furthermore, there were no established best practices for selecting sample shape or gripping method. An underlying assumption in much of the literature is that both rectangular and dogbone shaped samples are appropriate. While frequently unreported, clamp failure rates as high as 37% have been reported in rectangular specimens, even when rubber coated grips were used [19]. In a very relevant study on small rectangular specimens (7.2 mm × 2.81 mm) of coronary arteries using sandpaper inserts, it was found that only "… a small number of samples fractured within the gauge section" and the authors conjectured that, "Dumbbell-shaped samples might increase the success rate of fracture tests" [15]. Consistent with this work, we found that few rectangular samples with sandpaper inserts failed in the mid-region (only 1/11). We found even less information on failure location for dogbone specimens, Table 1. Shah [28] performed failure testing on the medial layer of healthy ascending thoracic aorta and reported a 28% failure rate at the grips, details were not found on use of inserts.

A recent study on meniscus tissue provides an extensive analysis of the impact of sample shape on uniaxial failure results, using cloth sandpaper inserts for all samples [36]. While the structure of the meniscus is substantially different than arterial tissue and the specimens are more than four times larger than in the current study, it is worth commenting on these results since studies of vascular tissue comparing the role of specimen shape were not found. Failure in the mid-region was rare for their circumferentially aligned samples, found in only 1 out of 11 of the dogbone and none of the 23 rectangular specimens. The radial samples showed higher, but still low, mid-region failure. Using an elegant assessment of the strain fields, the authors demonstrated artifacts from the grips extend to the mid-sample region for both dogbone and rectangular samples when sandpaper inserts were used. This low mid-region failure is consistent with the current study, where a combination of dogbone shape and soft inserts were needed to obtain regular failure away from the clamps. Our own preliminary studies on dogbone samples with sandpaper inserts gave unacceptable levels of grip failure (more than 75%), prompting us to shift to soft insert materials and leading to the current investigation.

As previously noted, in a desire to avoid possible artifacts associated with clamping, some researchers explicitly discard samples that fail at the clamps. Such artifacts include stress concentration and shearing damage associated with deformations adjacent to the clamps. Hence, the methodology developed here for consistent mid-region failure in small samples will enable meaningful data to be obtained from a larger percentage of specimens. This is an important consideration for biological samples which are often difficult to obtain and heterogeneous across specimens.

This study found important differences in the failure process at the clamp region compared with mid-region failure, which we conjecture arise due to the stress concentrations and shearing

near the clamp/tissue interface. We anticipate the stress concentration will vary across the clamp/tissue interface in contrast to the more uniform stress distribution at the mid-region of the tissue sample. We found that in the human basilar arteries from aged adults, the mid-region failure was always due to cracking, regardless of the sample shape or grip insert (7/7 cases), Table 3. In contrast, all three failure modes were seen for clamp failure. For sheep carotid arteries, mid-region failure was associated with necking as well as cracking, almost equally split between these groups, while clamp failure was nearly always associated with delamination, Table 2. These substantial differences suggest artifacts associated with clamping may introduce an alternate failure process - an important consideration when designing studies to understand causes of tissue failure or strength in vascular samples [55].

We did not find any published guidelines for small dogbone samples of soft biological tissues. In fact, this lack of guidelines was a motivation for the current work, where we focused on introducing and using a methodology for testing the minimum sample size we could test to failure in a reproducible manner. After iterative preliminary testing, we found this to be about 6 mm in length. This 6 mm length then served as a constraint for the length of the narrow test region of the dogbone sample given the need to firmly grip the ends of the sample for failure testing. The choice of the width of the dogbone sample was made after iterative mechanical testing with the objective to create reproducible geometries and consistent results. The methodology developed here for consistent uniaxial failure testing of dogbone samples of only 6 mm in length and 1.2 mm width at the mid-region, opens the possibility for efficiently testing multiple specimens of different orientations obtained from a single vascular sample. Given the focus on small samples, we did not investigate whether larger samples would display similar results with respect to for failure location and process.

Another method used to analyze the failure process in arteries is inflation testing (burst tests) of either intact vessel segments or circular clamped membranes, enabling biaxial loading of the tissue (e.g. [56–61]). The tubular inflation tests generate loading that is similar to the in vivo kinematics and inherently reproduces the in vivo residual stress, neither of which are possible in uniaxial testing. For example, Bellini et al. considered inflation failure in mice with impaired collagen fiber formation, finding these mice largely displayed a delamination failure compared with failure due to a transmural crack in control mice [61]. Burst tests on clamped circular membranes also involve biaxial loading, though with one degree less control than for the tubular geometry. Burst tests on clamped circular segments of human aortic aneurysms have yielded important results on failure direction [60] and localized wall thinning prior to failure [62]. An advantage for both the uniaxial testing protocol used here and clamped membrane testing is that failure occurs in a prescribed location, so the failure process is readily imaged. Uniaxial testing enables smaller samples to be used than currently possible in clamped membrane testing and with the potential to concurrently image both sides of the tissue to assess subfailure changes (e.g. [63]) and under microscopy.

In this work, when the delamination mode was seen, it always initiated with subfailure on the lumenal side of the artery that propagated across the width of the tissue without penetrating through the wall (e.g. only in the intima/medial layers of the wall). Delamination was evidenced by the retraction of these layers and separation from the deeper layers. These aspects of delamination failure are consistent with previous reports of delamination in uniaxial, tubular inflation and clamped membrane testing of arterial tissue with initial failure on the lumenal side [38,60,61,63,64]. In Bellini et al. [61], histological analysis was used to confirm delamination

occurred between the media and adventitia for an inflation study of the descending thoracic aorta of mice (lacking thrombospondin-2).

An interesting finding in the current work was the drop from ultimate stress most frequently occurred when only minor tears to the medial layer were visible. Hence, the area used to determine peak stress and strain could be consistently estimated. These results suggest the post peak failure process considered here is of importance in understanding tissue failure in clinical applications and is worthy of further investigation.

Limitations and Future Directions

There are several limitations to the current study that suggest directions for future work. While the present study included tissues from two different species, two age groups and a large range in ultimate stress (1.15 MPa to 6.26 MPa, for DB-FT), this work was not a comprehensive study of all soft tissue types. For example, we did not consider tissues heavily laden with atherosclerotic plaque, nor did we consider stiffer and stronger tissues such as ligaments and tendons. While we avoided samples with gross variations in thickness it is possible that modest variations in wall thickness would not be captured using digital calipers. For tissue with more heterogeneous thickness, methods such as micro-CT could be used to characterize these variations over the sample in the unloaded state (e.g. [65]). Residual stress is not considered in this study as it cannot be imposed in uniaxial testing. The opened segment of tissue is presumed to be stress free. Additional artifacts could arise from tissue storage including time between tissue harvest and testing as well as from freezing related artifacts. To avoid bias in the study from the artifacts, samples within each species were handled and stored in a consistent manner.

We also note that the definition of abrupt and gradual is not unique. Here, we chose a method that is user independent based on the relative areas under the loading curves pre and post ultimate stress. A cluster analysis, Figure 7(b), supported the choice of an R factor cut off value of 1/3, though there are two cases that could be viewed as close to this demarcation value.

Another limitation of this work is that stretch levels were estimated using grip to grip distance rather than using methods such as digital image correlation (DIC). Our preliminary studies for this work demonstrated that DIC could not be used to estimate strain during the failure process in cases where the specimen failed in delamination mode or in other cases where the strain across the thickness of the sample was not heterogeneous and/or the deformation was far from affine. For consistency, we therefore chose to use grip to grip distance. Errors associated with this approach would not change the central conclusions in this work including failure location.

While DIC has inherent challenges and complexities, the use of DIC is of particular value in failure analysis to understand the local nature of the failure process, (e.g. [60]). Even so, challenges arise when the failure process cannot be well tracked by the markers used in DIC, such as during retraction due to delamination. The present work does suggest some opportunities for DIC going forward. The delamination mode was nearly always associated with clamp failure. Therefore, it is expected that measurement problems associated with DIC during delamination failure could be avoided using the DB-FT protocol. For example, a system could be used to obtain DIC data from both the adventitial and medial sides, providing a more localized and layer dependent assessment of the strain field past failure initiation. Such an approach would not be possible with inflation studies of failure.

While it was not the objective of this study to characterize the failure properties of sheep carotid and human basilar arteries, we did find it striking that the ultimate stress and strains were

not significantly different across the test groups in this study (DB-FT, Rect-FT, and Rect-SP), Figure 6. Similarly, there were no significant differences in these values between middle and clamp failure groups, which is consistent with earlier reports on tendon and ligament [66]. While this could suggest the clamp artifacts may have only small to moderate influence on the failure stress, it could also suggest more samples are needed to reach statistical significance due to the large degree of heterogeneity in arterial tissues. For example, even in the carotid arteries of young sheep where all DB-FT specimens failed in the middle region, the ultimate stress ranged from 1.15 MPa to 4.81 MPa with an average value of 3.0 MPa ± 1.3 MPa. This large range in values is consistent with recent reports on ultimate stress in sheep cerebral arteries where values of ultimate stress (though under biaxial loading) in juvenile sheep (3-7 months) ranged from 1.5 to 6.0 MPa [67]. Hence, a comprehensive study of possible artifacts in strength measurements caused by clamp failure might require a larger sample size for arterial tissues. Alternatively, in silico experiments could be run to assess how failure stress and stretch are altered under the different test conditions for fixed material properties [49], ideally including multi-scale modeling of the extracellular matrix [47]. Given the large range in material properties in even young animals, it is perhaps even more striking that mid-region failure was consistently attained in these dogbone specimens using the DB-FT protocol.

The findings in this study introduce new questions related to the failure process in arterial tissue that can be addressed in the future using combined optical/mechanical testing- made possible with consistent mid-region failure as well as complimentary histology work. For example, what structural differences within the young sheep population lead to the different failure modes (cracking and necking). Are there age related changes in the extracellular matrix that promote brittle type failure (abrupt, cracking) in the older human arteries? Or, is this failure also typical of

basilar arteries in younger adults. More generally, with consistent mid-region failure, new questions on failure in arterial tissue can be answered using modalities such as multiphoton or confocal microscopy, simultaneous with mechanical testing so that, for example, the delamination process can be observed in situ. Such studies have the potential to provide new insights and valuable quantitative information about changes to collagen and elastin structure during the failure process [55,68].

2.5 Acknowledgment

I wish to thank Dr. Robertson for her supervision in this chapter, and Dr. Maiti and Ronald Fortunato for their contribution to the data analysis. I am grateful to the human cerebral arteries provided by Dr. Kofler, and sheep carotid arteries provided by Dr. Wang and Chelsea Stowell.

3.0 Adaptive Remodeling in the Elastase-Induced Rabbit Aneurysms

The work in this chapter was reprinted by permission from Springer Nature Customer ServiceCentre GmbH: Springer Nature Experimental Mechanics

Sang, C., Kallmes, D.F., Kadirvel, R., Durka, M.J., Ding, Y., Dai D., Watkins, S., & Robertson, A.M. Adaptive remodeling in the elastase-induced rabbit aneurysms. *Experimental Mechanics* (2020) [69]

3.1 Introduction

An intracranial aneurysm (IA) is an enlargement in the wall of a cerebral artery that is generally saccular in shape, though the geometry can be quite irregular [9]. Rupture of IAs is estimated to occur at a rate of 1.3% per year [1] and can cause subarachnoid hemorrhage with an associated mortality rate of 40-65% [2]. Current treatments for IAs are largely aimed at isolating the aneurysm wall from the circulation through treatments that include placement of mechanical clips across the aneurysm neck, insertion of coils into the aneurysm sac and placement of flow diverters across the aneurysm neck. Treatment options of IAs, including surgical clipping and endovascular interventions, are themselves associated with substantial risk of morbidity (6.7% and 4.7%, respectively) and mortality (1.7% and 1.8%, respectively) [70,71]. As result, numerous research groups are endeavoring to improve methods for risk assessment [9,72–74], including, the possibility of using preferential uptake of gadolinium contrast agent [75–78] and by developing endovascular devices for diagnostic imaging the IA lumen [79,80].

Current risk assessment is largely driven by aneurysm size [4], though this approach has limitations as most aneurysms that rupture are small (70% of ruptured aneurysms have a diameter below 7 mm) [1]. A confounding factor in identifying other risk factors is that most approaches to risk assessment necessarily use the characteristics of ruptured aneurysms as representative of the features of high risk unruptured aneurysms. This approach is largely unavoidable as it is rare to have imaging data to track aneurysms over time and determine features of unruptured aneurysms that go on to rupture. Recently, the strength of aneurysm walls has been directly measured and used instead of rupture status to identify aneurysms that are vulnerable to rupture [11]. Using this approach, wall geometry and hemodynamics associated with wall vulnerability have been evaluated [11,20,21]. Still, there remains a pressing need to understand the temporal nature of changes to the wall during disease progression and, in particular, the diverse physical causes of diminished wall strength. Such information will be vital for developing effective metrics for risk assessment and novel pharmacological treatments to strengthen the aneurysm wall.

The passive mechanical response of healthy arterial tissues is largely determined by the organization and properties of the elastin and collagen fibers within the wall [81]. In contrast to cerebral arteries, elastin is nearly always absent in IA walls and in fact, the loss of elastin is considered an early event in aneurysm formation [82,83]. Therefore, the stiffness, strength, and organization of the collagen fibers are critical in defining the mechanical properties of IA walls. Clinical studies of changes in IA geometry over time have identified local changes in the form of blebs as well as more global enlargements [13,84]. The collagen fabric must adapt to the altered geometry in order to maintain a sustainable level of intramural loads and avoid rupture under extremes in physiological loading [11,85]. Indeed, both temporal increases size and irregularity in shape (e.g. blebs) are associated with increased risk of rupture [86], supporting the importance of

effective remodeling in response to the changing IA geometry. Therefore, understanding the capacity of the aneurysm wall to maintain and evolve this collagen fabric is essential for improving risk assessment and developing new therapies.

Although collagen remodeling is a key factor in determining IA rupture risk, it has received little attention. Few studies have directly evaluated the collagen fibers or their architecture [11]. As a result, many fundamental questions important to aneurysm patients remain regarding the capacity of an IA for effective remodeling and the factors that contribute or detract from this capacity. While intracranial aneurysm tissue can be harvested following treatment by surgical clipping, these samples can only represent one time point in the progression of the disease.

Animal models for intracranial aneurysms offer larger numbers of samples and provide a means for studying multiple time points in disease progression, though their clinical relevance must always be evaluated. This type of temporal data is crucially needed to answer fundamental questions about the remodeling process. Growth and remodeling (G&R) theories have been developed to study the evolution of aneurysms [87–89] and in particular, constrained mixture theories have been developed to model the production, degradation and turnover rates of different structural constituents such as collagen [87,88]. However, it is only through a tight and iterative coupling of theory driving experimental design and experimental data driving theoretical formulations that meaningful progress can be made. While the theoretical frameworks are crucial for interpreting the complex coupling between mechanics and biology, their value rests on the inclusion of the key biomechanical mechanisms for the application at hand, which necessarily can only be determined by experiments. For example, in the case of the evolving aneurysm wall, it is crucial to understand how and where in the wall the remodeling occurs. Does remodeling occur via a reorganization of the existing collagen matrix, or is it the result of the deposition of a new

layer? Is there a single mechanism of adaptation? Or, are there multiple stages of the remodeling process, such as an early response to an acute event followed by a second phase of reorganization? A two phase response of this kind, has been reported in tissue engineered blood vessels [90,91] and is in fact, known in other context [92]. Until these fundamental questions about adaptive remodeling in cerebral aneurysms are answered, the clinical impact of G&R computational studies will be limited.

The objective of the present study then, is to use an established elastase induced aneurysm model in rabbits, to investigate these fundamental questions. In prior work, the rabbit model has been shown to have similar flow types and histologic wall types to human aneurysms [93,94]. In the present work, the changing collagen organization and mechanical properties in the aneurysm model are assessed at multiple time points after aneurysm creation as the aneurysm geometry evolves. Multiphoton imaging of the collagen matrix is performed to evaluate the evolving wall architecture to determine where in the wall, and when, the growth and remodeling occurs. Mechanical testing is used to assess whether the remodeling is effective in adapting to the altered mechanical environment. This work is the first to assess collagen remodeling in an animal model of saccular aneurysm and lays the foundation for future work to develop novel therapies to enhance the structural integrity of the aneurysm wall.

3.2 Methods

3.2.1 Creation of Rabbit Aneurysms and Acquisition of Tissue

Saccular aneurysms were created in 22 New Zealand white rabbits using vessel ligation and elastase incubation as described previously [95]. All procedures were approved by the Institutional Animal Care and Use Committee (IACUC) at the Mayo Clinic and followed the NIH Guidelines for the Care and Use of Laboratory Animals. Briefly, a sheath was introduced retrograde into the midportion of the right common carotid artery (RCCA). A balloon catheter was then advanced through the sheath to the origin of the RCCA to occlude the vessel, after which elastase was infused endoluminally above the balloon. After 20 minutes of incubation, the balloon was removed and the artery was ligated distally. Aneurysms developed over time from the stump of the RCCA. Aneurysms were harvested at 2 weeks (n=5), 4 weeks (n=5), 8 weeks (n=6) and 12 weeks (n=6) after creation and control vessels (left common carotid arteries) were harvested at that time. Digital subtraction angiography (DSA) and three-dimensional rotation angiography (3DRA) were performed just prior to sacrifice and used for the computational solid mechanics study, Figure 8(a). After harvest, the aneurysm sacs were bisected longitudinally, Figure 8(b). The ventral half was transported overnight on ice to the University of Pittsburgh in 1% phosphate-buffered saline (PBS) solution for assessment of collagen structure and mechanical testing, as described below, Figure 8(d, e).

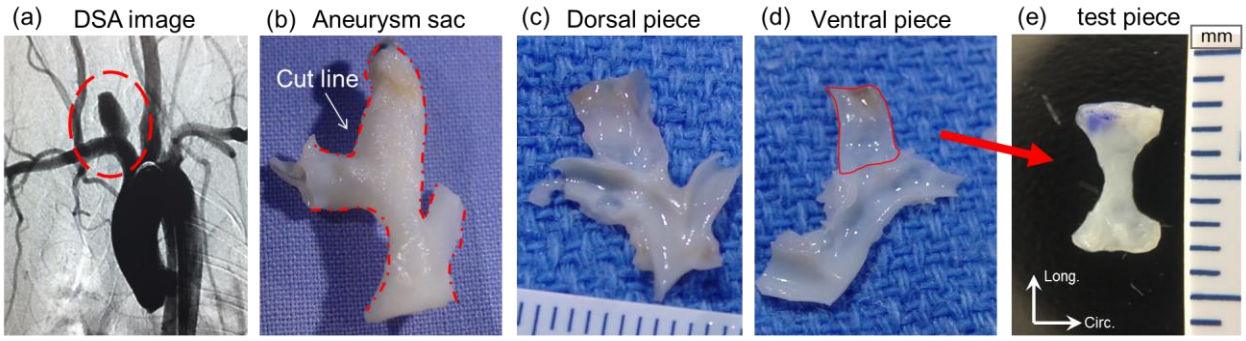

Figure 8 Tissue Harvest and Sample Preparation. (a) DSA image of aneurysm before sacrifice, aneurysm circled. (b) Aneurysm sac was bisected longitudinally, cut line shown in red, into dorsal and ventral pieces, (c) and (d) with aneurysm region in ventral pieces shown in red. (e) Dogbone shaped sample cut in longitudinal direction from ventral piece.

3.2.2 Overview of Tissue Assessment

To leverage as much information as possible at each time point, samples were assessed using multiple modalities. We provide an overview of the tissue analysis here and details of each modality are given below. After transport to the University of Pittsburgh, as described above, each intact specimen was imaged en face in the unloaded state from both the luminal and abluminal sides using multiphoton microscopy (MPM) to assess collagen fiber organization and the status of the elastic lamellae (n = 22). The samples were then trimmed into rectangular specimens with long axis aligned in the longitudinal direction of the aneurysm sac and imaged under uniaxial loading using our combined multiphoton mechanical testing system [96], that enables evaluation of the collagen reorganization under subfailure loading levels (n=16, as 6 samples were too small for testing). As described further in the following sections, this longitudinal orientation was chosen to

assess the effectiveness of tissue remodeling in response to increasing ratio of longitudinal to circumferential stress, more typical of saccular aneurysms [97]. To supplement the en face imaging, cross sections of the wall, orthogonal to the en face imaging were analyzed in the auxiliary tissue specimens that remained after the rectangular test samples were cut. In particular, these remnants were fixed and cross-sectional slices were imaged under MPM to assess collagen and elastin content in the plane orthogonal to the en face imaging plane. As a final step, IA samples (n=16) were cut into dogbone shape and tested to failure using a custom-built strain controlled uniaxial loading system [26]. In addition to aneurysm specimens, control arteries (n=6), were imaged and tested in uniaxial extension using the same protocol, (3 longitudinal and 3 circumferential orientations).

3.2.3 Imaging the Evolving Collagen Fiber Organization

3.2.3.1 Multiphoton Imaging of Collagen and Elastin Fibers

Using previously developed methods, multiphoton imaging was used to obtain stacks of planar images of collagen and elastin content across the aneurysm wall [52]. Briefly, an Olympus FV1000 MPE multiphoton microscope (Tokyo, Japan) equipped with a Coherent Chameleon Ti-sapphire laser and 1.12NA 25×MPE water immersion objective was used for the study. Using an excitation wavelength of 870 nm, stacks of 1024×1024-pixel (508×508 μm) planar images were obtained at a 2 μm vertical spacing steps ("z-stacks"). The second harmonic generation (SHG) signal from collagen was collected using a 400 nm wavelength emission filter and the autofluorescence signal from elastin due to its intrinsic two-photon excited fluorescence (2PE signal) was collected using a 525 nm wavelength emission filter. The area fraction of elastin was analyzed in planar images of the 2PE signal using ImageJ (NIH, MD, USA).

3.2.3.2 Quantification of Collagen Fiber Orientation and Waviness

Collagen fiber orientation were evaluated in the planar MPM images using a fiber tracking algorithm in the open source software ctFIRE (Laboratory for Optical and Computational Instrumentation, University of Wisconsin-Madison, WI) [98,99]. Briefly, after denoising the planar MPM images and enhancing the fiber edge features, individual collagen fibers were extracted using the fiber extraction (FIRE) algorithm, Figure 9, with parameter settings detailed in Appendix A. Default parameters were used for analysis. Fiber orientation was determined by the angle of a chord connecting the ends of the traced fiber with zero angle denoting the circumferential direction of the specimen, Figure 10(a). Heat maps of fiber angle distribution as a function of wall depth were generated based on the output of ctFIRE using custom scripts in Matlab (R2017a, MathWorks Inc., Natick, MA).

To describe the fiber angle dispersion, an anisotropy index (*AI*) was calculated based on the orientation distribution of collagen in each layer [100]. Briefly, the orientation tensor $\boldsymbol{A}$ was obtained from the orientation distribution data,

$$\boldsymbol{A} = \int_0^{\pi} \boldsymbol{r}(\theta) \otimes \boldsymbol{r}(\theta) \rho(\theta) d\theta \qquad \textbf{3-1}$$

where $\rho(\theta)$ is the probability density function (PDF) of fiber orientation, $\boldsymbol{r}$ is a unit vector defined as

$$\boldsymbol{r} = cos\theta \boldsymbol{i} + sin\theta \boldsymbol{j} \qquad \textbf{3-2}$$

The anisotropic index (*AI*) was then calculated, from its definition

$$AI = 1 - \frac{\nu_1}{\nu_2} \qquad \textbf{3-3}$$

where ν_1 and ν_2 are the eigenvalues of the orientation tensor $\boldsymbol{A}$, with $\nu_1 \leq \nu_2$. *AI* ranges from 0 to 1, taking the value zero if the fiber network has an isotropic distribution and one if the network is perfectly aligned in a single direction.

Fiber tortuosity was measured using previously published methods [52]. Briefly, fiber tortuosity was defined as the ratio of fiber arc length to linear distance between two ends and obtained directly from fiber tracings performed with Imaris (Bitplane, Switzerland). Tortuosity was measured in representative planes for each layer of all samples.

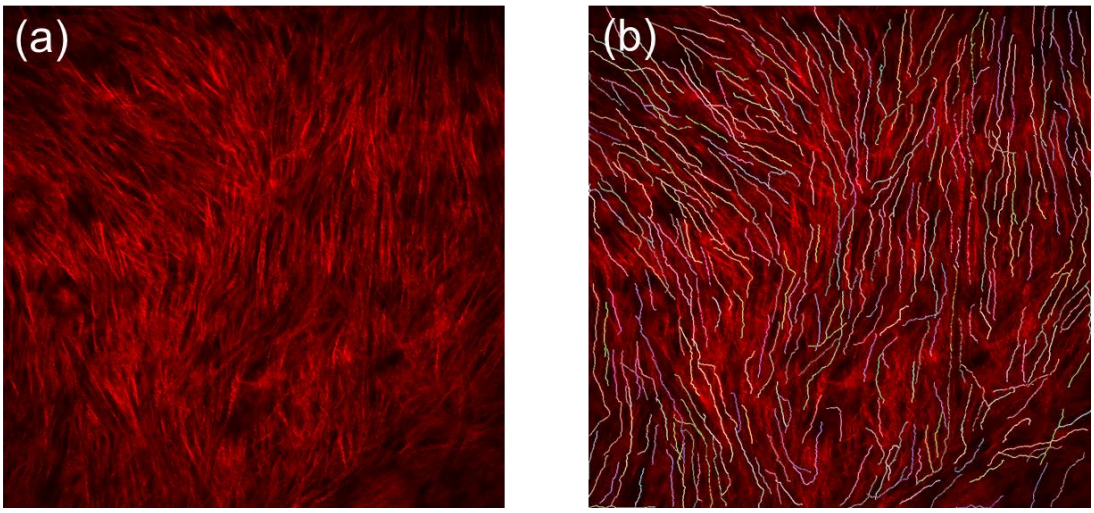

Figure 9 Example of ctFIRE traced fibers. (a) The input MPM image. (b) Output from ctFIRE with traced fibers.

3.2.3.3 Assessment of Wall Structure in Cross Sections of Fixed Tissue Samples

Auxiliary pieces of aneurysm wall, not used for mechanical testing, were fixed in 4% paraformaldehyde (PFA) at 4°C for 2 hours and frozen in OCT compound (Sakura Finetek, Torrance, CA, USA), with liquid nitrogen and cryosectioned to 8 μm thickness. These sections were then imaged under MPM, using the just described methodology, to obtain both the SHG signal (collagen fibers) and two photon emission signal (elastin).

3.2.3.4 Assessment of Collagen Fiber Reorganization under Sub-Failure Loading

A custom-built mechanical testing system that enables simultaneous multiphoton imaging and mechanical testing of soft tissues [96] was used to obtain data on collagen fiber reorganization under subfailure loading. Briefly, 6mm × 2.5mm rectangular test samples were cut from the aneurysm and control artery specimens with long axis aligned with the longitudinal axis of the vessel and aneurysm sac. The test samples were then secured in the testing system using specialized *biorakes* (CellScale Biomaterials Testing). Stacks of MPM images were obtained at increasing levels of stretch (λ) from the unloaded state in increments of 0.1, where stretch was defined as the ratio of loaded to the unloaded grip to grip distance. Due to the diversity in mechanical properties of the remodeled tissue, the maximum stretch was tissue specific and chosen in real time to avoid overextension of collagen fibers based on MPM images with simultaneous measurements of load to identify onset of high stiffness region of the loading curve. Specimens were immersed in 1% phosphate buffered saline（PBS) at room temperature during the entire testing process (approximately 2-3 hours) and preserved at -20 °C in PBS afterwards for assessment of mechanical failure properties.

3.2.4 Assessment of Mechanical Properties through Complete Failure

Prior to failure testing, the rectangular aneurysm samples (n = 16) were thawed and cut into dogbone shape with mid-region width of approximately 1.25 mm (1.25 ± 0.16 mm), Figure 8(e). Width and wall thickness were measured at three positions in the mid-region of the dogbone using digital calipers and then averaged. Following a previously published protocol for failure testing [26], foam tape was attached to the face of the metal clamps used in the uniaxial system to prevent slippage during loading while avoiding clamp failure artifacts. Specimens were submerged in a 1% PBS bath at room temperature during testing process (approximately 20 minutes) to prevent artifacts from dehydration. After three preconditioning cycles to 20% extension, the samples were loaded to failure [11,26,101]. Applied force was measured with a 5lb load cell (MDB-5, Transducer Techniques, Temecula, CA). The component of the Cauchy stress vector in the loading direction (σ) was approximated as the applied force divided by the current cross-sectional area which was approximated as the unloaded, mid-region cross-sectional area divided by stretch (assuming an isochoric deformation).

3.2.5 Estimating the Multi-Axial Nature of Intramural Stresses

The shift to a more multi-axial intramural load state in the aneurysm wall after aneurysm creation was studied by evaluating the ratio of the principal stresses in the artery and aneurysm wall. In addition to estimates using Laplace's equation for idealized geometries, the equilibrium equations for the aneurysm wall and surrounding vasculature were solved using the finite element method. As the aneurysm walls are thin relative to the radius, we took advantage of known results for thin shells in the analysis [102–104], for which the wall tension in equilibrium is nearly

independent of the material properties. The aneurysm wall was modeled as a neo-Hookean material, with Young's modulus of 1 MPa and Poisson's ratio of 0.49. Briefly, the 3D geometry with surface mesh was reconstructed from 3DRA images, taken before tissue harvest, using Mimics (Materialise, Leuven, Belgium) and further re-meshed in Meshmixer (Autodesk, San Rafael, CA) to increase the mesh quality. The geometry was then imported in Preview (FEBio, University of Utah, UT and Columbia University, NY) where triangular shell elements were generated with an extensible director formulation with three displacement degrees of freedom and three director degrees of freedom [105,106]. Wall thickness was set to the case specific average wall thickness as measured in the harvested tissue. As boundary conditions, a stress vector normal to the surface with magnitude of 15.5 kPa was applied at the inner wall and the outer wall was left stress free, corresponding to a transmural pressure of 15.5 kPa (116 mmHg) [107]. The edges at the boundary of the vascular model were fixed. Approximate solutions to the equilibrium equations were obtained using the nonlinear finite element based open source software suite within FEBio. The ratio of the second principal stress and first principal stress (σ_2/σ_1) was then calculated.

3.2.6 Structurally Motivated Constitutive Equation for the Remodeled Wall

A central objective of this work is to identify the physical mechanisms by which growth and remodeling occurs and develop a general structural form for the passive response of the remodeled wall, valid at a single time point, including the possibility of new layers and remodeling of existing layers. Such a model can be used to guide future experimental and computational studies of temporal changes to the aneurysm wall during growth and remodeling. In this section, we briefly outline the form of the structurally motivated constitutive model to be used with the

experimental results, providing sufficient generality here to capture the mechanisms identified in this work. Additional details are included in Appendix A.

The average stress tensor over the cross section of the aneurysm wall is assumed to arise from the contributions of *N* wall layers, each of which has passive contributions from collagen fibers, ground matrix and elastin (*i*=1,2, …N). For simplicity, here the ground matrix and elastin will be combined in a single mechanism, with stress tensor $\boldsymbol{\sigma_{gi}}$, assumed to be Neo-Hookean with

$$\boldsymbol{\sigma_{gi}} = \alpha_i \, \boldsymbol{b} \qquad \textbf{3-4}$$

where $\boldsymbol{b} = \boldsymbol{F}\boldsymbol{F}^{\boldsymbol{T}}$ and $\boldsymbol{F}$ is the deformation gradient associated with the mapping from reference to the current configurations and α_i is the shear modulus of layer *i*.

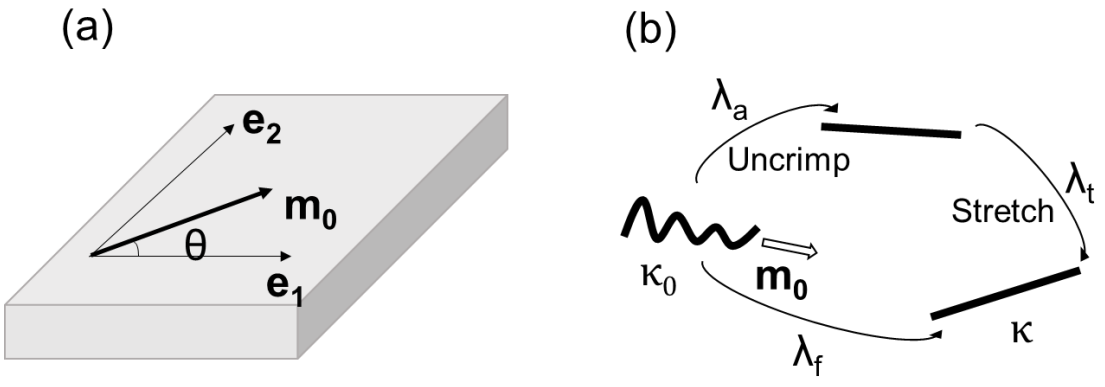

Figure 10 Schematic of coordinates and mapping used for fiber kinematics. (a) Unit vector m_0 represents arbitrary fiber direction with respect to Cartesian coordinate system (e_1 is circumferential direction, e_2 is longitudinal direction). (b) Schematic of fiber and associated fiber stretch during loading.

The collagen fiber response for arbitrary layer *i*, $\boldsymbol{\sigma_{fi}}$ arises from the collective response of an ensemble of extensible fibers with a distribution of orientations. Using local Cartesian coordinates with unit base vectors ($\boldsymbol{e_1}$, $\boldsymbol{e_2}$), Figure 10(a), an arbitrary fiber with direction $\boldsymbol{m_0}$ in reference configuration κ_0, can be written as $\boldsymbol{m_0} = cos\theta\boldsymbol{e_1} + sin\theta\boldsymbol{e_2}$. The strain energy function of collagen fibers in each layer is then constructed by integrating the response of fibers in that layer over all directions [52,108],

$$W_{fi} = \frac{1}{\pi}\int_0^{\pi} \rho_i(\theta)\, w_{fi} d\theta \qquad \textbf{3-5}$$

where $\rho_i(\theta)$ is the PDF of fiber orientation, chosen as a bimodal von Mises distribution, Appendix A. The PDF was determined by maximum likelihood estimation [109] using Matlab (R2017a, MathWorks Inc. Natick, MA) based on collagen fiber orientations measured from the MPM stacks. In general, a single collagen fiber will have a wavy conformation in κ_0, Figure 10(b), and will not be recruited until $\lambda_f = \lambda_a$, where λ_f is the stretch of material element during deformation from κ_0 to κ and λ_a is the activation stretch, a material property. The value of λ_f can be obtained from the kinematic relation ${\lambda_f}^2 = \boldsymbol{C}:\boldsymbol{m_0}\otimes\boldsymbol{m_0}$ and $\boldsymbol{C} = \boldsymbol{F^T F}$. Therefore, the strain energy of fibers in layer *i*, denoted as w_{fi} in (5) depends on the true fiber stretch $\lambda_t = \lambda_f/\lambda_a$,

$$w_{fi} = \frac{\beta_i}{2}({\lambda_t}^2 - 1)^2 \cdot H(\lambda_t - 1) \qquad \textbf{3-6}$$

where β_i is the stiffness of fibers in layer i. Here, the Heaviside function is used to switch off the contribution of the fiber to the strain energy function at stretches below this critical level.

$$H(\lambda_t - 1) = \begin{cases} 0 & if\ \lambda_t \leq 1 \\ 1 & if\ \lambda_t > 1 \end{cases} \quad \textbf{3-7}$$

The resulting equation for collagen fiber response of layer i is then,

$$\boldsymbol{\sigma_{fi}} = \boldsymbol{F}\left\{\frac{2}{\pi}\int_0^{\pi} \rho_{i(\theta)} \frac{\partial w_{fi}}{\partial {\lambda_f}^2} \boldsymbol{m_0} \otimes \boldsymbol{m_0}\, d\theta\right\}\boldsymbol{F^T} \quad \textbf{3-8}$$

As each layer only occupies a fraction of the cross section,

$$\boldsymbol{\sigma} = -p\boldsymbol{I} + \sum_{i=1}^{N} \gamma_i(\mu_i \boldsymbol{\sigma_{fi}} + (1-\mu_i)\boldsymbol{\sigma_{gi}}) \quad \textbf{3-9}$$

where p is the Lagrange multiplier arising from the constraint of incompressibility, γ_i is the thickness fraction of layer i and μ_i is the areal fraction of collagen fibers in cross section of layer i. Combining the Equation 3-4 and Equation 3-8 in Equation 3-9,

$$\boldsymbol{\sigma} = -p\boldsymbol{I} + \boldsymbol{b}\sum_{i=1}^{N}\gamma_i(1-\mu_i)\alpha_i + \frac{2}{\pi}\sum_{i=1}^{N}\gamma_i\mu_i\boldsymbol{F}\left\{\int_0^{\pi}\rho_{i(\theta)}\frac{\partial w_{fi}}{\partial {\lambda_f}^2}\boldsymbol{m_0}\otimes\boldsymbol{m_0}\,d\theta\right\}\boldsymbol{F^T} \qquad \textbf{3-10}$$

To determine the material parameters from uniaxial tension experiments, the least-squares objective function was minimized using interior-point optimization algorithm in Matlab as detailed in the Appendix A.2.

3.2.7 Statistical Analysis

Statistical analysis was conducted using IBM SPSS Statistics (version 25, IBM Corp, Armonk, N.Y., USA). The assumptions of normality and homogeneity of variance were tested first using Shapiro-Wilk test and Levene's test, respectively. Welch's t-test was used to test whether the mean values of a certain property (mechanical properties or AI of one layer) of control arteries and aneurysms were statistically different. For comparing means of mechanical properties of control arteries and aneurysms of different time points, the Welch's ANOVA followed by the Games-Howell post hoc was performed. The independent samples T-test was used to compare means of fiber tortuosity of different layers. A two-tailed p value less than 0.05 was considered to be statistically significant. 95% confidence intervals were calculated and reported.

3.3 Results

3.3.1 Collagen Fiber Remodeling in Response to Altered Loading in the Aneurysm Wall

3.3.1.1 Shift to Increased Longitudinal Loading after Aneurysm Formation

As noted above, aneurysm formation involves ligation of an approximately cylindrical vessel. Hence, after ligation, the intramural loads in the vessel shift to approximately those in a capped cylinder where the well-known equilibrium solution (Laplace's Law) for the ratio of principal stresses in the cylindrical region ($\sigma_2/\sigma_1 = \sigma_{zz}/\sigma_{\theta\theta}$) is 0.5.

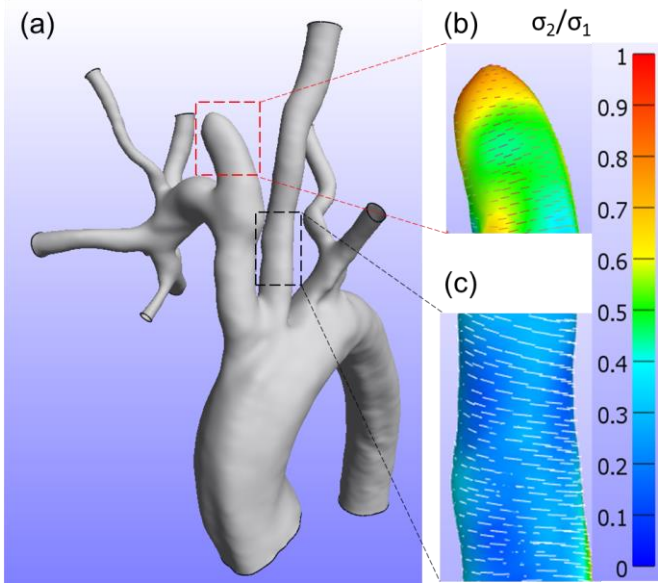

Figure 11 Shift to a more biaxial load state after aneurysm formation. (a) 3D reconstruction of the vasculature from DSA data from a representative two week case (H396). (b, c) Contour plots of the ratio of the principal Cauchy stress components σ_2/σ_1. The direction of the first principal stress is shown (arrows), demonstrating that σ_1 and σ_2 are approximately in the circumferential and longitudinal directions, respectively. In the aneurysm wall (b), the longitudinal stress is generally at least half the circumferential stress due to the end cap that is formed after vessel ligation. In contrast, in the control arteries (c), longitudinal stress is much smaller relative to circumferential stress

Similarly, the ratio of principal stresses in the spherical cap region can be estimated from equilibrium as 1.0. These results are consistent with those found from the 3D finite element analysis of the intramural stresses in the reconstructed aneurysm wall (average value of σ_2/σ_1 = 0.55±0.02), Figure 11(b). In contrast, in the (nonligated) control artery, the average value of σ_2/σ_1 is 0.27±0.02, Figure 11(c). Namely, after aneurysm formation, the contribution of longitudinal stress relative to circumferential stress increases approximately two fold in the bulk of the aneurysm.

3.3.1.2 First Phase Remodeling - Formation of New Layer between Media and Adventitia

The overall structure of the artery and aneurysm walls is most easily seen from the MPM images of wall cross sections, Figure 12(b, f). For the control artery, the media has a layered elastic lamellae, visible from the two-photon signal (green) with collagen fibers visible from the SHG signal (red), Figure 12(b). The adventitia is distinct, with increased SHG signal in the collagen fibers and no elastic lamellae. In the projected MPM stacks obtained from en face imaging from the luminal side of the unloaded control artery, the media collagen fibers can be seen to be highly aligned in the circumferential direction (AI = 0.88 ± 0.06), Figure 12(d). The layered elastic lamellae in the media are also visible in en face MPM images of the control artery, Figure 12(a). Adventitial fibers display a wider distribution in collagen fiber orientation compared with the media, though with a preferred circumferential direction (AI = 0.46 ± 0.15), Figure 12(c). Collagen fiber tortuosity is significantly greater ((p < 0.001, 95% CI [0.13, 0.18]) in the adventitia layer (1.23 ± 0.02) compared with the medial layer (1.07 ± 0.01), Figure 12(c, d).

In contrast, at two weeks after aneurysm creation elastin was sparse, dropping from 96% to 23% in areal coverage Figure 13(a,b). By 4 weeks, almost all elastin was gone, leaving only 4% coverage, Figure 13(c). Consistent with these images from the planar stacks, only remnants of elastin were visible in MPM images of the cross sections of the aneurysm wall, Figure 12(f).

In the remodeled aneurysm, a first phase of remodeling was seen as the development of an additional layer of collagen fibers between the media and adventitia layers, Figure 12(h) and Figure 14. The new layer was found in 3 out of 5 cases for the two-week group and in all cases at later time points (4 weeks, 8 weeks, 12 weeks). The average thickness of the new layer across all times points was 50.6 ± 14.3 μm, Table 4.

This new layer was clearly distinct from the neighboring media and adventitia, with qualitatively different fiber morphology and signal intensity in the MPM images, Figure 12(g,h,i). In particular, the tortuosity in the new layer was consistently low (1.08 ± 0.02) in contrast to the high tortuosity in the adventitial layer (tortuosity = 1.22 ± 0.03), Figure 12(g). The distribution of fiber orientation of the new layer (*AI* = 0.56 ± 0.15) clearly differentiated it from the adjacent medial layer where the fibers were circumferentially aligned (*AI* = 0.78 ± 0.12) with a weaker SHG signal compared with the new layer, Figure 15(d).

While the orientation in the aneurysm adventitia appeared similar on average to that in the new layer (*AI* = 0.55 ± 0.17), the adventitial fiber alignment varied greatly across samples, with no association with remodeling time. There were 8 cases with an *AI* value less than 0.5, 3 cases with an *AI* value larger than 0.7, and 11 cases with values within this range.

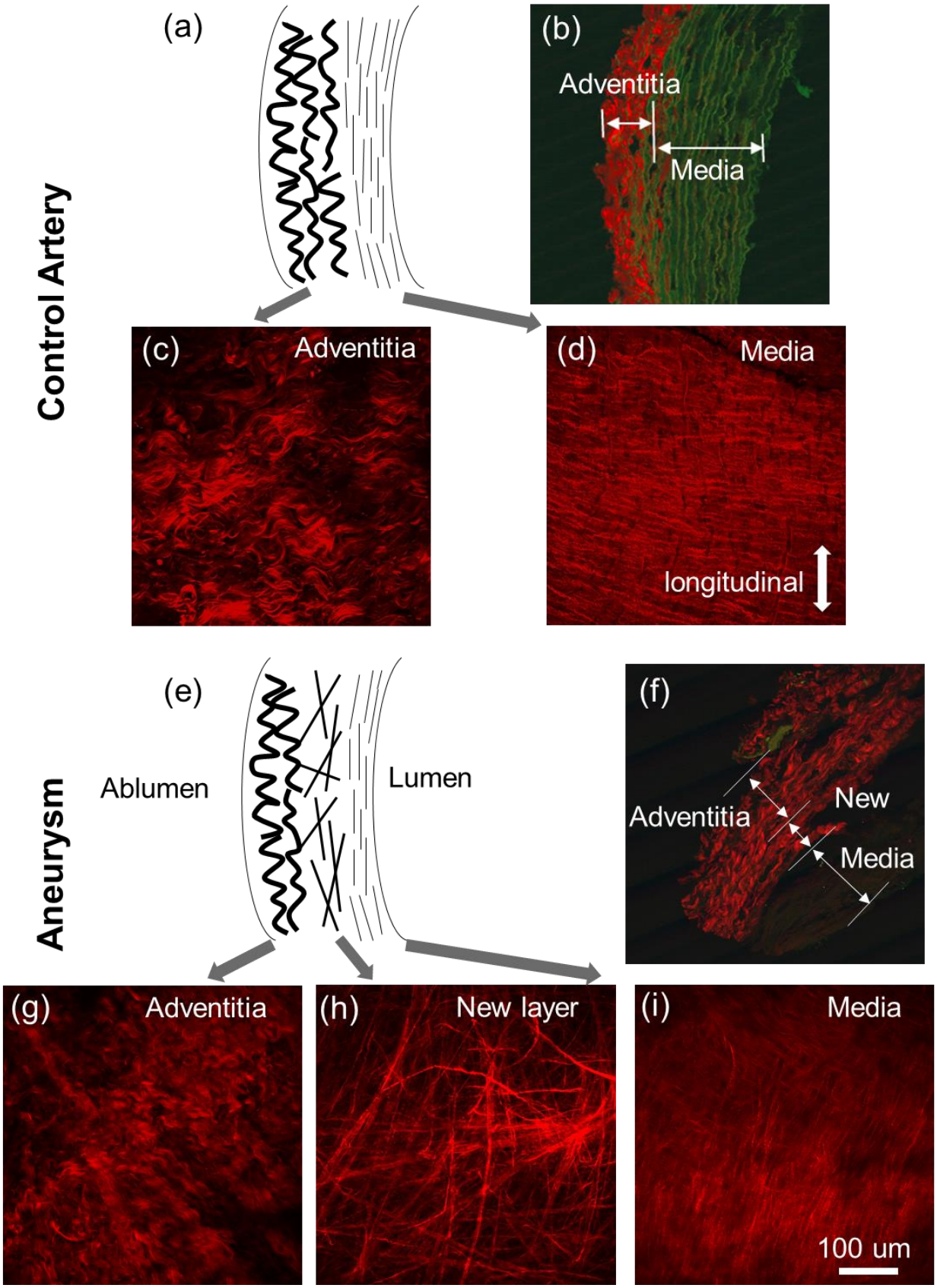
Control Artery
(a)
(b)
Adventitia
Media
(c)
Adventitia
(d)
Media
longitudinal
Aneurysm
(e)
Ablumen
Lumen
(f)
Adventitia
New
Media
(g)
Adventitia
(h)
New layer
(i)
Media
100 um

Figure 12 Comparison of wall layers in artery and aneurysm wall. Wall structure of control artery (a-d) and aneurysm in (e-i) as seen using multiphoton imaging with collagen fibers in red (SHG signal) and elastin fibers in green (2PE signal). (a) schematic of layered organization of wall of control artery, (b) cross section of artery wall showing elastin layers in media and collagen fibers in both medial and adventitial layers. (c,d) projected substacks from enface imaging images. Wall layers in aneurysm wall with (e) schematic of layered organization of wall of aneurysm, (f) cross section of IA wall showing an additional layer between the media and adventitial layers. (g-i) Substacks obtained from enface imaging for each of three wall layers in illustrative 8 week case (H629). The *AI* values for each image: (c) 0.49; (d) 0.93; (g) 0.62; (h) 0.44; (i) 0.50.

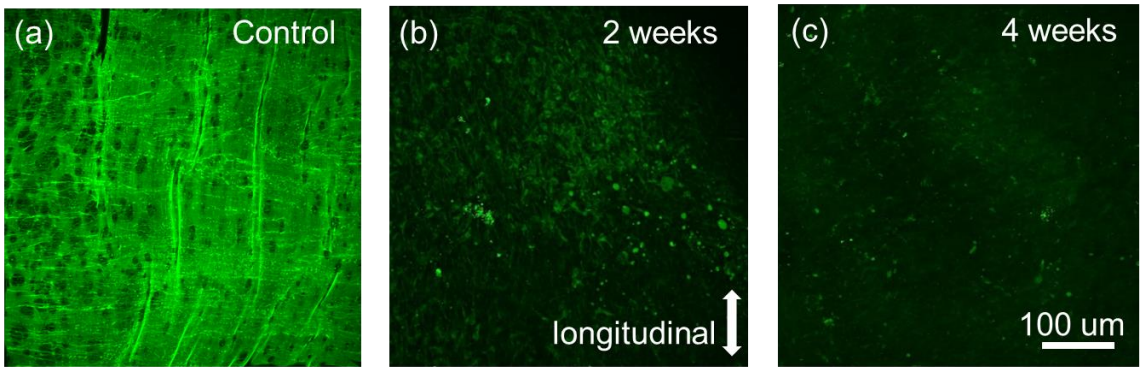

Figure 13 Evolution of elastin layers after aneurysm initiation. Projected stacks of MPM images showing elastin (2PE signal) of (a) control artery with area coverage of 96%, (b) aneurysm wall 2 weeks after creation with area coverage of 23%, and (c) 4 weeks after creation with area coverage of 4%. The area fraction was analyzed by ImageJ (NIH, MD, USA).

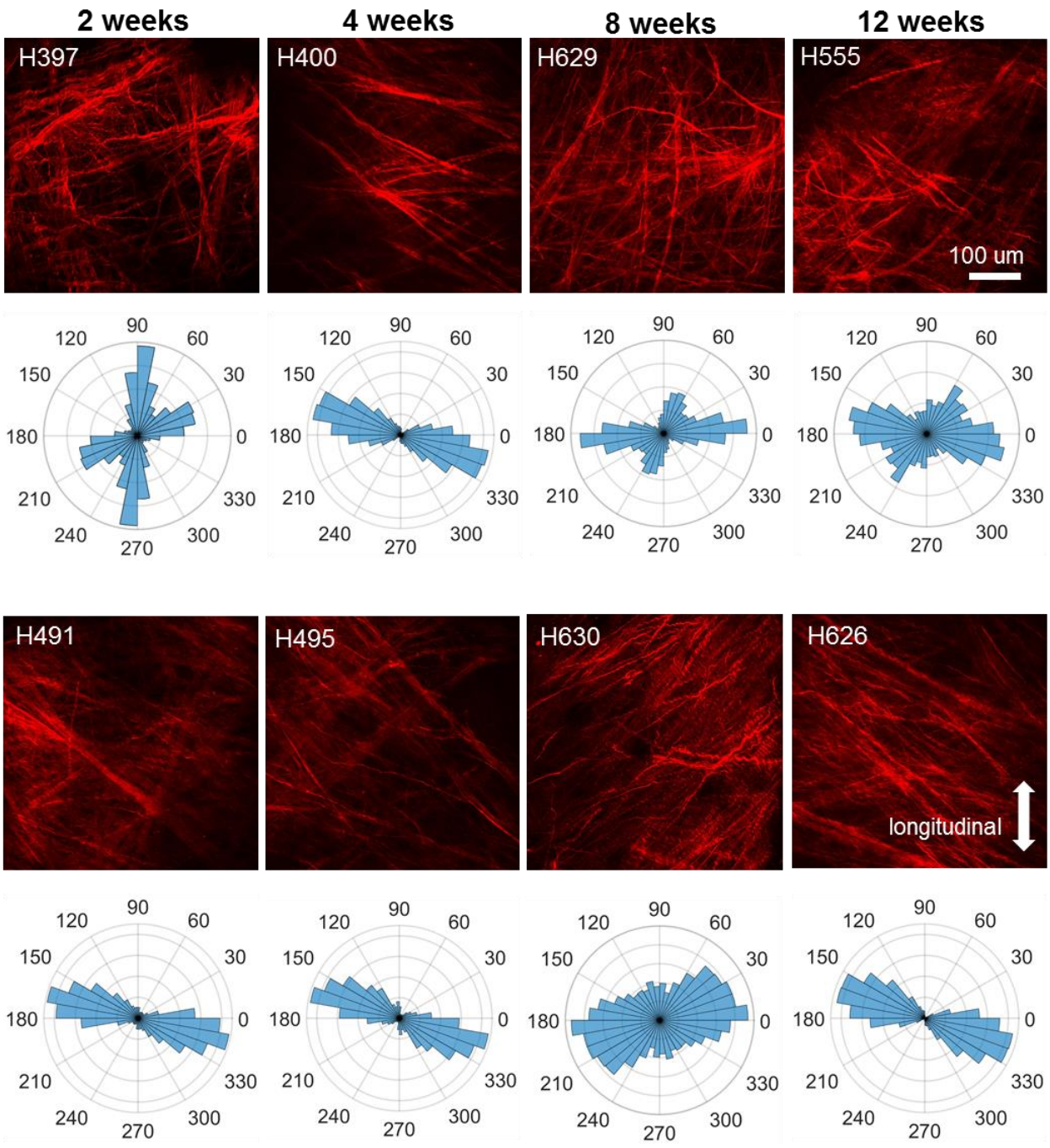

Figure 14 New collagen layer seen as early as two weeks. Substacks of MPM imaging of new wall layer, for representative cases from all four time points. Projected MPM images show wide distribution of collagen fiber orientation (*AI* = 0.56 ± 0.15, average over all samples). Circumferential orientation is 0 or 180 in the circular histogram. Longitudinal orientation is 90 or 270.

Table 4 Shape features and mechanical properties in longitudinal loading for aneurysms and control arteries across all samples

time	Case #	Thickness (μm)	Inner diameter (mm)	Height (mm)	New layer thickness (μm)	Ultimate stretch	Ultimate stress (Cauchy) (MPa)	Ultimate stress (1st PK) (MPa)
Control	H400-c	250	2.9	-	-	2.54	1.47	0.58
	H491-c	290	2.8	-	-	2.82	2.39	0.85
	H629-c	270	2.9	-	-	2.64	2.37	0.9
2 weeks	H491	240	3.3	9.5	64	1.68	5.76	3.43
	H492	440	3.2	11.0	-	2.14	5.31	2.48
	H493	300	3.2	8.9	52	1.51	2.92	1.93
	H396	420	2.8	8.2	-	-	-	-
	H397	400	3.6	12.1	60	-	-	-
4 weeks	H398	370	3.5	10.0	58	1.58	1.8	1.14
	H399	280	4.9	13.7	60	1.93	8.29	4.3
	H400	340	5	13.8	64	1.74	2.11	1.21
	H494	370	2.7	6.7	50	1.82	6.86	3.77
	H495	310	3.1	9.3	30	-	-	-
8 weeks	H551	350	5.1	10.0	74	2.02	4.78	2.37
	H552	480	5.1	10.5	66	-	-	-
	H553	330	4.8	8.6	30	2.58	10.85	4.21
	H628	460	4.5	9.8	40	-	-	-
	H629	330	5.2	8.9	32	1.5	1.99	1.33
	H630	280	6.1	12.5	40	2.13	13.56	6.37
12 weeks	H554	340	6.5	14.1	58	1.52	6.15	4.05
	H555	280	2.4	6.3	60	2.01	13.21	6.57
	H556	370	3.2	10.6	54	2.45	13.22	5.4
	H625	180	5.2	13.2	30	1.59	1.72	1.08
	H626	300	4.2	5.1	60	2.26	10.57	4.68
	H627	360	3.7	13.9	30	-	-	-

3.3.1.3 Second Phase Remodeling – Reorientation of Medial Collagen Fibers

In addition to the creation of a new layer, a later stage of remodeling was seen within the medial layer. This medial remodeling was only found at later time points, 8 weeks (5 out of 6) and 12 weeks (5 out of 6). In particular, the media of the later time points aneurysms adapted to the increased longitudinal load through changes in fiber orientation which varied across the thickness ($AI = 0.51 \pm 0.17$) and was statistically different from the earlier time points cases ($AI = 0.65 \pm 0.10$) ($p < 0.037$, 95% CI [-0.28, -0.01]), Figure 15. Whereas fibers in the outer media maintained the circumferential orientation found in the control, Fig, 15(a,d), those in the inner media became highly aligned in the longitudinal direction - the direction of increased load following aneurysm formation, Figure 15(a,b). A transition regime existed between these regions which contained both the circumferential and longitudinal alignment from the neighboring regions, Figure 15(a,c). The fiber tortuosity was unchanged in the remodeled medial layer (tortuosity = 1.07 ± 0.01 in control and remodeled media).

3.3.2 Capacity of Collagen Fibers for Longitudinal Load Bearing

3.3.2.1 Collagen Fibers in Control Artery Show Little Capacity for Contribution to Longitudinal Load Bearing

For the control arteries, the alignment of the medial collagen fibers remained circumferential throughout the wall thickness even under increasing stretch. This can be seen both qualitatively in the MPM images and quantitatively in the heat maps of fiber orientation as a function of stretch, even at stretches as high as 2.4, Figure 16. The adventitial fibers, which were highly tortuous (tortuosity = 1.26) with a distributed orientation in the unloaded state, remained tortuous even at $\lambda = 2$ (tortuosity = 1.14).

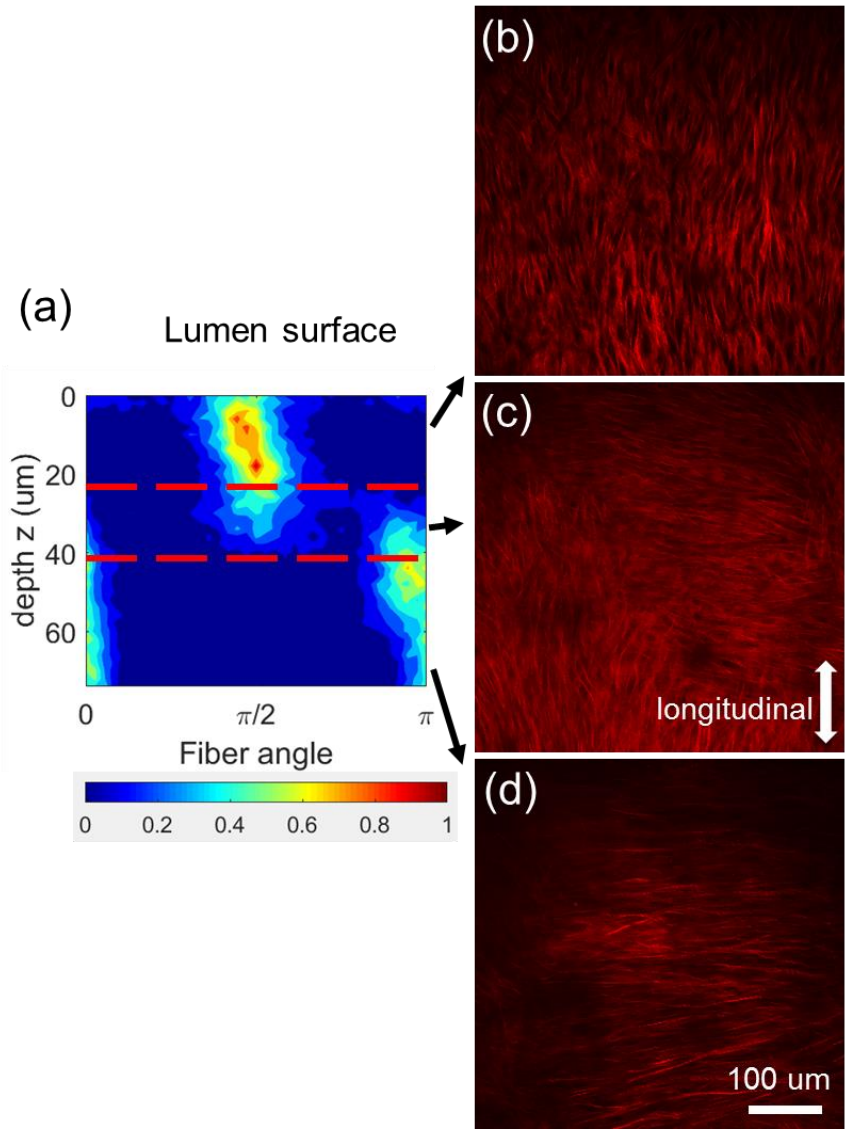

Figure 15 Remodeled media shows transition of collagen fiber orientation from longitudinal to circumferential direction. Collagen fibers (SHG signal) in substacks of MPM images across the medial layer for a representative 8 week case (H551) and associated heat map of distribution of fiber orientation. (a) Heat map of distribution of fiber angle as a function of distance from lumen surface. Circumferential direction is 0 and π and longitudinal direction is π/2. Fiber distribution is normalized to range from zero to one; (b) In inner media, (depth 0-20 μm), collagen fibers are largely aligned in longitudinal direction; (c) In mid-region of media, (depth 20-40 μm), fibers display a more dispersed distribution; (d) In outer media, (depth 40-80 μm), fibers are largely circumferentially aligned.

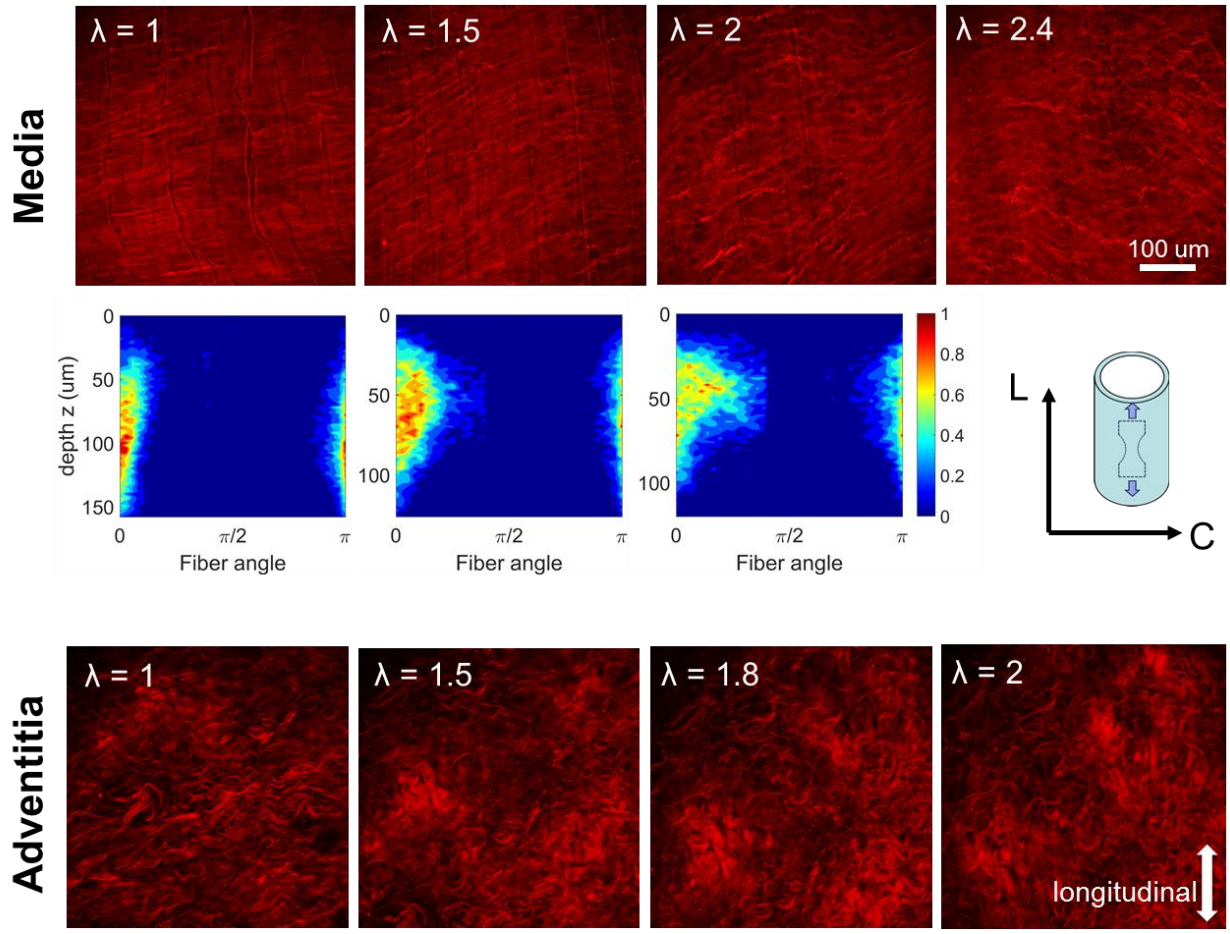

Figure 16 Collagen fibers in control artery show little recruitment even under substantial longitudinal stretch. 1st row: Projected stacks of MPM images show medial collagen fibers are largely circumferentially aligned in the unloaded state ($\lambda = 1$). 2nd row: Contours of fiber angle as a function of wall depth show largely circumferential alignment throughout the wall thickness in the unloaded state. With increasing stretch there is only a modest reorientation of fiber angle and fibers remain wavy and unrecruited, even at stretch up to 2.4. 3rd row: The undulations in the adventitial collagen similarly remain unrecruited even at stretch of 2.

3.3.2.2 Remodeled Collagen Fibers in the Aneurysm Wall Reorient under Longitudinal Loading

In contrast, in the remodeled aneurysm, collagen fibers in the new layer demonstrated their capacity to reorient under longitudinal loading, Figure 17. By a stretch of λ=1.4, all fibers in the new layer appear to be realigned in the loading direction, as seen both directly in the MPM images as well as in the contour plots of fiber orientation, Figure 17. As just noted, the medial collagen fibers remodeled in response to the increased longitudinal load, shifting from a dominant circumferential to longitudinal alignment. Under axial loading, the medial fibers sharpened their longitudinal alignment, Figure 18.

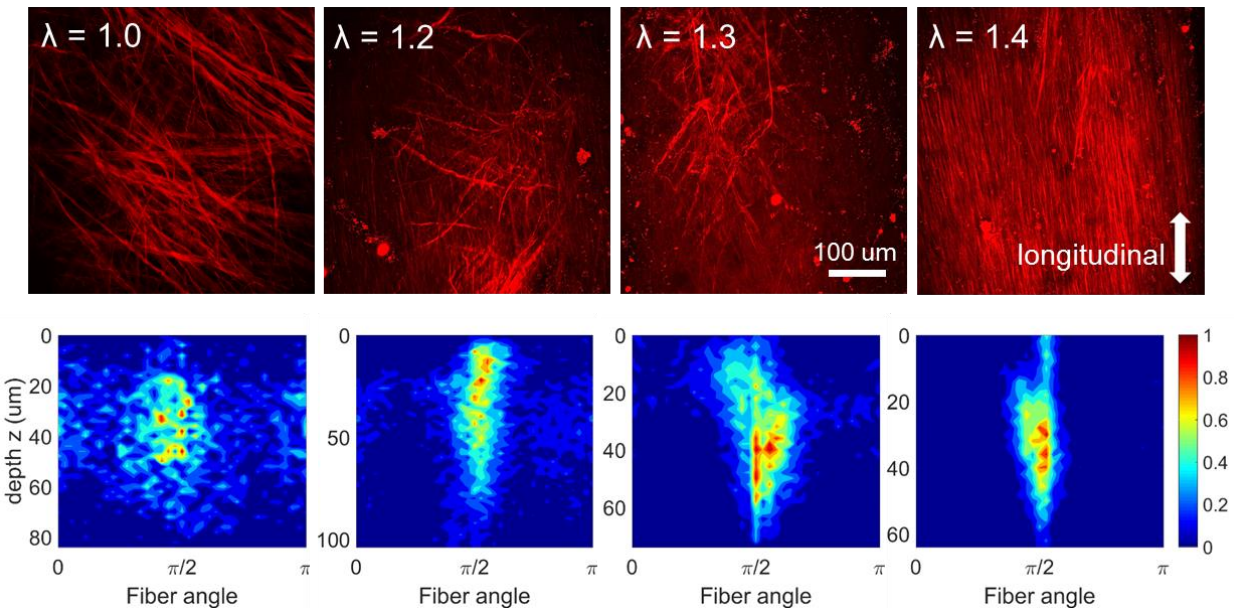

Figure 17 Fibers in new layer reorient under longitudinal load. With increasing axial load, collagen fibers in new layer show reorientation in the loading direction ($\pi/2$), and nearly complete alignment by stretch of 1.4 (case H629, 8 weeks).

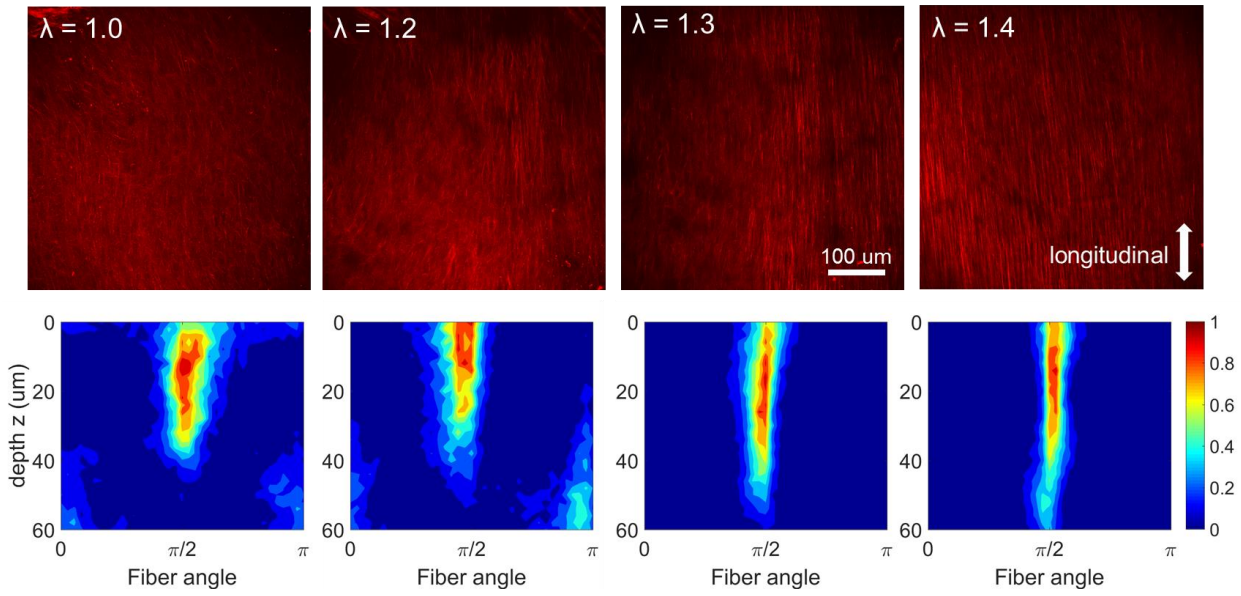

Figure 18 Collagen fibers in remodeled media of aneurysm further align under longitudinal loading (Case H626, 12 weeks). Heat maps of fiber distribution of collagen fibers across medial layer showing increasing longitudinal alignment with stretch across medial layer.

3.3.3 Strength under Longitudinal Loads

The ultimate strength of the aneurysm wall under longitudinal loading was significantly greater than that in the control artery (p = 0.001, 95% CI [2.73, 7.11]) and increased on average over time, Figure 19(a). The average ultimate stress for the aneurysm wall under longitudinal loading was 6.82±4.18 MPa (n = 16), three times greater than that of the control artery which averaged 2.07±0.43 MPa (n = 3), Table 4. The lower ultimate stress in the control artery under longitudinal loading is consistent with the lack of recruitment of collagen fibers in this loading direction. While the aneurysm wall increased in strength on average, there was a great

heterogeneity even at similar time points, Figure 19(a). Some remodeled aneurysms showed substantial increase in strength, Figure 19(a). To emphasize this difference, samples with above and below average strength were designated differently, (blue diamonds and red circles, respectively), Figure 19(a). Due to this spread, there is no significant difference in strength between control arteries and aneurysms of different time points. The average ultimate stretch of the control artery was 2.67±0.12 and statistically higher than the average ultimate stretch of 1.9±0.33 seen in the aneurysm wall ($p < 0.001$, 95% CI [0.49, 1.04]), Figure 19(b), consistent with the loss of elastin in the aneurysm wall.

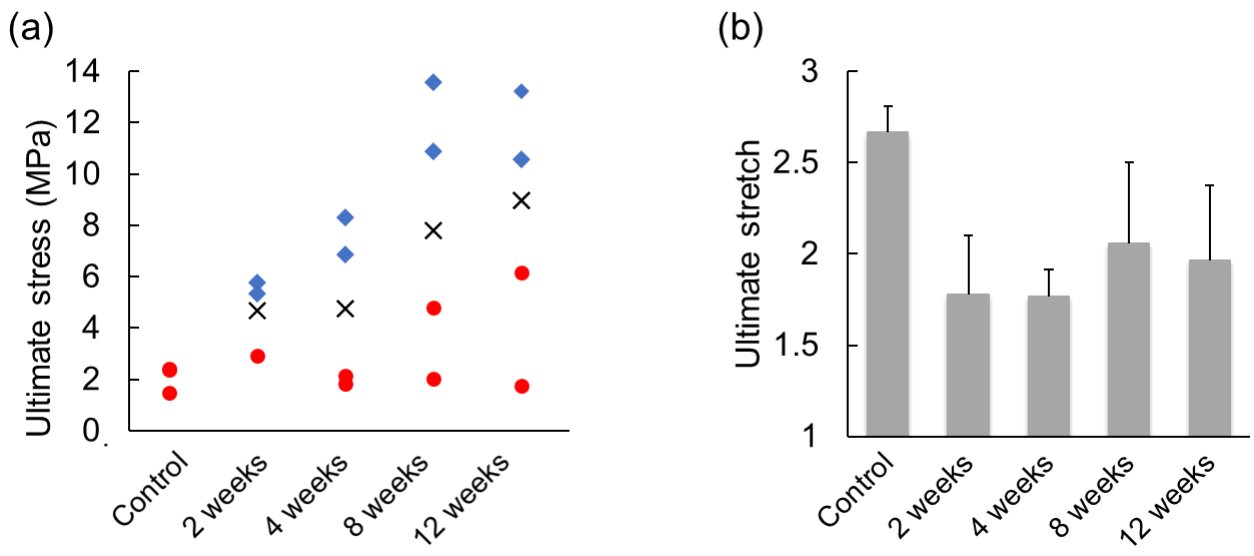

Figure 19 Failure properties of longitudinal samples of control artery and aneurysm wall as a function of remodeling time. (a) Ultimate Cauchy stress of all samples, split into below average strength (red circles) and above average strength (blue diamond), with average values for each time point denoted by "x". All above average cases have strength greater than 5 MPa. (b) Average ultimate stretch for control and each time point, corresponding to data in (a). Error bar represents standard deviation. Ultimate stretch is the stretch corresponding to the ultimate (peak) stress during uniaxial failure testing.

3.3.4 Constitutive Equation for Remodeled Aneurysm Wall

In this section, results of the formation of a structurally motivated constitutive equation for the remodeled aneurysm wall are given. This new model includes the two mechanisms of remodeling identified in the experimental work, and is driven by the bioimaging and mechanical testing data. The model is illustrated on a single case using the general constitutive framework introduced in Section 3.2.6. For clarity, an overview of the equations and parameters are given in Table 5. The parameters are broken down into those that were directly measured from imaging data and those that were obtained as part of the parameter identification process from the uniaxial mechanical testing data. Briefly, directly measurable variables include the thickness of each wall layer, the areal fraction occupied by a wall component (e.g. collagen fibers) and characteristics of the collagen fibers (fiber orientation distribution, activation stretch). Parameters obtained from the regression analysis were those related to material stiffness. The details of the methods for obtaining the directly measured properties and the regression of the uniaxial testing data were provided in Section 3.2.6 and Appendix A.

We briefly elaborate on some of the modeling choices given in Table 5. As noted above, the remodeled aneurysm wall was found to display two mechanisms of adaption to increase longitudinal loading - creation of a new layer between the media and adventitia as well as remodeling of the medial collagen fibers. Based on these findings, N=3 layers are selected for the aneurysm wall, the media, new layer and adventitia. The endothelium is not considered to be load bearing in this work. In contrast, the control artery has only medial and advential layers (N=2).

Table 5 Overview of parameters in constitutive model

	Explanation	Source of Parameter acquisition	Equation	
γ	Thickness fraction of each layer	Obtained from MPM imaging. Equal to number of planar MPM images in that layer multiplied by spacing between images.	$\boldsymbol{\sigma} = -p\boldsymbol{I} + \sum_{i=1}^{N} \gamma_i(\mu_i \boldsymbol{\sigma_{fi}} + (1-\mu_i)\boldsymbol{\sigma_{gi}})$	3-9
μ	Area fraction of collagen fibers in cross section of each layer	Obtained from 3D reconstructed MPM image stack of SHG signal. Measured collagen area fraction in cross sections orthogonal to loading direction.		
λ_a	Activation stretch of fiber	Obtained directly from MPM stacks of SHG signal. Equal to average tortuosity of collagen fibers.	$w_{fi} = \frac{\beta_i}{2}\left(\left(\frac{\lambda_f}{\lambda_a}\right)^2 - 1\right)^2 \cdot H\left(\frac{\lambda_f}{\lambda_a} - 1\right)$	3-6
a_1, a_2, b_1, b_2	Parameters of bimodal orientation distribution function for fiber angle	Fit of fiber angle distribution that was measured directly from fiber tracing in stacks of MPM images for each wall layer.	$\rho(\theta) = \frac{1}{2I_0(b_1)} e^{b_1 cos2(\theta - a_1)} + \frac{1}{2I_0(b_2)} e^{b_2 \cos 2(\theta - a_2)}$	A-4
α	Isotropic material properties of ground matrix and elastin	Obtained as part of parameter identification from uniaxial data-longitudinal loading.	$\boldsymbol{\sigma} = -p\boldsymbol{I} + \boldsymbol{b}\sum_{i=1}^{N} \gamma_i(1-\mu_i)\alpha_i + \frac{2}{\pi}\sum_{i=1}^{N} \gamma_i \mu_i \boldsymbol{F}\left\{\int_0^{\pi} \rho_{i(\theta)} \frac{\partial w_{fi}}{\partial {\lambda_f}^2} \boldsymbol{m_0} \otimes \boldsymbol{m_0}\, d\theta\right\}\boldsymbol{F}^T$	3-10
β_m	Stiffness of collagen fiber in media layer	Obtained as part of parameter identification from uniaxial data-circumferential loading.		
β_n	Property of collagen in new layer	Obtained as part of parameter identification from uniaxial data-longitudinal loading.		

The collagen fibers in the adventitia layer remained wavy (unrecruited) throughout the subfailure loads considered for the constitutive modeling (Figure 16). Namely, the subfailure stretch levels were below the recruitment stretch of adventitial collagen. Therefore, for the loading conditions considered in this study, the adventitial layer did not contribute to the strain energy function for either the control artery or aneurysm tissue.

The material parameters α_i for the isotropic components were assumed to be the same for different layers. It was determined through a fit to the toe-region of the loading curve up to the activation stretch where the fibrous component was recruited to load bearing [110,111]. The collagen stiffness parameter β_m was obtained from parameter regression from uniaxial testing on circumferential strips of control artery. The constitutive model for the aneurysm wall included both medial layer and the new layer. The material constant for the collagen fibers in the medial layer (β_m) was assumed to remain constant during the remodeling process and therefore set equal to this same constant as obtained from the control artery. The stiffness of the newly deposited collagen fibers, β_n, was obtained as part of the parameter identification process using the uniaxial mechanical testing data on the aneurysm tissue. All the measured and fitted parameters are listed in Table 6. The fitted curve ($R^2 = 0.983$) along with experimental data are shown in Figure 20.

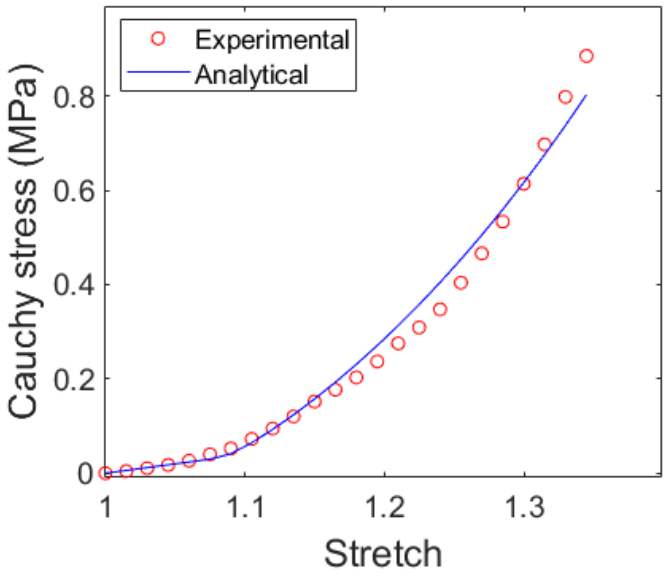

Figure 20 Experimental stress-stretch data (red dots) along with the fitted curve (solid) for case H400

Table 6 Results for measured and fitted parameters in constitutive model

Case	Layer	Measured Parameters			PDF				Fitted Parameters			
		γ	μ	λ_a	a_1	a_2	b_1	b_2	α (MPa)	β_a (MPa)	β_m (MPa)	β_n (MPa)
Control H495-c	media	0.62	0.45	1.07	0.01	3.07	14.95	2.72	0.19	-	0.83	-
	adventitia	0.38	0.42	1.25	2.14	3.01	0.99	3		-		
Aneurysm H400	media	0.11	0.44	1.08	0.27	0.62	4.35	1.07	0.17	-	0.83	12.28
	new layer	0.2	0.31	1.08	1.02	1.39	1.08	2.79		-		
	adventitia	0.69	0.42	1.22	0.86	1.53	0.49	1.93		-		

3.4 Discussion

The objective of this work was to investigate the physical mechanisms for remodeling collagen fibers in response to changing mechanical loads in an elastase induced model of saccular aneurysms in rabbits. Fundamental questions regarding the location of remodeling within the wall and the possibility of multiple stages in the remodeling process were addressed. Multiphoton microscopy and mechanical testing were used to evaluate the nature of this remodeling process.

This work is motivated by a need to understand mechanisms of wall remodeling in human aneurysms - fundamental knowledge that can impact patient treatment and risk assessment. It is well established that aneurysm geometries evolve in time [112], which in turn, leads to changes to the intramural loads and flow environment [11,113]. The response of the aneurysm wall to this changing mechanical state cannot be studied in patients and so animal models of the kind used here are needed. In the rabbit model, the application of elastase gradually disrupts the elastin layers thereby contributing to an increased sac diameter over time as well as rendering the extracellular matrix more similar to that of human aneurysms, where elastin is rarely found. Here we used this model to explore mechanisms by which the aneurysm wall can adapt to changing intramural loads under flow fields that have been shown to be similar to those found in human aneurysm sacs [93].

Prior work has also considered the impact of elastase degradation on the relationship between wall structure and mechanical function in aortas. In [114], it was shown that after 6 hours of elastase incubation, the elastin network was no longer visible in MPM images and the unloaded sample length increased sufficiently to cause recruitment (straightening) of the collagen fibers. We emphasize that the objective of the present study was to consider a more gradual change in the extracellular matrix (ECM). Therefore, in the current study, elastase was applied for only 20 minutes. Even after only 2 weeks post application, sparse elastin fibers remained in the aneurysm

wall, Figure 13(b). Moreover, the medial and adventitial collagen fibers retained their wavy structure in the unloaded state.

In this work, the creation of the aneurysm wall led to a shift in the intramural loads from predominantly circumferential to a more multi-axial loading state that is more typical of human saccular aneurysms. While it has been long recognized that altered blood flow and pressure can induce arterial remodeling such as changes in wall thickness and biomechanical response [115,116], vascular growth and remodeling due to changes in the multi-axial loading state has received little attention [117,118]. We found the remodeling response in the wall demonstrated two distinct phases, that were localized in different wall regions. The first phase occurred as early as 2 weeks after aneurysm creation and was characterized by the development of a new layer between the adventitia and media. This layer was composed of relatively sparse, multi-directional collagen fibers, Figure 12(h) and Figure 14. The fast deposition and distributed orientation of collagen fibers in this new layer, coupled with the low level of undulations in these fibers provided a mechanism for the wall to bear both longitudinal and circumferential loads, without extensive elongation. The MPM analysis of recruitment and reorientation of collagen fibers in the new layer during longitudinal loading, demonstrated that collagen fibers in this layer were recruited to longitudinal load bearing before the circumferentially aligned medial fibers and the highly undulated adventitial fibers. Namely, until some time between 4 and 8 weeks, only collagen in this new layer was recruited to longitudinal load bearing. A second, later phase of remodeling within the medial layer was seen in most 8 weeks and 12 weeks cases. In particular, in response to the in vivo increase in longitudinal loading, collagen fiber orientation in the media remodeled, changing from almost purely circumferential across the entire medial layer to containing a range of orientations that depended on radial position. The outer media remained largely circumferential,

while fibers in the inner media displayed a longitudinal alignment. These two regions were separated by a transition regime with both alignments, Figure 15.

The current work provides provocative information about possible mechanisms by which human aneurysms may adapt to changing mechanical loads. In earlier studies of human IAs, we also saw remodeled medial layers that similarly demonstrate plies with multiple directions [11,12], Figure 21. This earlier work, similarly employed MPM analysis of collagen fibers. The present results, identified a second mechanism that enables rapid response to acute changes in mechanical loading and brings to question the mechanisms by which the human IAs can stabilize after acute changes in geometry that might follow acute subfailure damage. In particular, if medial reorganization has a time frame of 8 weeks, is there similarly a second mechanism of remodeling in human IAs that can stabilize the wall prior to effective medial remodeling? We conjecture that this mechanism for rapid deposition of collagen fibers or some other mechanism must also exist in human aneurysms. In the future, we intend to investigate this conjecture as the capacity for rapid structural reinforcement will be essential for preventing catastrophic rupture in some IAs, and thereby be of vital clinical importance.

It has already been established that human unruptured IAs display both vulnerable and robust walls as seen in the ultimate failure stress [11]. In fact, one of the most important clinical objectives is to predict which unruptured aneurysms are vulnerable. Ideally, we will understand the physical cause for this vulnerability so that we can develop new treatments and methods of assessment. Interestingly, even in this study, where the rabbit aneurysms were developed in a systematic manner, their failure strength also showed great heterogeneity. However, no clear differences in collagen architecture, such as distributions and density of collagen fibers, could be found in the rabbit aneurysms to explain this heterogeneity. This suggests the difference in strength

could be due to some aspect of the fiber structure at the nano level, rather than the distribution and organization of fibers at the micro level. In future studies, electron microscopy will be used to evaluate difference in the collagen fibers.

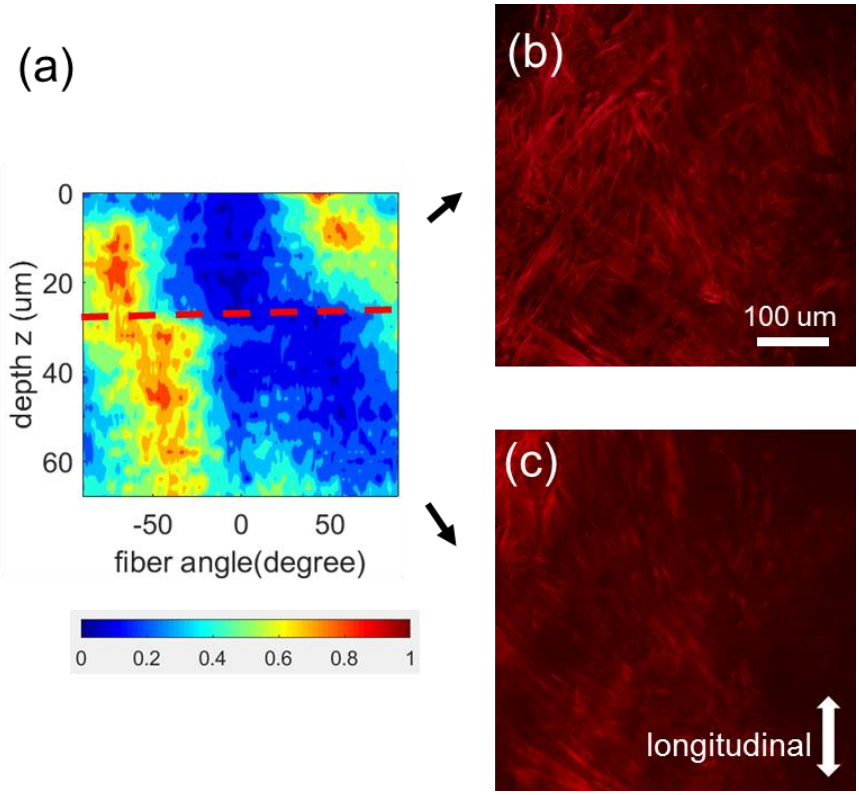

Figure 21 Remodeled medial collagen fibers of human aneurysm case similarly show transition between two orthogonal directions. (a) Distribution of fiber orientation as a function of depth. (b,c) Projected stacks of MPM stacks showing collagen fibers largely aligned in one direction in outer media (depth 30-70 μm), and displayed more dispersed distribution in inner media (depth 0-30 μm) orientations (Contour plot reproduced from [12]). This human aneurysm sample (CA-25) was obtained from a 53 year old female patient and had distinct medial like and adventitial like layers.

The discovery of these two mechanisms of remodeling is crucial for understanding how the vascular wall can adapt to changing loads on short and long time scales. Such information is essential for the development of meaningful growth and remodeling theories, which can in turn guide future experimental work. In the present study, we developed for the first time a structurally motivated constitutive model for the remodeled aneurysm wall, which is general enough to capture both modes of remodeling. With future applications of growth and remodeling in mind, a methodology was introduced to use the data obtained in this work to drive choices for material parameters in the constitutive model. Such models in turn will be invaluable in guiding future experimental studies.

Limitations and Future Directions:

The theoretical model presented here included some idealizations that can be relaxed in future works. While we did model the fibers with layer specific material properties (stiffness), we used a constant (average) value of recruitment stretch for each wall layer rather than using a distribution of recruitment stretches, such as we used in [52]. With respect to mechanically testing, while we did consider the biaxial response in subfailure loading, our failure testing was performed on uniaxial strips in the longitudinal direction, due to limitations in sample numbers. The longitudinal direction was chosen based on the need for adaptation in ECM to maintain wall structural integrity after aneurysm formation. While remodeling of fibers in both directions, were analyzed using MPM, it may be of interest in the future to also measure the circumferential properties in the aneurysm wall. Unless fibers are perfectly symmetric about the loading direction, a shear stress will be generated at the clamped region in uniaxial testing. In the mechanical tests, we did not measure this shear load, though we did include measurements of fiber angle in the

constitutive model. Furthermore, due to limitations in imaging depth, it was generally not possible to image through the entire adventitia in fresh samples. In future studies, optical clearing methods could be used to more fully probe possible modeling in the adventitial layer [119,120].

The relationship between hemodynamic factors and remodeling was not investigated in this work as the focus was on the adaption of the wall to increased longitudinal load. In fact, the flow field did not show significant differences as a function of time point. The magnitude of time averaged wall shear stress was uniformly low relative to the parent arteries. In all cases, the spatial average was less than 7 dynes/cm^2. The qualitative flow features were also similar across the models, displaying two transient vortices, driven by the inflow jet. There were differences between cases, such as the location of jet impingement and duration of the secondary vortex. In future studies, it could be interesting to analyze the association between local flow features such as jet impingement and endothelial cell morphology and function.

The current studies demonstrate relevance in several important areas between human IA walls and the walls of the elastase induced aneurysm model in rabbits. Even so, we must always question the relevance of the application of a given animal model to a particular aspect of a human disease. For example, the current study considered young animals. In future work, we intend to use older animals to explore the impact of age on the remodeling responses. Although the current study did not develop the temporally evolving constitutive models for growth and remodeling theories, it identified, for the first time, the mechanisms of remodeling in the rabbit model of saccular aneurysms. As such, this study provides essential information for the design and implementation of future growth and remodeling theories with applications to aneurysms. The stiffness of overall collagen component in the new layer is substantially higher than in the neighboring media layer. This trend is consistent with results on in vivo neo artery formation in

rats in which the collagen contribution from newly deposited collagen fibers was also stiffer than in control artery [29]. It should be noted that the stiffness parameter is not obtained from data normalized by fiber number, but rather by area fraction of collagen. Therefore, it cannot be used to compare individual fiber stiffness between layers. In future work, it would be valuable to perform a more extensive analysis of the collagen fibers themselves using, for example, electron microscopy.

This elastase induced aneurysm model in rabbits has already been recognized as a valuable model for developing new devices for treating cerebral aneurysms such as flow diverters [121–123]. The present study suggests this animal model may also provide an opportunity to evaluate the impact of these devices as well as pharmacological treatments on aneurysm wall remodeling.

3.5 Conclusion

Since collagen is the major passive load bearing component in the aneurysm wall, collagen remodeling in response to the evolving IA geometry is vital for maintaining a sustainable level of intramural loads and avoiding rupture. The current study directly evaluated collagen remodeling in the rabbit aneurysm model and identified two fundamentally different mechanisms of remodeling. The first occurred over the period of weeks and involved the development of a new wall layer. A second, later response, involved reorganization of the medial collagen fibers in response to sustained changes in load and occurred on the time scale of months. The second remodeling mechanism has been identified in human aneurysms. The first mechanism, though not yet reported in human IAs, suggests new areas of study in human IAs as it occurs over a relatively short time period in response to acute changes in load. Collectively, the results in this work suggest

the rabbit aneurysm model warrants further investigation as a tool for studying the evolution of human IAs and investigating new treatment strategies.

3.6 Acknowledgment

I would like to thank Dr. Robertson for her supervision and guidance in this chapter. I am grateful to the researchers at Mayo Clinic, Dr. Kallmes, Dr. Kadirvel, Dr. Ding and Dr. Dai, for creating the rabbit aneurysms used here and the analysis of endothelial cells (Appendix B.1.2). I also want to thank Dr. Watkins for the technical support of microscopic imaging.

4.0 Prevalence and Distribution of Calcification in Human Cerebral Arteries

4.1 Introduction

Vascular calcification is a pathological deposition of mineral within the vascular wall. It is a common phenomenon that is influenced by complex interactions between several factors, such as aging, diet and other pathologies [124,125]. At least two different types of pathological processes can lead to calcification accumulating in the vascular wall [126], atherosclerotic calcification (typically in the intima) and non-atherosclerotic calcification in the other layers. Atherosclerotic calcification is a slow, inflammation driven process and associated with lipid pools [127]. Non-atherosclerotic calcification occurs via rapid mineralization due to an upregulation of calcifying genes, typically in the absence of lipid pools [124,128,129]. In both cases, vascular calcification is considered to be an independent marker of increased cardiovascular risk, such as coronary mortality, myocardial infarction and stroke [130–135].

While the formation of vascular calcification is widely studied, its role in cerebral vascular disease has only received limited attention. Calcification as a rigid deposit in the artery wall has important biomechanical effects [23,136,137]. Size of calcification particles and distribution in the wall can alter the mechanical stress [138–142]. There are several imaging techniques, both *in vivo* and *in vitro*, that are commonly used for detection of calcification. Clinical computed tomography (CT) and Optical Coherence Tomography (OCT) are non-invasive approaches to study the prevalence and location of calcification in the cerebral artery wall [135,138,143,144]. Though clinical CT and OCT capture large calcification easily, they fail to detect micro-calcifications, which are conjectured to play an important role by causing local stress concentration [140].

Besides *in vivo* imaging techniques, histology studies can detect calcification and provide more details about type and location of calcification in the wall [144,145]. However, such studies only provide localized two dimensional structural information and can be time consuming to prepare. An alternative in vitro non-destructive technique, high resolution micro-computed tomography (micro-CT), can overcome such limitations in histology and provides a means of investigating the details of micro-calcifications in intact samples [25,146], though typically with lower resolution and without the option of additional staining.

Common sites of intracranial aneurysm occurrence are arterial bifurcations of the circle of Willis, a circular junction of arteries found in the inferior part of the brain. The calcification distribution in these regions compared to other locations remains unknown. A recent study using high resolution micro-CT found that calcification, both atherosclerotic and non-atherosclerotic, is more prevalent in intracranial aneurysms than previously reported, reporting a prevalence of 51 in 65 resected human aneurysm samples [25]. Moreover, this study provided a comprehensive exploration of the size and location distribution of calcification as small as 3 μm. It is not known whether this high prevalence of calcification is already present in the wall of cerebral vessels, especially the bifurcation regions where they originate, or whether this calcification develops as part of the pathology of IAs.

The objective of the current study is to determine the prevalence, distribution and type of calcification in internal carotid arteries (ICA) and three of the bifurcations associated with the ICA. Two of these bifurcations are located at the proximal and distal sides of the juncture of ICA and posterior communicating artery (PCOM). Aneurysms at the proximal PCOM bifurcation (PB-P) area and the distal PCOM bifurcation (PB-D) area account for approximately 25% of all intracranial aneurysms [147]. The other bifurcation considered here is the ICA bifurcation (ICA-

B) which is located at the juncture of the ICA, middle cerebral artery (MCA) and anterior cerebral artery (ACA). The ICA-B accounts for about 5% of all intracranial aneurysms (reports range from 2% to 9%) [148–150]. Twenty ICAs with bifurcations were scanned using high resolution micro-CT scans that detected calcifications down to 3 μm. The prevalence, distribution and type of calcification were analyzed and compared to intracranial aneurysms. Prevalence of calcification in these three bifurcations were measured and compared with the remaining ICA tissue as well as data for cerebral aneurysms.

4.2 Methods

4.2.1 Tissue Acquisition

Twenty circles of Willis were obtained during human autopsy (Alzheimer's Disease Research Center Brain Bank, University of Pittsburgh). Samples were fixed in 4% paraformaldehyde (PFA) within 5 hours after autopsy. Tissue segments with either the left or right ICA along with the PCOM bifurcation (if PCOM was present) and ICA bifurcation were cut from each circle of Willis, Figure 22(a, b). Clinical data were collected for each patient including age, sex, smoking, hypertension, hyperlipidemia, diabetes and neurodegenerative diagnosis.

4.2.2 Micro-CT Scanning

All samples were scanned using a high resolution micro-CT scanner (Skyscan 1272, Bruker Micro-CT, Kontich, Belgium) [25,65]. The scanning resolution was set to be 3 μm to capture

micro-calcifications. Following previously published protocols [25], samples were placed in a 1.5 mL microcentrifuge tube atop a moist gauze to prevent dehydration during scanning. The tube was mounted vertically on an attachment of micro-CT. Samples were scanned 180° around the vertical axis with a rotation step of 0.2° and a framing average of 8. The source voltage and current were set to be 50 kV and 200 μA. The scanning time was approximately 2 hours for each sample. Three-dimensional reconstructed images were created in NRecon (Bruker Micro-CT, Kontich, Belgium).

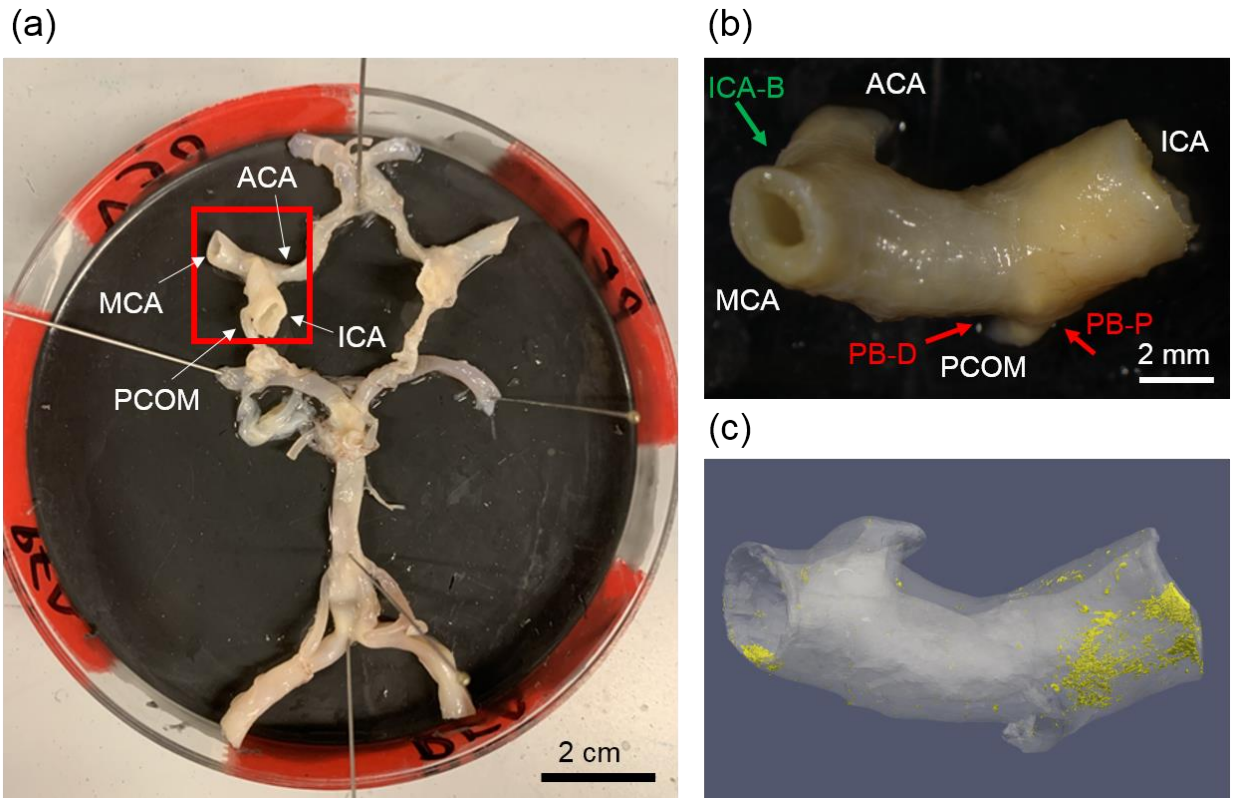

Figure 22 Circle of Willis and the anatomy for the segments included in current study. (a) Circle of Willis from human cadaver. (b) Representative arterial segment. The red arrows point to distal and proximal PCOM bifurcations (PB-D and PB-P, respetivey) and the green arrow points to ICA bifurcation (ICA-B). (c) 3D reconstruction from micro-CT scan. The grey region is non-calcified tissue and the yellow shows the calcificed particles in the wall.

4.2.3 Mesh Generation

The surface mesh for calcification and non-calcified tissues were generated in Simpleware ScanIP (Synopsys, Mountain View, USA) as previously described [25,146,151]. Briefly, the reconstructed images created in NRecon were segmented into one mask of all tissue and one mask for calcification. The tissue mask was created using segmentation filters including thresholding, flood fill and additional morphological filters such as eroding and dilating to remove unwanted components. Then, recursive Gaussian smoothing was performed on the mask. The calcification was separated from non-calcified tissue by thresholding based on increased grayscale value following by a series of Boolean operations to remove surface noises. A general module in ScanIP was used to generate volume fraction of calcification based on the segmented mask. Geometric information including diameter, volume and centroid of individual calcification particle was analyzed using the particle analysis module in ScanIP. The major diameter of the bounding ellipsoid of each calcification particle was used to compare the particle size. The surface mesh consisting of triangular elements was generated for each mask, Figure 22(c).

4.2.4 Classification of Wall Types

The presence of lipid pools could be detected in micro-CT images of the sample cross section due to its lower grayscale value [25]. The arterial walls were classified into 3 different types based on the association of calcification with lipid pools as previously described [25]. Briefly, Type I refers to samples contained only calcification without lipid pools. Type II refers to samples with lipid that is not co-localized with calcified tissue. Type III walls contain colocalized calcification and lipid pools. As in the prior studies on aneurysms [25], calcification particles were

categorized further according to their sizes. Micro-calcifications have a diameter less than 500 μm, meso-calcifications have a diameter between 500 to 1000 μm, and macro-calcifications have a diameter that larger than 1000 μm.

4.2.5 Bifurcation Identification

4.2.5.1 Vascular Branch Splitting

The surface mesh of the arterial tissue was preprocessed with several different operations in Meshmixer (Autodesk, San Rafael, CA). First, it was smoothed to eliminate surface defects. To facilitate the calculation of centerlines, short branches were extruded with a length between 2 to 3 mm. Finally, the inner and outer surfaces were separated and exported.

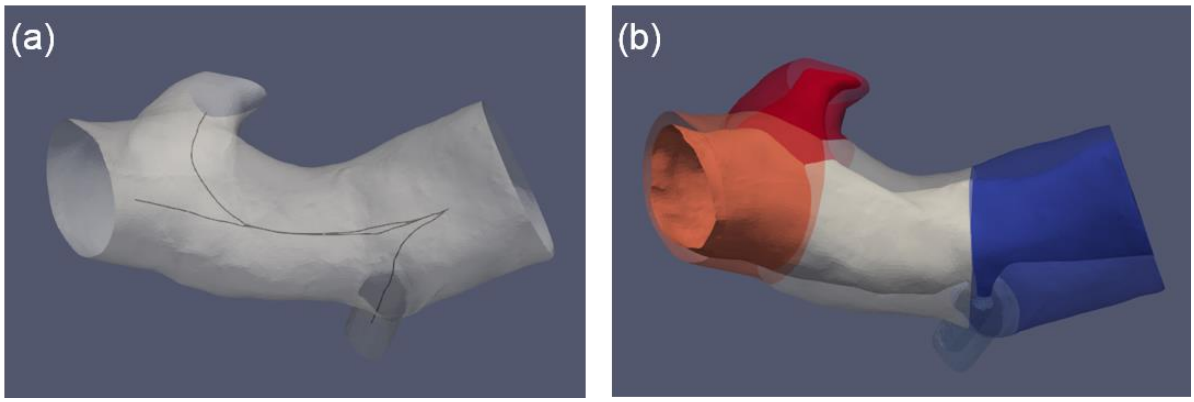

Figure 23 Illustration of methodology for splitting regions based on centerlines. (a) Centerlines of outer surface. (b) Inner and outer surfaces with split regions.

The centerlines were calculated based on the outer surface using the 'vmtkcenterlines' function in VMTK [152], Figure 23(a). The inlet was set to be the ICA opening, and the outlets were set to be openings of MCA, ACA and PCOM. Then both the inner and outer surfaces were split into different branches based on the previously calculated centerlines using 'vmtkbranchextractor' and 'vmtkbranchclipper' functions in VMTK [153]. Nodes in different branches were labeled by corresponding group ID in the output surface file, Figure 23(b).

4.2.5.2 Bifurcation Regions

A custom Matlab code (R2017a, MathWorks Inc., Natick, MA) was then designed to take the surfaces with separated regions defined by VMTK, identify surfaces at vessel bifurcations, and use these surfaces to localize calcification within each region. The bifurcation regions were identified on the inner and outer surfaces separately following the same steps. The centerpoint of a bifurcation region, which was defined as the middle point of the curve between two intersecting regions, was located first, Figure 24(a). Points on the intersecting curve and the midpoint between two end points of the curve can form an angle θ. The centerpoint of the bifurcation region, which was the same centerpoint on the curve, was found at the point on the curve which has a θ that is closest to $\pi/2$, Figure 24(a).

After the centerpoint of the bifurcation was identified, a circular bifurcation region was propagated from that point with chosen diameter. In particular, diameter of each bifurcation region was chosen to be the diameter of the artery with the smallest size that formed the bifurcation, Figure 24(b, c). For example, the diameter of the PCOM bifurcation region for the inner surface was the inner diameter of the PCOM, which is 1.1 mm [154]. The diameter of the PCOM

bifurcation region on the outer surface was the outer diameter of the PCOM, which is 1.5 mm [155]. The diameters of the ICA bifurcation region on the inner and outer surfaces were the inner and outer diameters of the ACA, which are 1.8 mm and 2.3 mm, respectively [154,155]. In Matlab, using the alphaShape function, alpha shape volumes were constructed using the vertex of the inner and outer artery surfaces. These volumes and the inShape Matlab function were then used to determine the region where the vertices of the calcification were residing. These labels and surfaces were then used to extract stl files of the calcification in each region. The stl files of the bifurcation, including inner surface, outer surface and calcification, were exported, Figure 24(d).

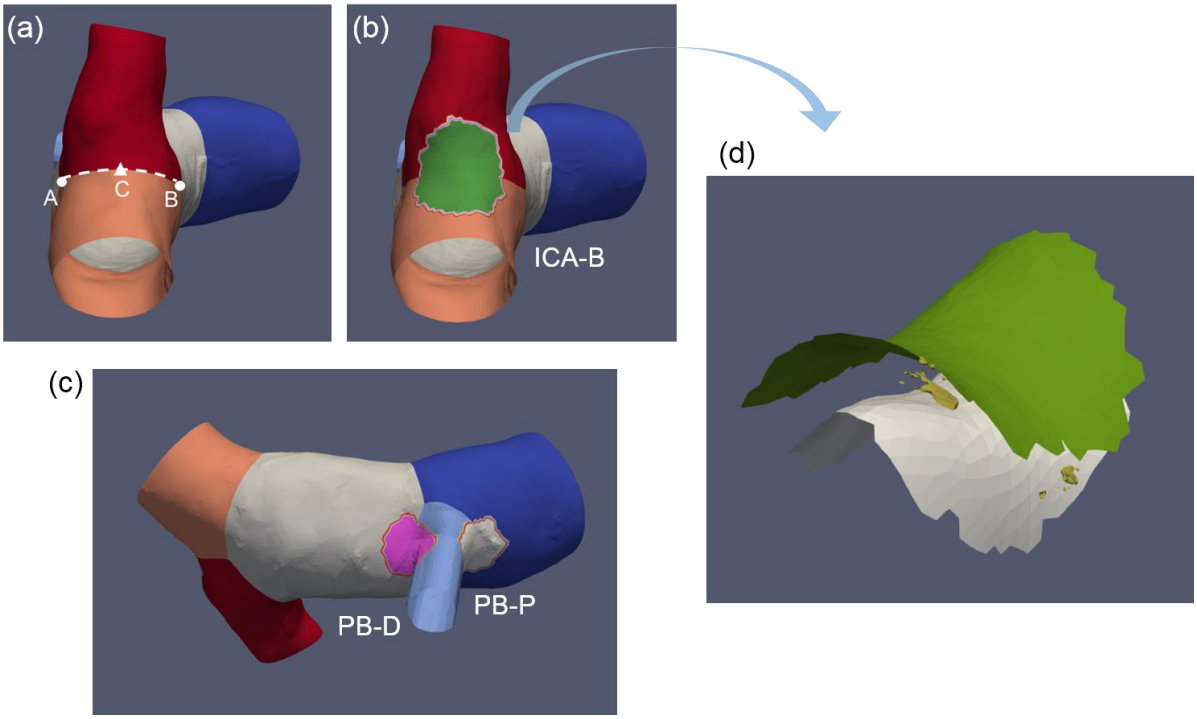

Figure 24 Identifying and extracting bifurcation regions. (a) The centerpoint (C) of the bifurcation region was located at the middle point of curve AB. (b) ICA bifurcation (ICA-B) was formed by propagating an area outward from the centerpoint to a radius equal to that of the ACA. (c) PCOM bifurcations (PB-D, PB-P) were formed by propagating an area from the centerpoints to a radius equal to that of the PCOM. (d) Illustration of extracted inner surface, outer surface and calcification at bifurcation region.

4.2.6 Calcification Location and Volume Fraction Analysis for Separate Regions

4.2.6.1 Calcification Location Analysis

To assign each calcification particle to either the inner, middle or the outer third of the wall thickness, a high fidelity protocol was utilized [156] that identifies two intramural surfaces that separate the wall into three regions. Briefly, the normal vectors for all points on the outer surface were determined and used to locate the counterparts on the inner surface. Then the distance vectors between the inner and outer surfaces were defined based on the points on the outer surface and counterparts on inner surface. The distance vectors were divided into three equal parts with two markers. Two triangulated surfaces were then reconstructed using the markers labelled on the distance vectors. Once these two surfaces were identified, the calcification particles could be assigned to the inner, middle and outer third of the wall.

4.2.6.2 Calcification Volume Fraction in Separate Regions

The data for the calcification in the sample was obtained from micro-CT scans in the form of point cloud entities. The volume of calcification in each third of the arterial wall was determined using the methods presented in [156]. Briefly, using the machine learning classification algorithm, DBScan, each of the calcified particles/entities in the micro-CT's dataset was identified. Then, the volume of each of these particles was determined using the MATLAB built-in function, AlphaShape. Finally, the overall volume of the calcifications within the region of interested was determined by summing the volumes of all particles in that region.

4.2.7 Statistical Analysis

Statistical analysis was conducted using IBM SPSS Statistics (version 25, IBM Corp, Armonk, N.Y., USA). The assumptions of normality and homogeneity of variance were tested first using Shapiro-Wilk test and Levene's test, respectively. Mann-Whitney U Test was used to test the statistical difference between arteries and aneurysms for continuous variable. Chi-squared test or Fisher's Exact test were used to determine the statistical difference in the distribution of categorical variable between arteries and aneurysms. One-way ANOVA followed by the Games-Howell post hoc was applied to compare the means among groups on the same continuous variable if the assumptions of parametric tests were attained. Otherwise, Kruskal-Wallis test followed by Dunn's test with a Bonferroni correction was applied. A two-tailed *p*-value less than 0.05 was considered to be statistically significant.

4.3 Results

4.3.1 Calcification is Present in All Cerebral Artery Samples

The average age of all patients is 82 ± 7.6 years old. The patient characteristics were listed in Table 7. Calcification was present in all cerebral artery samples (20/20) with a range of volume fraction between 0.013% and 12.2% with an average of 1.56 ± 3.04%, Figure 25(a). Fourteen out of 20 cases had a volume fraction of calcification less than 1%. There was no correlation between calcification volume fraction and patient age. The average volume fractions were not significantly different between sexes and for patients with and without a given medical condition.

Table 7 Summary of patient clinical data

Case ID	Age	Sex	Hyper-tension	Hyper-lipidemia	Diabetes	Smoking	Primary Neurodegenerative Diagnosis
CW18-008	100	F	yes	no	no	no	AD neuropathologic change
CW18-009	76	M	yes	no	no	yes	Progressive Supranuclear Palsy
CW18-011	70	F	no	yes	no	yes	AD neuropathologic change
CW18-012	73	F	no	no	no	no	AD neuropathologic change
CW18-013	94	F	yes	yes	no	no	Vascular dementia
CW18-015	81	F	yes	yes	no	yes	AD neuropathologic change
CW18-017	80	M	no	yes	yes	N/A	AD neuropathologic change
CW18-021	82	F	yes	yes	no	yes	AD neuropathologic change
CW18-022	71	M	N/A	N/A	yes	N/A	Progressive Supranuclear Palsy
CW18-023	87	M	yes	yes	no	yes	AD neuropathologic change
CW18-024	82	F	yes	no	no	no	AD neuropathologic change
CW18-025	76	M	yes	no	no	no	DLB, neocortical
CW18-028	88	F	yes	yes	no	yes	AD neuropathologic change
CW18-029	86	M	yes	yes	no	no	AD neuropathologic change
CW18-030	84	F	no	yes	no	no	AD neuropathologic change
CW19-002	76	F	no	no	no	no	AD neuropathologic change
CW19-003	88	F	yes	yes	yes	no	AD neuropathologic change
CW19-005	88	F	no	yes	no	yes	AD neuropathologic change
CW20-002	78	F	N/A	N/A	N/A	N/A	AD neuropathologic change
CW20-004	79	M	yes	no	no	no	AD neuropathologic change

*AD: Alzheimer disease

*DLB: dementia with Lewy bodies

For the aneurysms, 76% cases had a volume fraction of calcification that was less than 0.1% [25,90], Figure 25(a). The volume fraction of calcification previously reported for cerebral aneurysms (0.69 ± 2.16%) was significantly lower than for the cerebral arteries studied here (p < 0.001), Figure 25(b).

Due to the complexity of the arterial geometry, the inner and outer surfaces could only be successfully separated for 10 samples and therefore the analysis of the distribution of calcification across the wall was based on these 10 cases, Table 8. The middle third and outer third of arteries had the highest and lowest average volume fraction of calcification, respectively, Figure 26(a), although there was no significant difference among inner, middle and outer thirds (p = 0.722). In contrast, the outer third of the cerebral aneurysm wall had significantly higher calcification than the inner third, Figure 26(b).

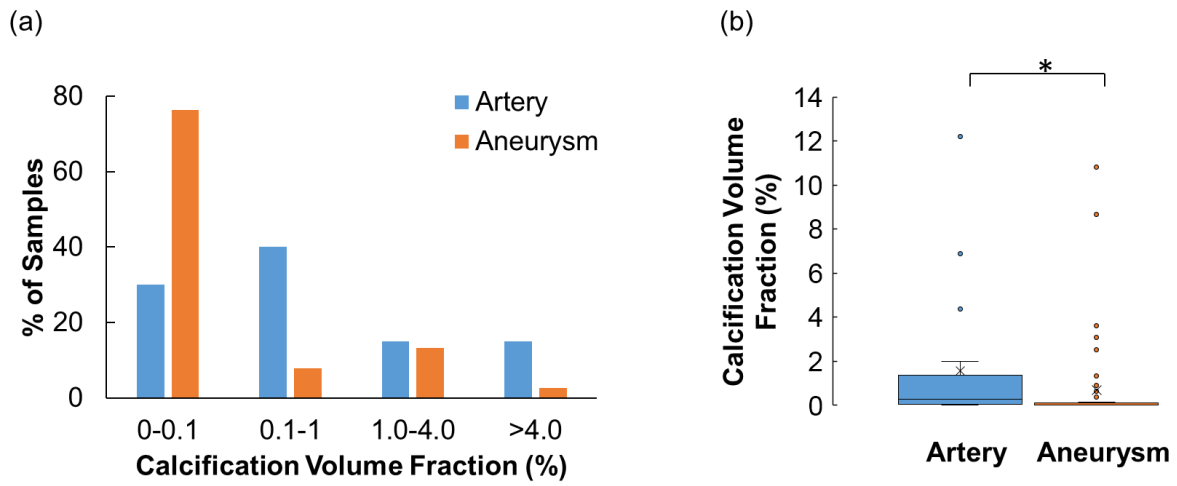

Figure 25 Calcification volume fraction in cerebral arteries (blue) and cerebral aneurysms (orange). (a) Distribution at different ranges. (b) Calcification volume fraction in cerebral arteries is higher than cerebral aneurysms (p < 0.001). Data of cerebral aneurysms was from [25].

Table 8 Calcification volume fraction, wall type and largest particle size in cerebral arteries

Case ID	Calcification Volume Fraction (%)	Wall Type	Largest Particle size	Location Analysis
CW18-008	1.210	III	Macro	No
CW18-009	0.229	II	Macro	Yes
CW18-011	0.527	III	Meso	Yes
CW18-012	1.990	III	Macro	Yes
CW18-013	0.273	III	Macro	No
CW18-015	1.430	III	Macro	No
CW18-017	0.061	III	Meso	Yes
CW18-021	0.015	III	Micro	No
CW18-022	0.124	III	Macro	No
CW18-023	0.013	I	Micro	No
CW18-024	0.036	II	Meso	No
CW18-025	4.380	III	Macro	Yes
CW18-028	12.200	III	Macro	No
CW18-029	0.944	III	Macro	No
CW18-030	0.245	III	Macro	Yes
CW19-002	0.133	I	Micro	Yes
CW19-003	0.036	III	Meso	Yes
CW19-005	6.890	III	Macro	No
CW20-002	0.334	III	Macro	Yes
CW20-004	0.034	II	Meso	Yes

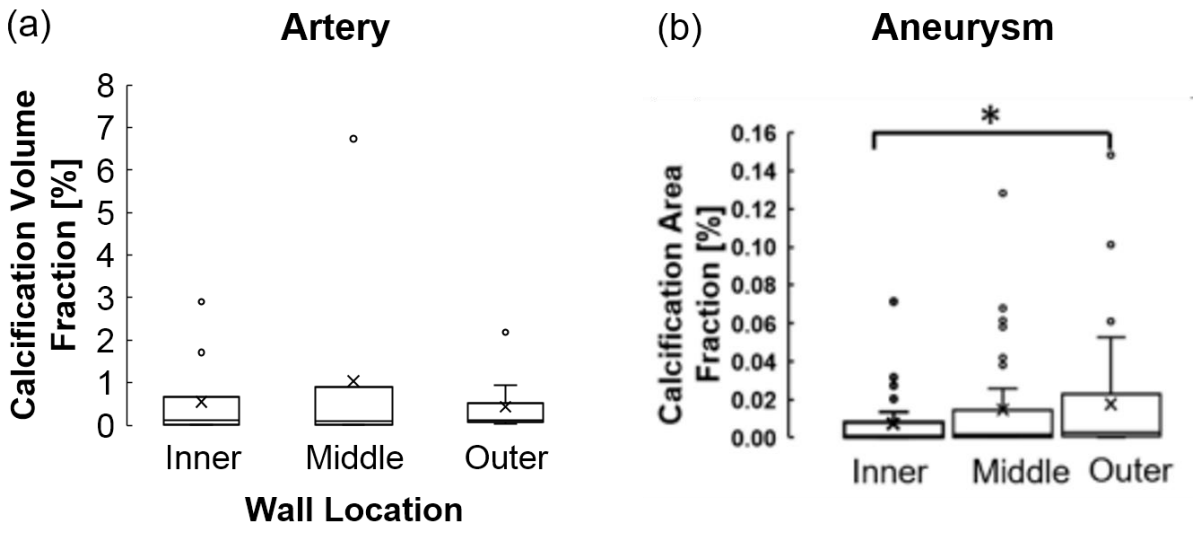

Figure 26 Calcification distribution in different layers of (a) cerebral arteries (n=10) and (b) cerebral aneurysms (n=51). (b) was reproduced from [25] with permission.

4.3.2 Most Calcification Particles Are Micro-Calcifications

For all particles, the ratio of the minor to major axis of the bounding ellipsoid is 0.5 ± 0.38. 91% of calcification particles had a major diameter that is less than 30 μm, Figure 27. The largest particle had a major diameter of 7.4 mm. Aneurysms were also reported to have a similar particle size distribution, Figure 27.

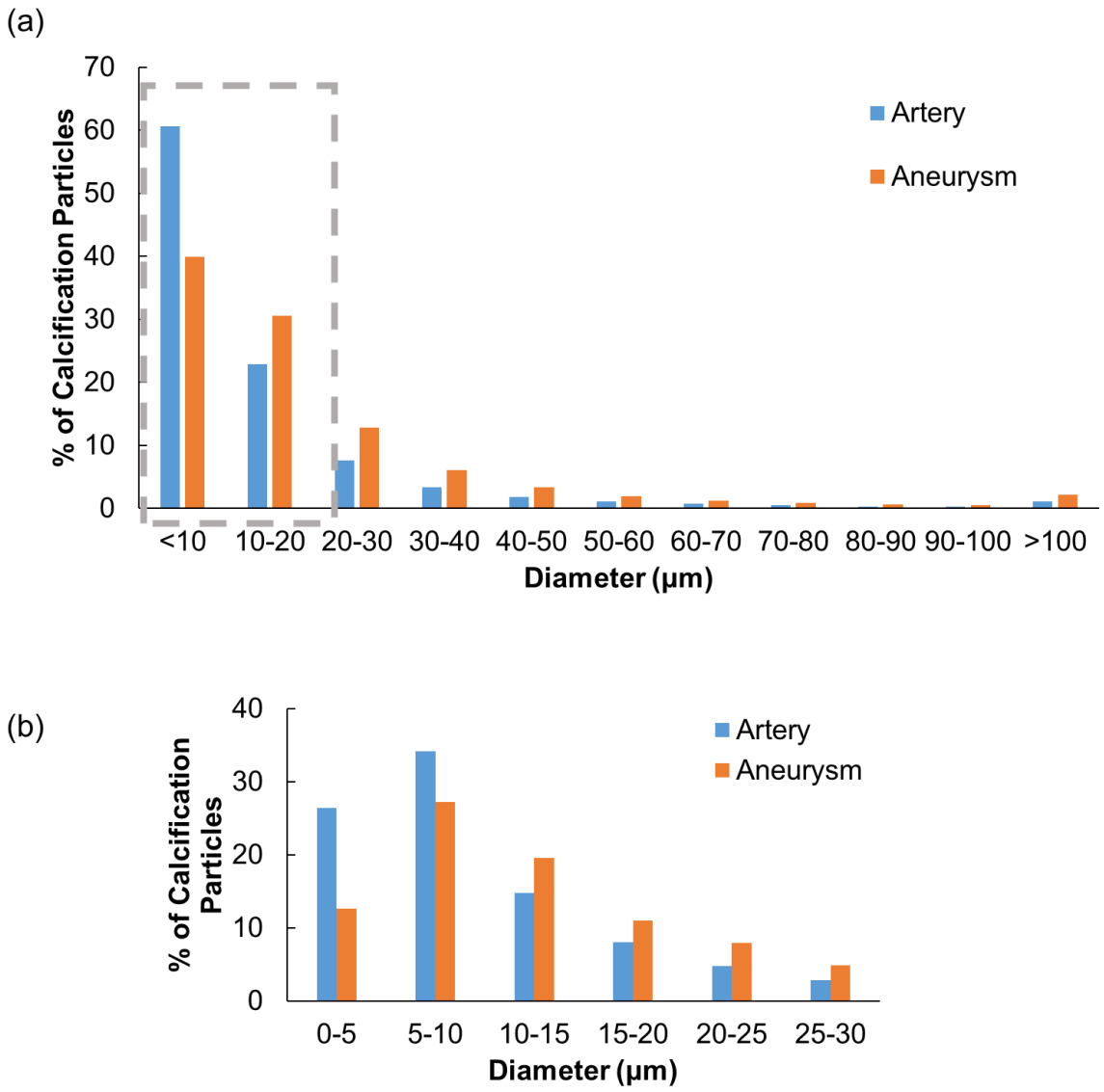

Figure 27 Most calcification particles are less than 30 μm, for both cerebral arteries and cerebral aneurysms. (a) Distribution of all sizes in cerebral artery and aneurysm. (b) Zoomed in distribution of calcifications less than or equal to 30 μm in artery and aneurysm. Data of cerebral aneurysms was from [25].

Macro-calcifications were present in 12 out 20 samples, Figure 28. For the remaining 8 cases, meso-calcifications were present in 5 of them. There were 3 cases that only had micro-calcifications. For the 12 cases that had macro-calcifications, meso-calcifications were also found. All samples (20/20) had micro-calcifications distributed in the wall. The proportion of arteries that had macro-calcifications was significantly higher than for aneurysms ($p < 0.001$), Figure 28.

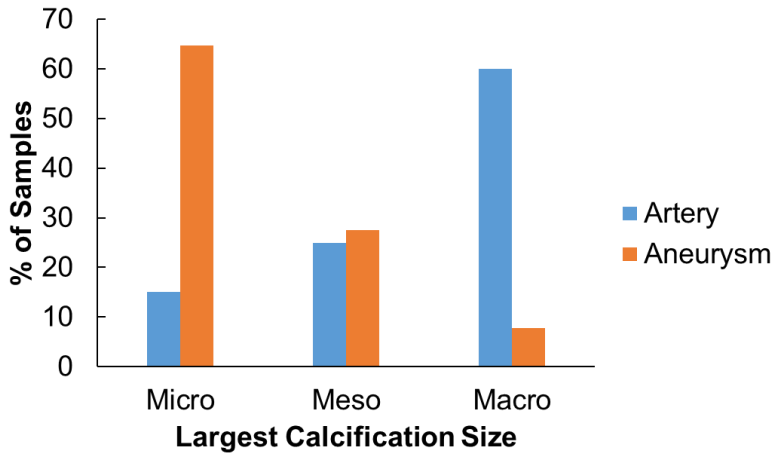

Figure 28 Macro-calcification has higher prevalence in cerebral arteries (blue) than cerebral aneurysms (orange). The proportions of calcification size in arteries and aneurysms are significantly different ($p < 0.001$). Data of cerebral aneurysms was from [25].

4.3.3 Most Calcification Found in Atherosclerotic Form

Representative CT slices of different wall types were showed in Figure 29. Only 2 samples were Type I wall, which indicated that there were no lipid pools found in the entire wall, Figure

30. These two samples only had micro-calcifications, Figure 29, located in the inner third of the wall. Three samples were found to have Type II walls for which lipid pools were present in the wall but never co-localized with calcifications. Only one case had macro-calcification located in the middle third of the wall. The other two cases of Type II walls had meso-calcifications located in the outer third of the wall. There were 15 samples that had Type III walls (lipid pools had co-localized calcification). Macro-calcifications were present in most cases of Type III wall (11/15). All samples with Type III walls also had calcification particles that were not associated with lipid pools. Whereas, atherosclerotic (Type III) walls were found in 15/20 cerebral artery samples, they were only found in a 23.5% of aneurysm samples, Figure 30. The proportions of wall types in aneurysms and arteries are significantly different ($p < 0.001$).

Arteries with atherosclerotic calcifications (Type III, n=15) had significantly higher calcification volume fraction than arteries with only non-atherosclerotic calcifications (Type I and Type II, n=5) with $p = 0.015$, Figure 31(a). Similarly, cerebral aneurysms with Type III walls had significantly higher calcification volume fraction than samples only with non-atherosclerotic calcifications (Type I and Type II), $p = 0.009$, Figure 31(b).

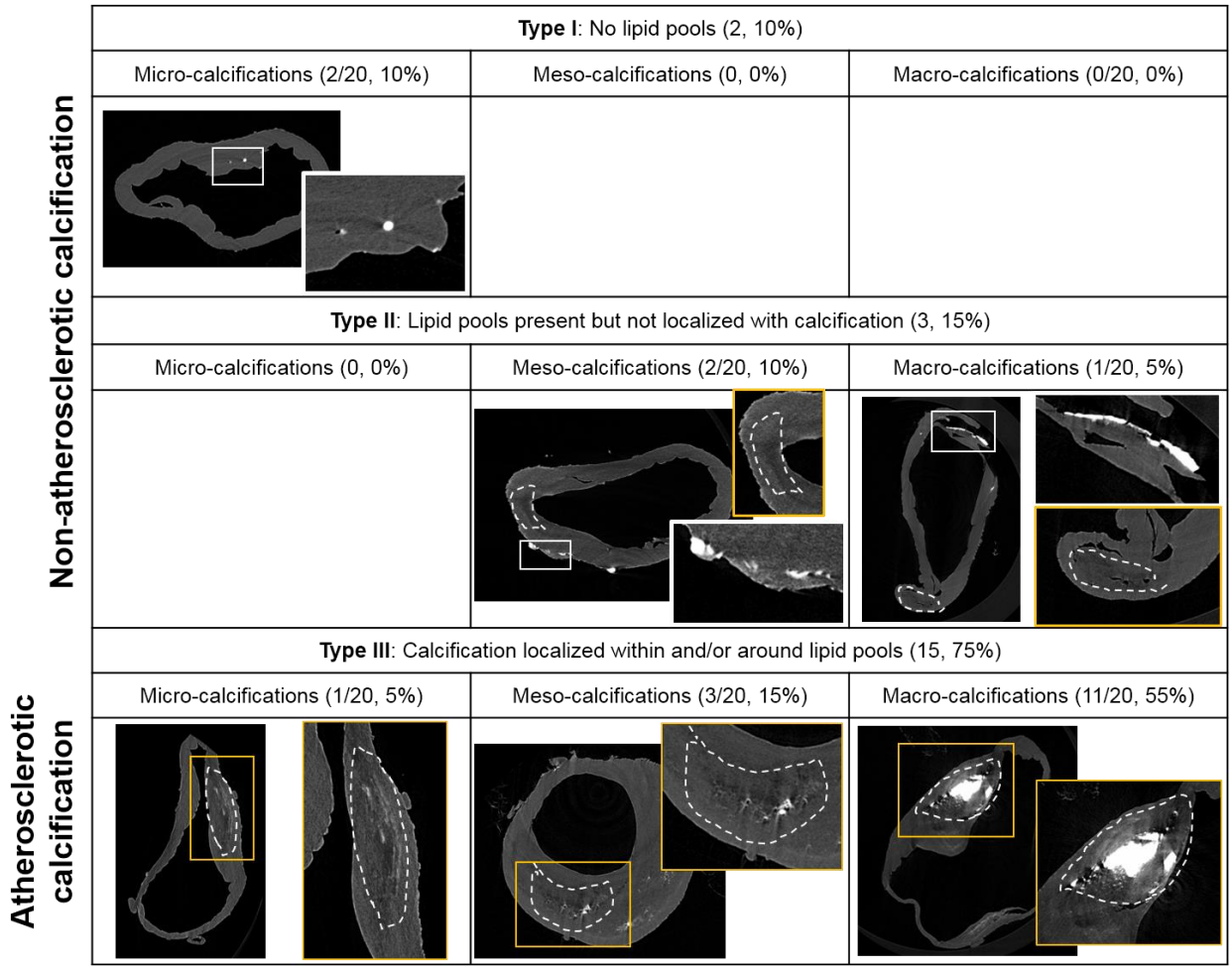

Figure 29 Representative CT slices of three different wall types which are subcategorized based on largest particle found in the sample. The white and yellow rectangles show zoomed in calcification and lipid pools, respectively. Lipid pools are indicated by white dotted lines.

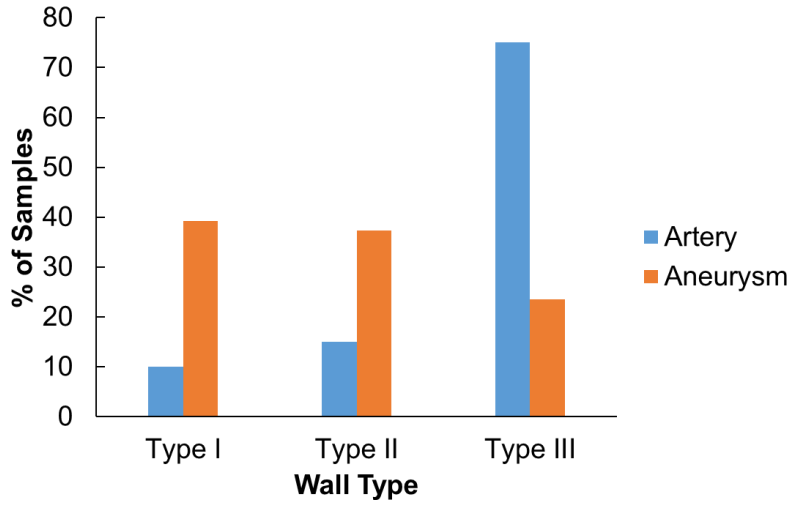

Figure 30 Majority of cerebral arteries have atherosclerotic calcifications (Type III wall). The proportions of wall types of cerebral arteries (blue) and cerebral aneurysms (orange) are significantly different ($p < 0.001$). Data of cerebral aneurysms was from [25].

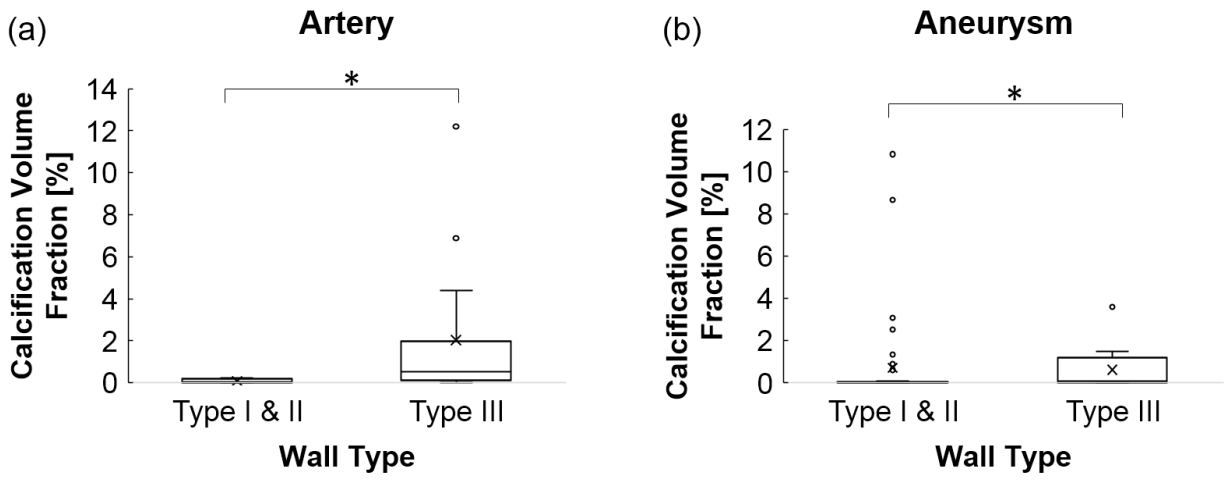

Figure 31 Type III walls had significantly higher calcification volume fraction than Type I&II for both (a) cerebral arteries ($p = 0.015$) and (b) cerebral aneurysms ($p = 0.009$). Data of (b) was obtained from experiments performed by Dr. Gade with permission.

4.3.4 Calcification at Bifurcations

Results in this section were based on the 10 cases that the inner and outer surfaces were separated successfully. The non-bifurcation region and ICA bifurcation had the highest and lowest average volume fraction of calcification, respectively, Figure 32. The calcification volume fraction was significantly different between the distal PCOM bifurcation and non-bifurcation region (p = 0.015). The proximal (PB-P) and distal (PB-D) PCOM bifurcations had close average volume fraction of calcification (0.52% vs 0.51%). There was no statistical difference among three bifurcations of arteries and cerebral aneurysms.

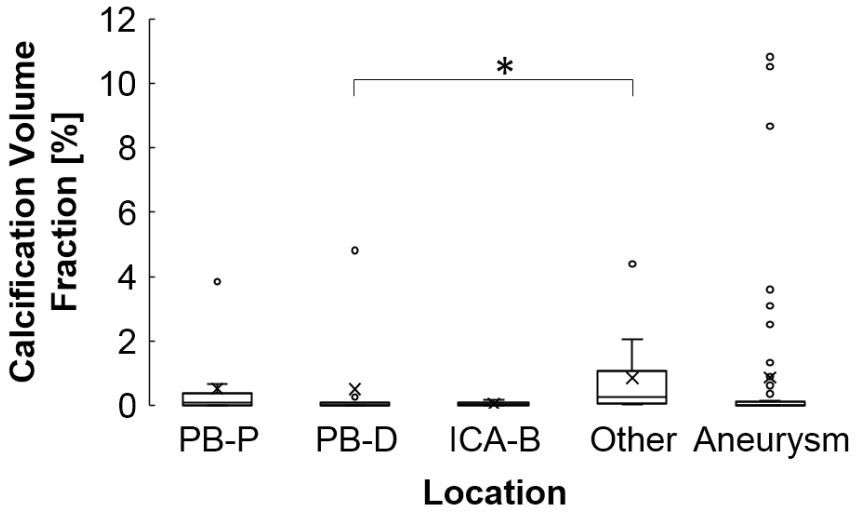

Figure 32 Volume fraction of calcification at the bifurcations of cerebral arteries (n=10). The volume fraction of calcification at non-bifurcation regions was significantly higher than for the distal PCOM bifurcations (p = 0.015). The difference in calcification volume fraction was not signficant between cerebral aneurysms and any region of the cerebral artery.

The distribution of calcification in the inner, middle and outer thirds showed different patterns for different regions, Figure 33. At the distal PCOM bifurcation, more calcification was located in the outer third. At the proximal PCOM bifurcation and ICA bifurcation, the distribution was relatively uniform across the wall. For the non-bifurcation region, more calcification was found in the middle third.

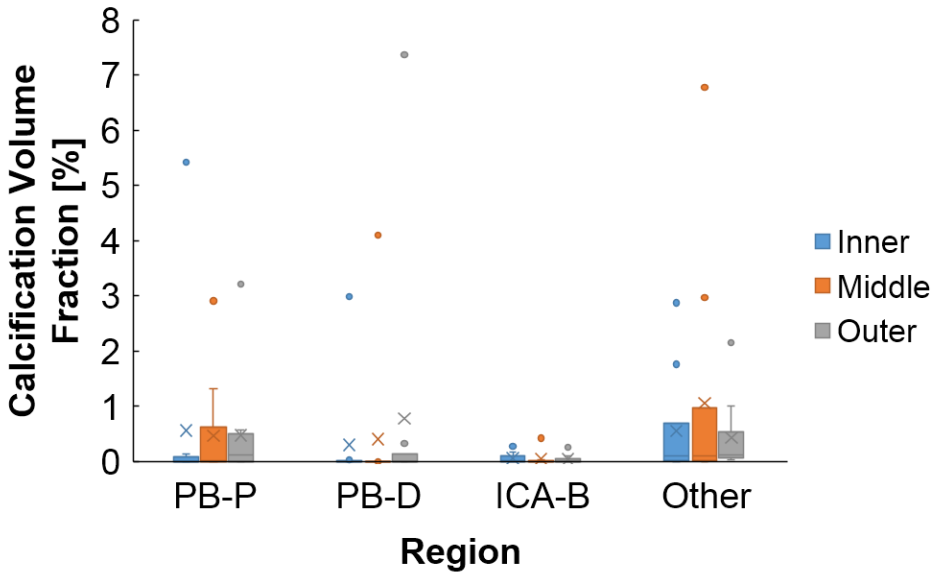

Figure 33 The distribution of calcifications in the inner, middle and outer thirds for bifurcations and remaining region

4.4 Discussion

In this work, calcifications in the ICA and associated bifurcations, PB-P, PB-D and ICA-B, were analyzed from micro to macro scales using high resolution micro-CT. Calcifications were found in all samples (n = 20) with a volume fraction between 0.013% and 12.2%. The results found were compared to data on intracranial aneurysms from prior work in our group [25,90].

The cerebral arteries were found to be significantly more calcified than cerebral aneurysms. One possible reason is that the age of patients in this study was substantially higher than patients in the aneurysm study. The average ages of patients in the current study and the aneurysm study are 82 years old and 57.5 years old, respectively. Aging was reported to be an important factor for vascular calcification, and the prevalence and calcification amount increase with increasing age in extracerebral arteries [157–159]. Most arteries (15/20) in this study had a Type III wall with atherosclerotic calcifications associated with lipid pools. This finding is different from calcifications in aneurysms. In the aneurysms, non-atherosclerotic calcification (no associated lipid pool) was more prevalent than for arteries. Moreover, calcifications in the middle third of cerebral arteries had the highest volume fraction. In contrast, the outer third in aneurysms was the most calcified.

The dominant calcification particles had a size that was less than 30 μm, which is similar to the aneurysm cases. Macro-calcifications were found in 12 out of 20 arteries. In contrast, only 7.8% of aneurysms had macro-calcifications. Figure 11 showed the relationship between particle counts and volume fraction of calcification of all samples in a log-log scale. The largest particle size found in each sample by a different data symbol. The accumulation of calcifications was related to both particle numbers and the largest particle size in that sample, Figure 34. At the early stage (with low calcification volume fraction), the volume fraction of calcification increased due

to both increasing number of particles and particle size. After the calcification volume fraction reached a certain level, the elevation of calcification was largely due to the increasing particle size, Figure 34(b). It suggests that smaller particles aggregated to form larger entities. Namely, it is possible that the clusters of micro-calcifications found in arteries and aneurysms preceded the formation of large calcifications [146].

The non-bifurcation region had higher volume fraction of calcification compared to the three bifurcations, although the statistical difference was only found between non-bifurcation region and distal PCOM bifurcation. Since most aneurysms originate at bifurcations, calcification volume fraction between cerebral aneurysms and different bifurcations were compared. There was no significant difference found in any pair. Even though there was no difference of the average calcification volume fraction between proximal and distal PCOM bifurcations, the distribution of calcification in the wall was different substantially. For the proximal PCOM bifurcation (PB-P), the middle third of the wall had the most calcification. Notably, calcification was highest in the outer third of the distal bifurcation of the PCOM artery (PB-D), similar to what is reported for cerebral aneurysms, Figure 26(b). It should be noted that the distal PCOM bifurcation accounts for most aneurysms among these three bifurcations [160]. These findings suggest that the calcification may be different in regions more prone to aneurysm formation.

The wall types were also categorized based on whether there was any atherosclerotic calcification in the wall. While this is useful for understanding walls without atherosclerotic calcification, it does not exclude the possibility that atherosclerotic walls also had non-atherosclerotic calcification. In the future, new techniques could be developed to analyze the raw CT scans to segment out regions of lipid pools so that each calcification particle can be definitively categorized as atherosclerotic or non-atherosclerotic.

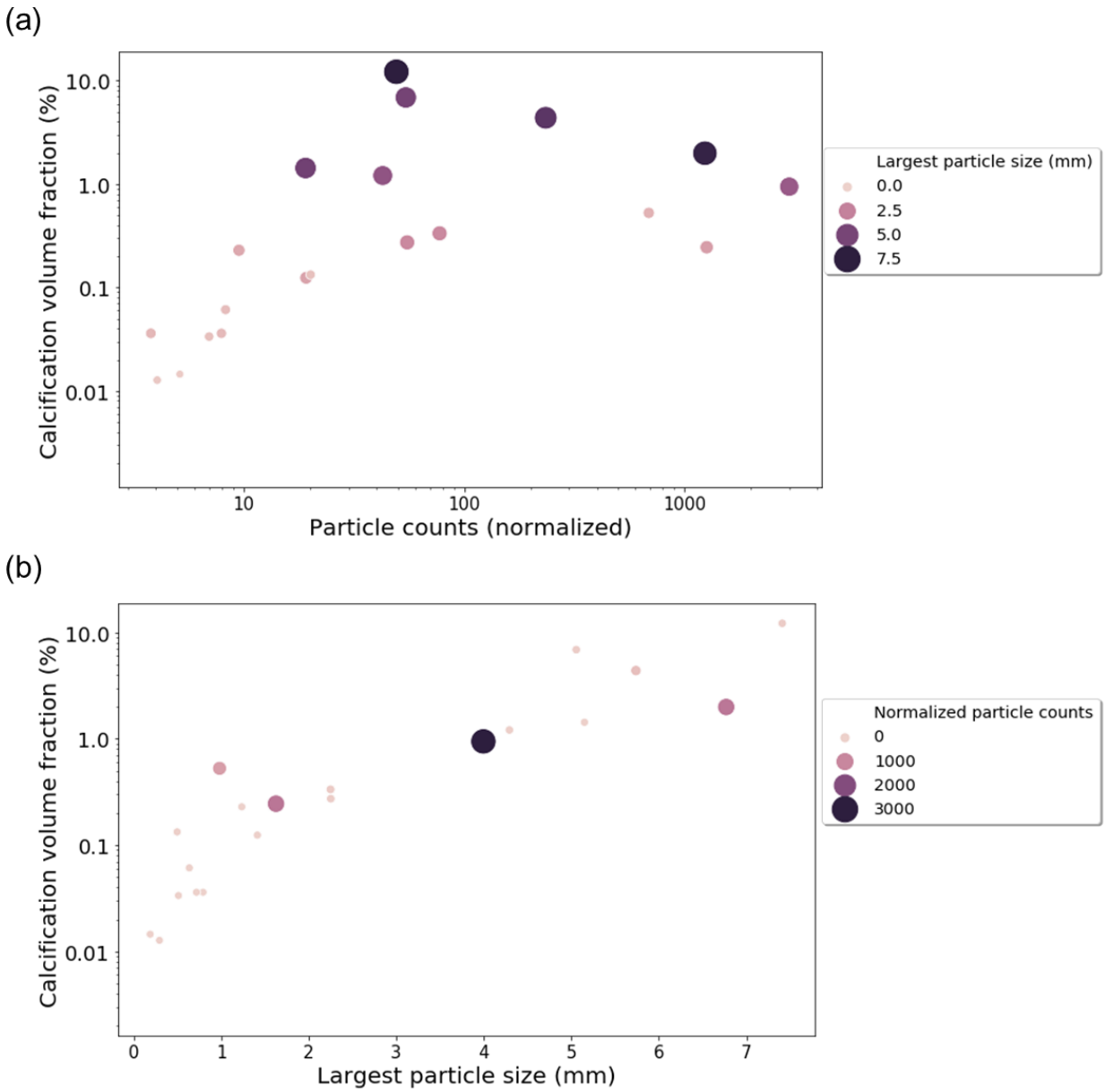

Figure 34 Relation among particle counts, largest particle size and volume fraction of calcifications of cerebral arteries. (a) Calcification volume fraction increased as particle counts increased at low volume fraction. (b) Calcification volume fraction increased as the largest particle size increased.

As noted in [25], the spatial distribution of micro-calcifications will be important for the mechanical properties of the wall. For example, a cluster of micro-calcifications which reside locally in a certain region will be expected to have a different effect on wall strength than those distributed sparsely across the wall. Moreover, the near calcification region is expected to have a great impact on the influence of calcification on the stress distributions in the wall [161]. Moreover, there is a pressing need to understand the interaction between the lipid pools, calcifications and collagen fibers during load bearing. In a preliminary study, multiphoton microscopy was used to explore the relation between calcification and collagen fibers in an aneurysm sample under uniaxial stretch, Appendix C. In the future, the relationship between lipid pools, calcifications and collagen fibers should be studied both computationally and experimentally, to determine their coupled influence on wall strength.

4.5 Acknowledgment

I am grateful to the collaborative efforts for this chapter. Dr. Robertson supervised and guided the entire research progress. Patrick Tatlonghari performed 18 out of 20 cases of scanning and reconstruction of the CT. Ronald Fortunato identified the bifurcation regions and separated the surfaces files into different groups, Section 4.2.5.2. Mehdi Ramezanpour calculated the calcification distribution across the wall to obtain the volume of calcification in each separated wall region, Section 4.2.6. Dr. Maiti also provided guidance and insights on the analysis of this chapter. Dr. Tobe transported and fixed all the circles of Willis.

Appendix A Constitutive Modeling of Rabbit Aneurysm

Appendix A.1 Fiber Dispersion Model

The collagen component is treated as a collection of extensible fibers with a distribution of orientations. In general, a single collagen fiber will have a wavy conformation in reference configuration κ_0, Figure 10(b). Using local Cartesian coordinates with unit base vectors ($\boldsymbol{e_1}$, $\boldsymbol{e_2}$) (Figure 10(a)), a direction is associated with undulated fiber $\boldsymbol{m_0}$ in reference configuration κ_0 where can be decomposed to

$$\boldsymbol{m_0} = cos\theta \boldsymbol{e_1} + sin\theta \boldsymbol{e_2}. \qquad \textbf{A - 1}$$

The undulated fiber is assumed to become load bearing when the material element in direction $\boldsymbol{m_0}$ has undergone a stretch of λ_a, Figure 10(b). This activation stretch is an additional material property determined from average tortuosity of fibers. Then the fiber commences stretching when $\lambda_f = \lambda_a$. The true stretch of the fiber λ_t is then

$$\lambda_t = \lambda_f / \lambda_a \qquad \textbf{A - 2}$$

where λ_f can be obtained from

$$\lambda_f{}^2 = \boldsymbol{C}:\boldsymbol{m_0}\otimes\boldsymbol{m_0} \qquad \textbf{A - 3}$$

The distribution of fibers was represented by probability density function (PDF) of fibers at arbitrary orientation $\mathbf{m_0}$ in the reference configuration. Motivated by the MPM data, only collagen fibers in 2D plane were considered. The PDF was represented by a bimodal von Mises distribution [162]

$$\rho(\theta) = \frac{1}{2I_0(b_1)} e^{b_1 cos2(\theta - a_1)} + \frac{1}{2I_0(b_2)} e^{b_2 \cos 2(\theta - a_2)} \quad \theta \in [0, \pi) \qquad \textbf{A - 4}$$

where a_1 and a_2 are symmetrical angles of two peaks, b_1 and b_2 are concentration parameters. $I_0(b)$ is the Bessel function of order zero defined by

$$I_0(b) = \frac{1}{\pi}\int_0^{\pi} e^{bcos\theta}\, d\theta \qquad \textbf{A - 5}$$

and the distribution is normalized such that [163],

$$1 = \frac{1}{\pi}\int_0^{\pi} \rho_i(\theta)\, d\theta \qquad \textbf{A - 6}$$

The four parameters (a_1, a_2, b_1, b_2) of Equation (10) of each case were determined using maximum likelihood estimation by function MLE in Matlab (MathWorks Inc. Natick, MA) [109] based on collagen fiber orientations measured from the MPM stacks using ctFIRE. The parameters of ctFIRE were listed in Table 9, with more details on the functions found at https://loci.wisc.edu/software/ctfire.

Table 9 Input parameters of ctFIRE

Parameter	Default value
thresh_im2	5
s_xlinkbox	8
thresh_ext	70
thresh_dang_L	15
thresh_short_L	15
s_fiberdir	4
thresh_linkd	15
thresh_linka	-150
thresh_flen	15
Percentile of the remaining curvelet coeffs	0.2
Number of selected scales	3

The strain energy function of collagen in each layer is then constructed by integrating response of fibers over all directions [52,108]. The strain energy function of collagen in each layer

$$W_{fi} = \frac{1}{\pi}\int_0^{\pi} \rho_i(\theta)\, w_{fi} d\theta \qquad \textbf{A - 7}$$

where w_{fi} is the strain energy of fibers in layer i, and defined as

$$w_{fi} = \frac{\beta_i}{2}({\lambda_t}^2 - 1)^2 \cdot H(\lambda_t - 1) \qquad \textbf{A - 8}$$

where the Heaviside function is used to switch the fiber contribution off when under compression

$$H(\lambda_t - 1) = \begin{cases} 0 & if\ \lambda_t \leq 1 \\ 1 & if\ \lambda_t > 1 \end{cases} \qquad \textbf{A - 9}$$

Appendix A.2 Determination of Material Parameters from Uniaxial Tension Experiments

As each layer only occupies a fraction of the cross section, Figure 35,

$$\boldsymbol{\sigma} = -p\boldsymbol{I} + \sum_{i=1}^{N} \gamma_i(\mu_i \boldsymbol{\sigma_{fi}} + (1 - \mu_i)\boldsymbol{\sigma_{gi}}) \qquad \textbf{A - 10}$$

where p is the Lagrange multiplier arising from the constraint of incompressibility, γ_i is the thickness fraction of layer i and μ_i is the areal fraction of collagen fibers in cross section of layer i.

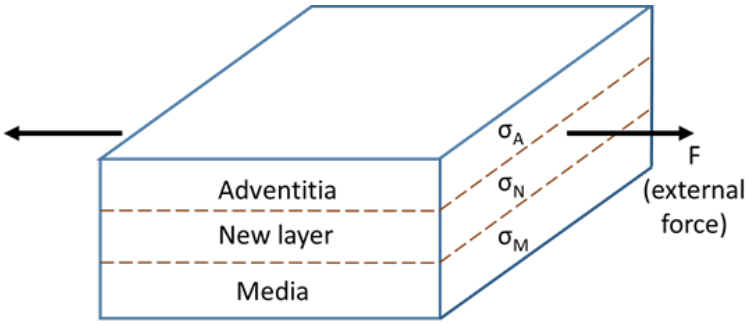

Figure 35 Schematic of stress distribution on different layers

Material constants in the structurally motivated constitutive model will be determined from multiphoton imaging and uniaxial mechanical testing. Assuming the tissue is incompressible, necessarily the deformation is isochoric with principal stretch values satisfying $\lambda_1\lambda_2\lambda_3 = 1$. The corresponding deformation gradient tensor and Cauchy Green tensors are

$$[\boldsymbol{F}] = diag\left[\lambda_1, \lambda_2, \frac{1}{\lambda_1\lambda_2}\right], \quad [\boldsymbol{C}] = [\boldsymbol{b}] = diag\left[{\lambda_1}^2, {\lambda_2}^2, \frac{1}{{\lambda_1}^2{\lambda_2}^2}\right] \qquad \textbf{A - 11}$$

where λ_i is the principal stretch in direction $\boldsymbol{e_i}$. Coordinate axis are chosen such that the loading direction is $\boldsymbol{e_2}$ and $\boldsymbol{e_3}$ is orthogonal to the sample. Then the principal components of the Cauchy stress can be written as

$$\sigma_1 = -p + {\lambda_1}^2 \sum_{i=1}^{N} \gamma_i (1-\mu_i)\alpha_i + \frac{2}{\pi} \sum_{i=1}^{N} \gamma_i \mu_i {\lambda_1}^2 \left\{ \int_0^{\pi} \rho_i \frac{\partial w_{fi}}{\partial {\lambda_f}^2} cos^2\theta \, d\theta \right\} \qquad \textbf{A - 12}$$

$$\sigma_2 = -p + {\lambda_2}^2 \sum_{i=1}^{N} \gamma_i (1-\mu_i)\alpha_i + \frac{2}{\pi} \sum_{i=1}^{N} \gamma_i \mu_i {\lambda_2}^2 \left\{ \int_0^{\pi} \rho_i \frac{\partial w_{fi}}{\partial {\lambda_f}^2} sin^2\theta \, d\theta \right\} \qquad \textbf{A - 13}$$

$$\sigma_3 = -p + \frac{1}{{\lambda_1}^2 {\lambda_2}^2} \sum_{i=1}^{N} \gamma_i (1-\mu_i)\alpha_i \qquad \textbf{A - 14}$$

By setting $\sigma_3 = 0$, an expression for the Lagrange multiplier p can be obtained. An implicit relation between λ_1 and λ_2 can then be obtained by setting Equation A-13 to be zero. Using Equation A-12 along with this implicit relation and the experimental data (relation between σ_1 and λ_1), the parameters α_i and β_i can be obtained from minimizing the least-squares objective function. The interior-point optimization algorithm of FMINCON function in Matlab (R2017a, MathWorks Inc., Natick, MA) was then used.

Appendix A.3 Acquisition of Other Parameters

Appendix A.3.1 Thickness Fraction of Each Layer - γ

Thickness fraction of each layer was measured from MPM images. For each MPM stack, the planar images were taken by a step size of 2 μm. The MPM images of different layers showed

distinct structures and were easy to determine the boundaries. Then the thickness of each layer was calculated as the slice numbers of MPM images multiplying imaging step size (2 μm). Figure 36 showed the cross section of MPM images of one aneurysm case.

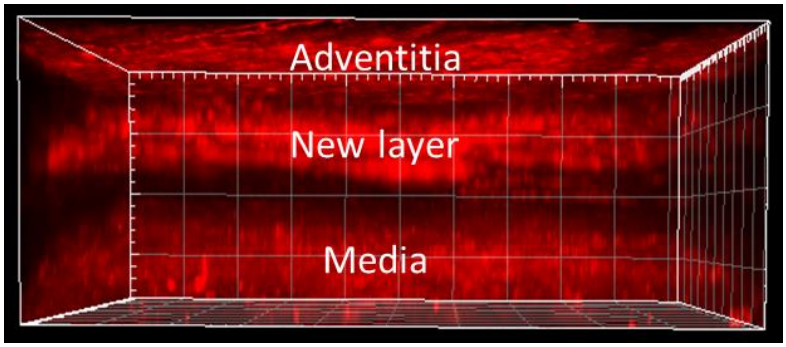

Figure 36 Cross section of MPM stack shows three different layers

Appendix A.3.2 Areal Fraction of Collagen Fibers - μ

Each later is considered to be composed of three different constituents, collagen fibers, elastin and ground matrix. Here the elastin was assumed to be isotropic and was combined with ground matrix. The strain energy function of this combined part is Neo-Hookean. The collagen fibers have different densities and distributions in each layer. To determine the stress contribution of collagen fibers in each layer, the cross sectional MPM images were analysis using ImageJ by thresholding. The areal fractions of collagen fibers at three different locations were measured and averaged.

Appendix A.3.3 Activation Stretch of Fiber

The activation stretch of fibers was assumed to be the average tortuosity of fibers in each layer. The tortuosity of fibers was obtained from manual tracing in Imaris.

Appendix A.3.4 Probability Density Function of Fiber Angle

The PDF of fiber angle was assumed to be Bimodal von Mises distribution. The angle of each traced fiber was obtained from ctFIRE. Then all fibers in a certain layer were combined. The parameters of this function for each layer were fitted using Maximum Likelihood Estimation (MLE) using Matlab. Figure 37 showed the distribution and fitted PDF of one representative case.

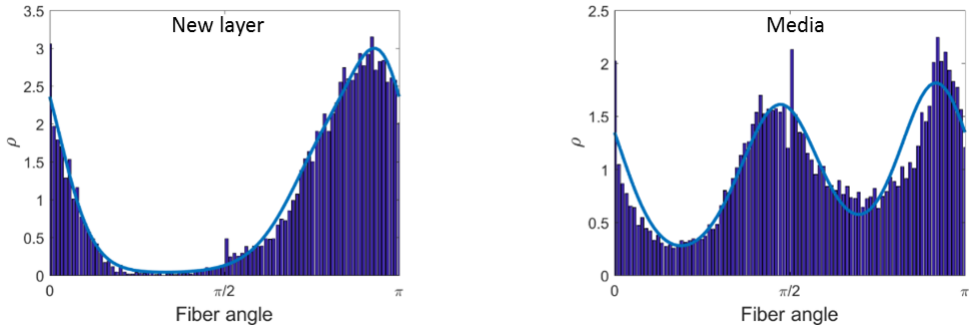

Figure 37 Angle distribution of new layer and media. The smooth lines are the fitted Bimodal von Mises functions

Appendix B Added Information on Rabbit Aneurysm

Appendix B.1 Analysis of Wall Thickness and Endothelial Cell Coverage

Appendix B.1.1 Detailed Wall Thickness

As discussed in Chapter 3, the mechanical testing and MPM imaging were performed on half of the aneurysm wall. The dorsal half was kept in Mayo Clinic for biology and histology studies. Then this half was embedded in paraffin and sent to University of Pittsburgh. The embedded pieces were scanned under high resolution micro-CT scanner (Skyscan 1272, Bruker Micro-CT, Kontich, Belgium) at a resolution of 3 μm. The scan was reconstructed using NRecon (Bruker Micro-CT, Kontich, Belgium). The surface mesh was generated using Simpleware ScanIP (Synopsys, Mountain View, USA) after several operations included segementation and Gaussian smoothing. The thickness information was evaluated after importing the surface mesh into Materialise 3-matic (Leuven, Belgium). The statistics, such as mean thickness, standard deviation of thickness, of selected regions was obtained, Figure 38.

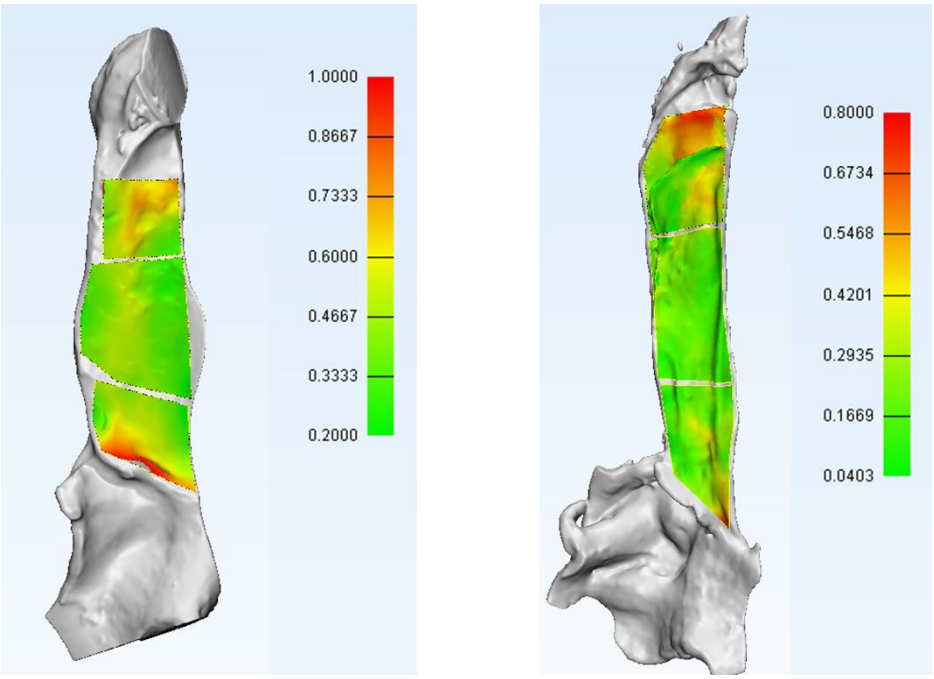

Figure 38 Thickness heat maps of two representative cases (scale: mm). The aneurysm part was further separated into 3 regions.

Appendix B.1.2 CD31 Cell Score

This section is based on joint work with Mayo Clinic (PI: Dr. David Kallmes).

To assess the coverage of endothelial cells of aneurysm wall, CD31 antibody staining was applied. The dorsal half of the aneurysm tissue was divided into three regions. Endothelial cells coverage of each region was evaluated and ranked by a score from 0 to 5. Each region was scored at five different spots. The explanation of the score was listed below:

- Score 0: completely lacking CD31 positive cells coverage
- Score 1: scattered, sparse, several cells which are positive for CD31

- Score 2: small, isolated, patchy, cell clusters are positive for CD31
- Score 3: the cell clusters which are positive for CD31 are much larger than that in 2 above
- Score 4: majority of the lumen side of the wall is still covered with CD31 + cells, with the exception of some small gaps among cells
- Score 5: the lumen side of the wall is still completely covered with CD31 + cells.

The represented images of covered endothelial cells at different scales were shown in Figure 39.

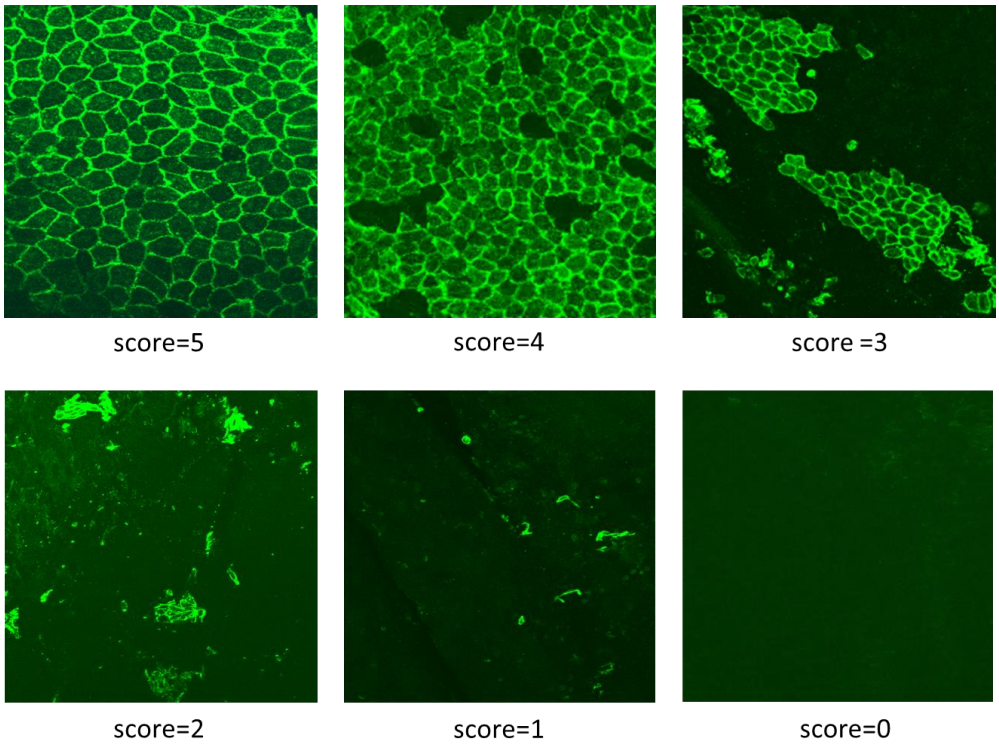

Figure 39 Representative images taken from samples to show the score of endothelial cells coverage

Appendix B.1.3 Relationship between Cell Score and Wall Thickness

As discussed in the previous two sections, the scores of endothelial cell coverage and thickness at different regions of all aneurysm tissues were obtained, Figure 40. After combing all regions from all samples (all time points), there was a positive correlation between average cell score and average thickness of regions (r = 0.328, p = 0.012), Figure 41.

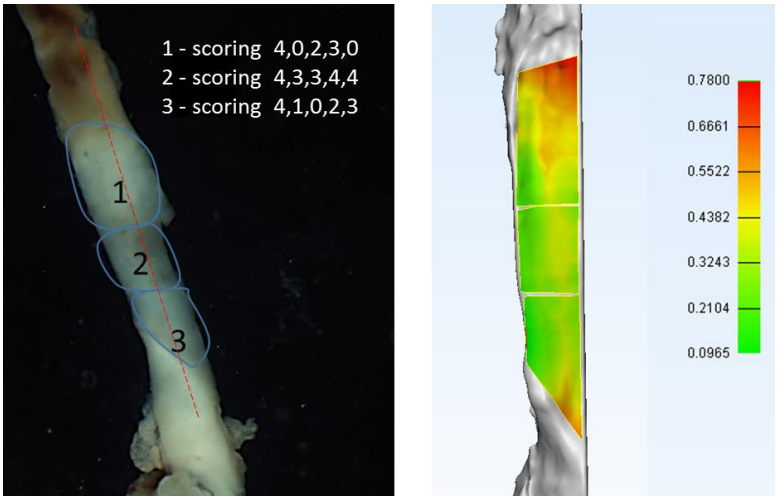

Figure 40 Cell scores of different regions and corresponding wall thickness map (thickness scale: mm)

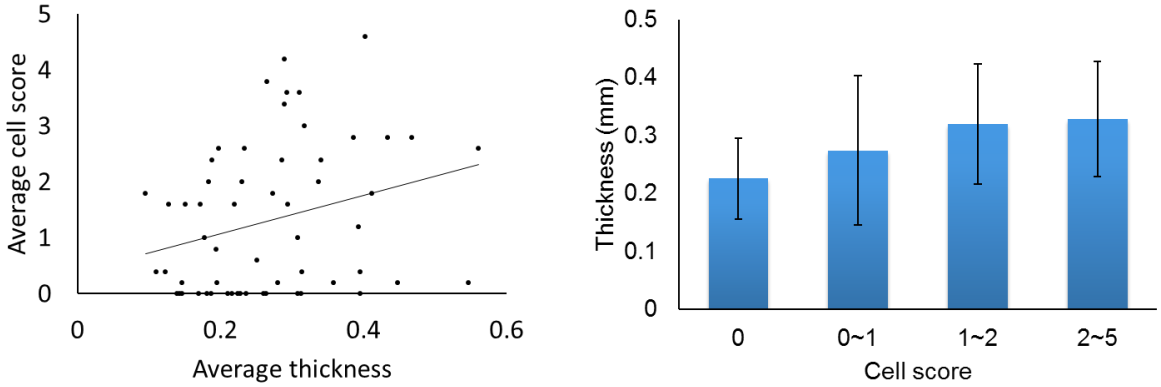

Figure 41 Correlation between average cell score and average wall thickness

Appendix B.1.4 Heterogeneity of Wall Thickness and Strength

For each case, the mean and standard deviation of wall thickness of an aneurysm region was obtained from Materialise 3-matic. There was no correlation between average wall thickness and wall strength. However, there was a negative correlation between standard deviation of wall thickness and ultimate stress (r = -0.519, p = 0.04), Figure 42. This suggests that the aneurysms with heterogeneous wall thickness are likely to be more vulnerable.

It should be noted here, the wall thickness and ultimate stress were measured on different tissue pieces of the same sample.

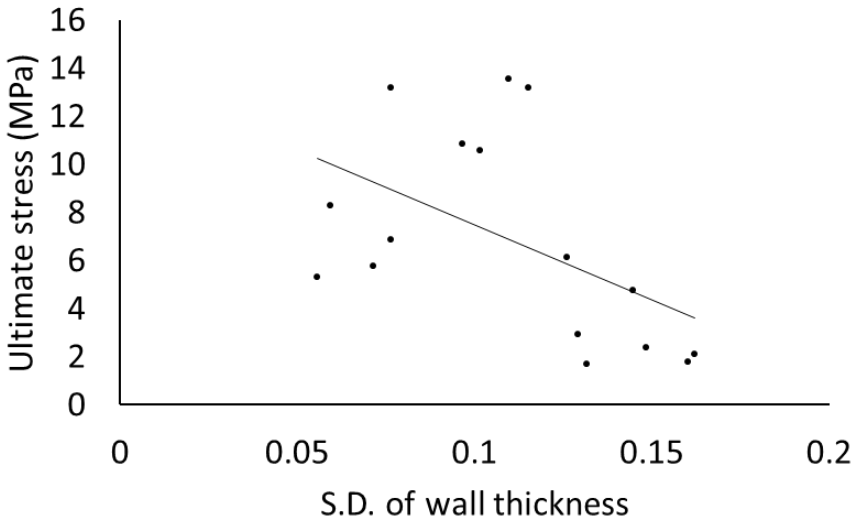

Figure 42 The ultimate strength of the tissue is negatively correlated with standard deviation

Appendix B.2 Biaxial Response of Rabbit Aneurysms

Aneurysm cases that had a sufficiently large piece of tissue (greater than 5 mm by 5 mm) were also tested biaxially using custom built biaxial testing system [96]. It was the same system as described in Chapter 3. However, four biorakes were used to mount a square piece of specimen. The testing protocol was exactly the same as described in Section 3.2.3. Due to the diversity in mechanical properties of the remodeled tissue, the maximum stretch was tissue specific and chosen in real time to avoid overextension of collagen fibers as seen under MPM and determined by reaching the high stiffness region of the loading curve based on load cell measurements. Seven cases of rabbit aneurysm tissues were tested equi-biaxially in longitudinal and circumferential directions. The mechanical responses were shown in Figure 43.

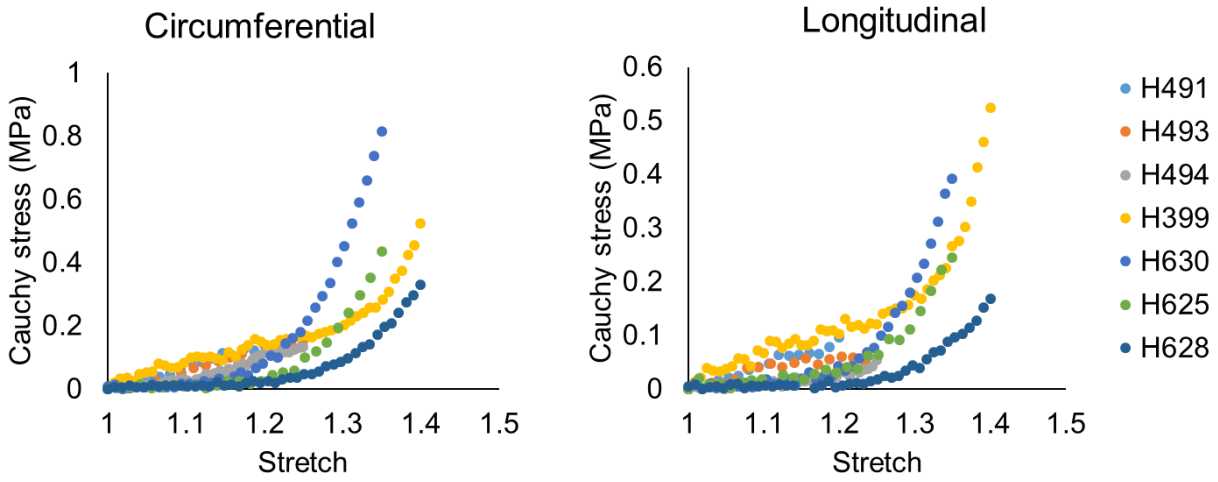

Figure 43 Equi-biaxial mechanical responses of seven rabbit aneurysm cases

In Figure 17, it has been already shown that dispersed fibers in new layer can reorient and bear load in the longitudinal direction. The MPM images were also collected simultaneously when the specimens loaded biaxially. The orientation of fibers in new layer showed minimal change under equi-biaxial loading, Figure 44. This confirms the ability to bear biaxial loading of the new layer.

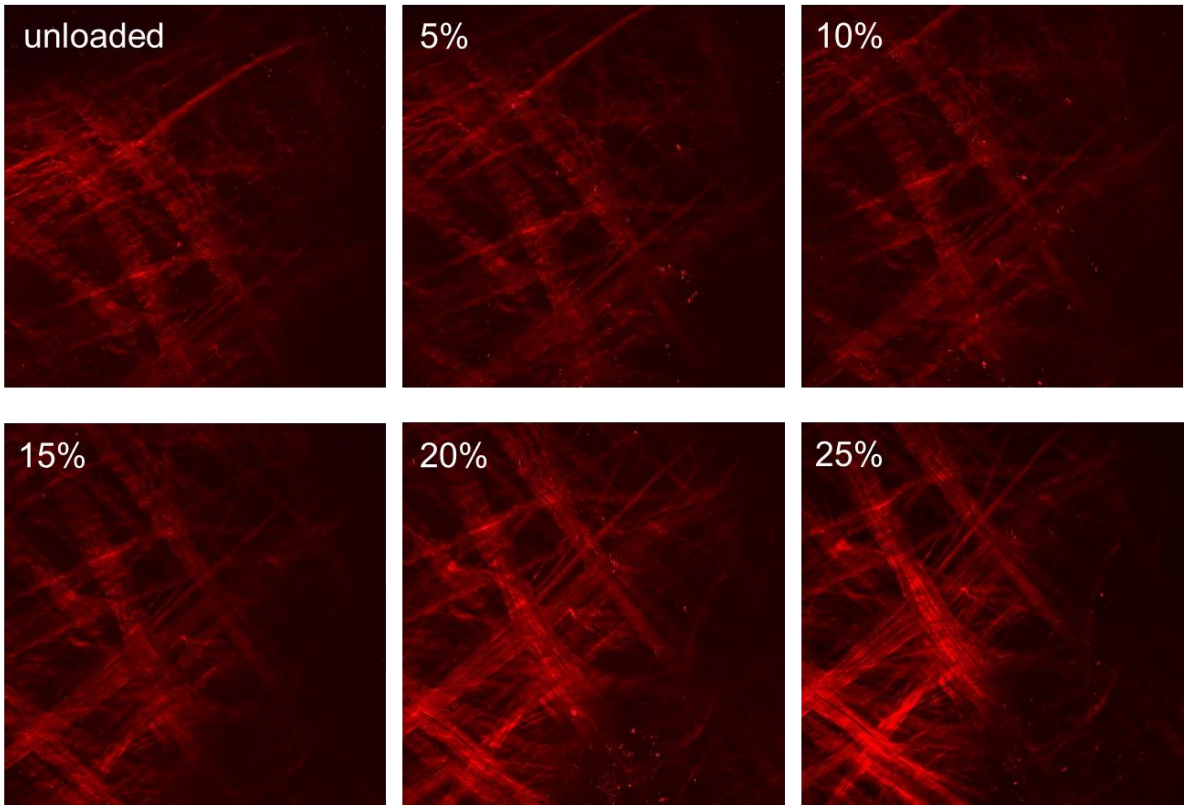

Figure 44 Collagen fibers in the new layer of aneurysm under equi-biaxial loading (Case H491)

Appendix C Visualization of Collagen Fibers and Calcification

Appendix C.1 Introduction

High-resolution micro-CT provides great details on the extent and distribution of calcifications in the wall, as discussed in Chapter 4. The size and distribution of calcifications can alter the mechanical stress. Meanwhile, collagen fibers are the major passive load bearing component in the wall. The relationship between calcification and collagen fibers can have large impact on the mechanical properties, such as stiffness and strength, of the arterial wall. To study this relationship, an established protocol was applied for visualizing collagen fibers and calcifications simultaneously [146]. The tissues were imaged under MPM after staining using OsteoSense. Calcifications with different sizes were found and different patterns of relationship between calcification and collagen were discovered.

Appendix C.2 Methods

Appendix C.2.1 Tissue Acquisition

Circles of Willis were obtained during autopsy from patients (Alzheimer's Disease Research Center Brain Bank, University of Pittsburgh). Samples were fixed in 4% paraformaldehyde (PFA) within 5 hours after autopsy. Segments of middle cerebral artery (MCA), internal carotid artery (ICA) or vertebral artery (VA) were cut from different circles.

Appendix C.2.2 Micro-CT Scanning

Arterial segments were scanned under a high resolution micro-CT scanner and scans were reconstructed as described in detail in Section 4.2.2. Briefly, arterial segments were scanned with a resolution between 3 μm to 5 μm. Then the 3D reconstructed images were created in NRecon. The calcification and non-calcified tissue were segmented into different masks by thresholding and a series of other operations.

Appendix C.2.3 MPM Imaging

To visualize the relationship between calcification and collagen fibers in regions of interest (ROIs) that were identified from micro-CT scanning, collagen and calcification were imaged simultaneously under MPM as described previously [146]. Briefly, tissues were stained in diluted (1:50) OsteoSense 680EX (Perkin Elmer, Waltham, MA) for 24 hours after micro-CT scanning. Samples were then rinsed using PBS and imaged under MPM with an excitation wavelength of 800 nm (same device as described in Section 3.2.3). The second harmonic generation (SHG) signal of collagen was collected using a 400 nm filter. Signal from calcification was collected using the fluorescent calcium tracer emission in the range of 665 to 735 nm.

Appendix C.2.4 Post-processing MPM Images

To better visualize the relationship between collagen and calcification, the MPM stacks were imported in Imaris 9.2 (Bitplane, Switzerland) and 3D reconstructed.

Appendix C.3 Results

Appendix C.3.1 Calcifications at Different Spots of One MCA Case

Different types of calcification were found in segment of MCA. From the dissecting scope image, yellow plaque-like region was shown in the middle of the segment, Figure 45(a). After reconstructing the micro-CT data, dense collection of calcification particles was found in the same yellow region, Figure 45(b). To visualize the collagen fibers in different regions, four different ROIs were imaged under MPM, Figure 45(c). The first ROI was chosen in the middle of the yellow region, which also has the highest density of calcification. A second ROI was chosen on the edge of the calcified region and non-calcified region. The third ROI was chosen away from the calcified region where the tissue was relatively transparent. Due to the thickness of the sample, it was not possible to image across the entire sample from one side. Therefore, these three ROIs were imaged from both luminal and abluminal sides. The fourth ROI was also imaged from luminal side to visualize the heterogeneity of IEL.

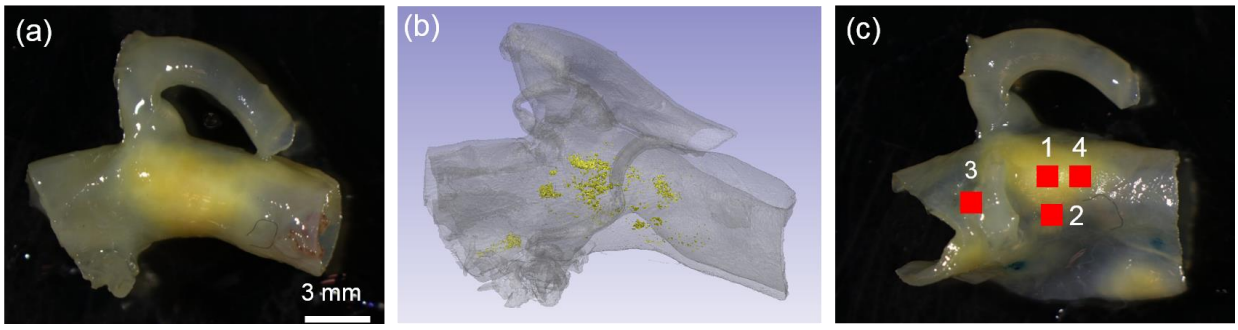

Figure 45 Micro-CT reconstruction of MCA (CW19-005) and ROIs for MPM imaging. (a) Dissecting scope image; (b) reconstruction of micro-CT (calcification shows up as gold); (c) locations of four ROIs under MPM

From the abluminal side imaging, collagen fibers showed different distributions of orientation in the first three ROIs, Figure 46. Fibers majorly aligned in the circumferential direction at the non-calcified region, Figure 46(c,f), while fibers in the calcified region and edge had a more dispersed distribution, Figure 46(a,b). The calcification imaged from the abluminal side showed more micro-calcifications with a size less than 10 μm and was located between collagen fibers. Calcification particles in these three ROIs showed similar presentation with respect to size and distribution between fibers. However, the density of calcification particles at the third ROI was lower than the other two locations. The larger calcification seen under micro-CT was not visible in MPM, likely due to the loss of signal when imaging through the dense fibers.

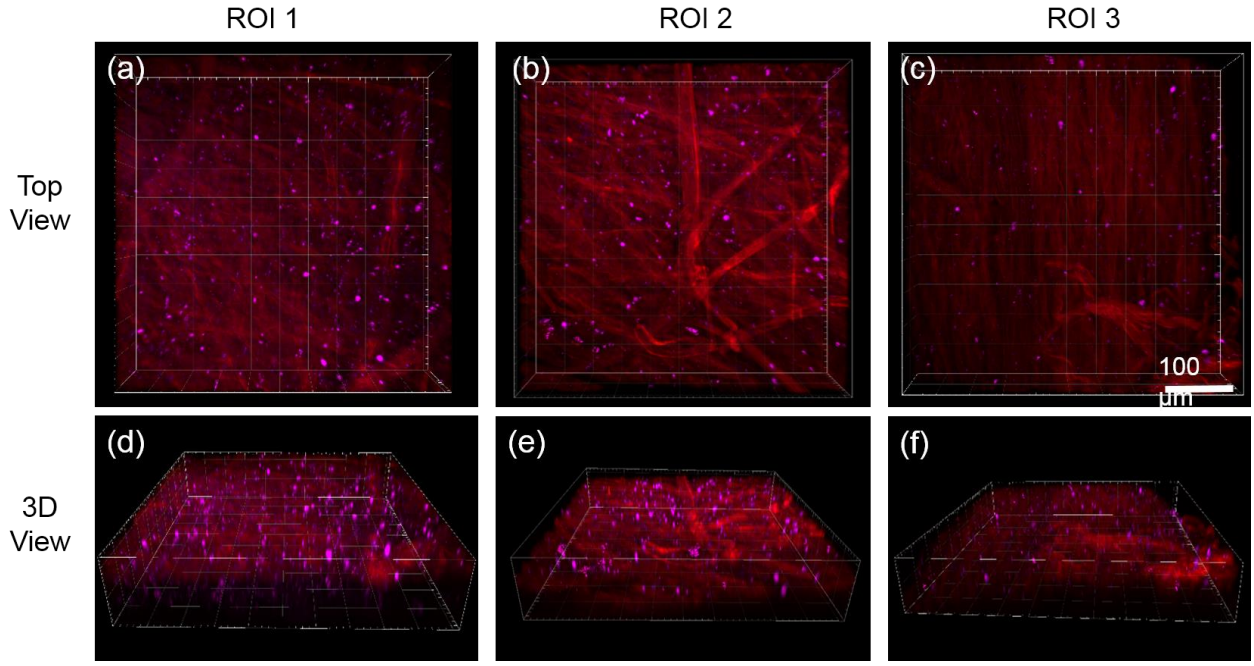

Figure 46 Micro-calcification was sparsely distributed in the adventitia of different ROIs (imaged from abluminal side; collagen – red, calcification – magenta)

Collagen fiber imaged from luminal side differed between ROI 1 and 2, Figure 47(a,b). At ROI 1, collagen fiber is degraded and absent at the location where calcification presents. This displays a similar pattern to that found in human cerebral aneurysm tissues [146]. At ROI 2, one part of the imaged region was filled with collagen and the other part was only calcification, Figure 47(b). Collagen fibers away from the calcification align in a direction that is perpendicular to the edge. When approaching to the calcification, fibers either stopped or changed their orientation to follow along the edge of calcification.

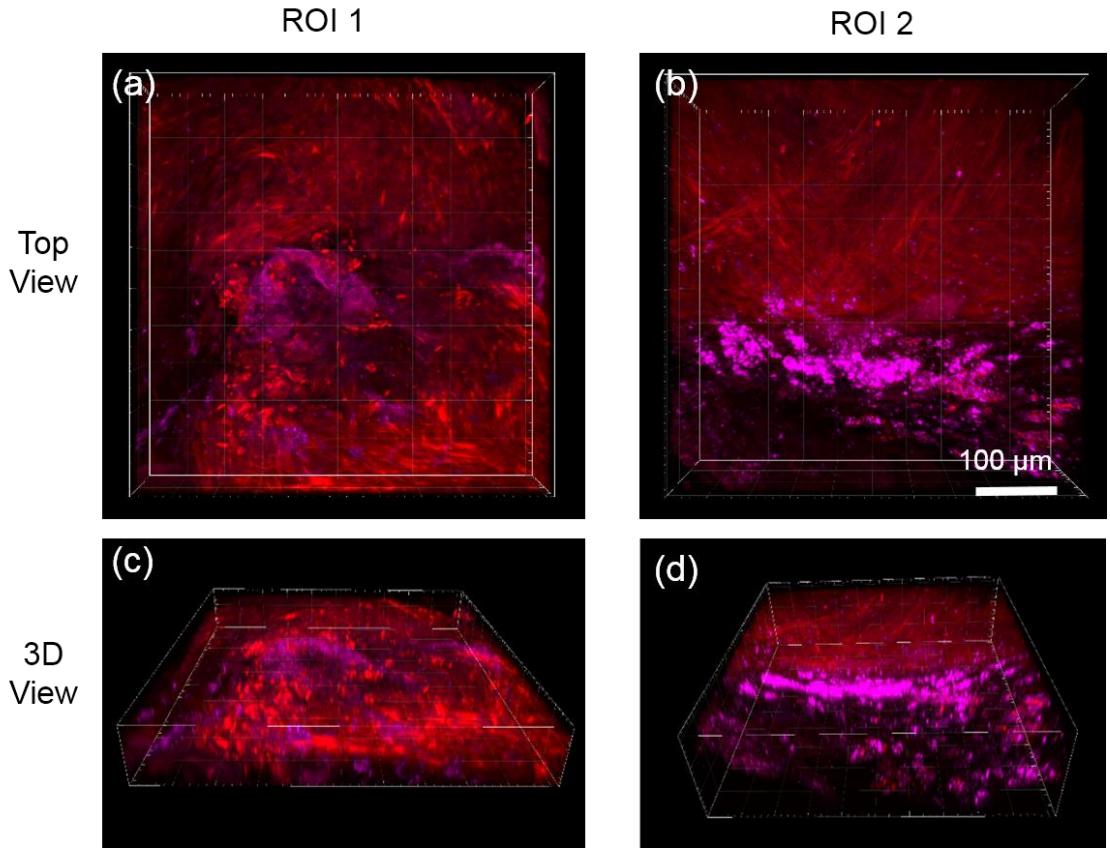

Figure 47 Collagen fibers and calcification imaged from luminal side at different ROIs (collagen – red, calcification – magenta)

Notably, no collagen was found in the calcified region suggesting this cluster was surrounded by lipid or other non-collagenous matrix material. For ROI 3, the internal elastic lamella (IEL) is intact and dense, Figure 48(a,b), The strong autofluorescence from the IEL interfered with the SHG signal from collagen, so that the collagen fibers in this region could not be imaged.

There was no IEL in ROI 1 and 2. However, disrupted IEL fragments were found at ROI 4 as labeled in Figure 45(c), Figure 48(c,d),.

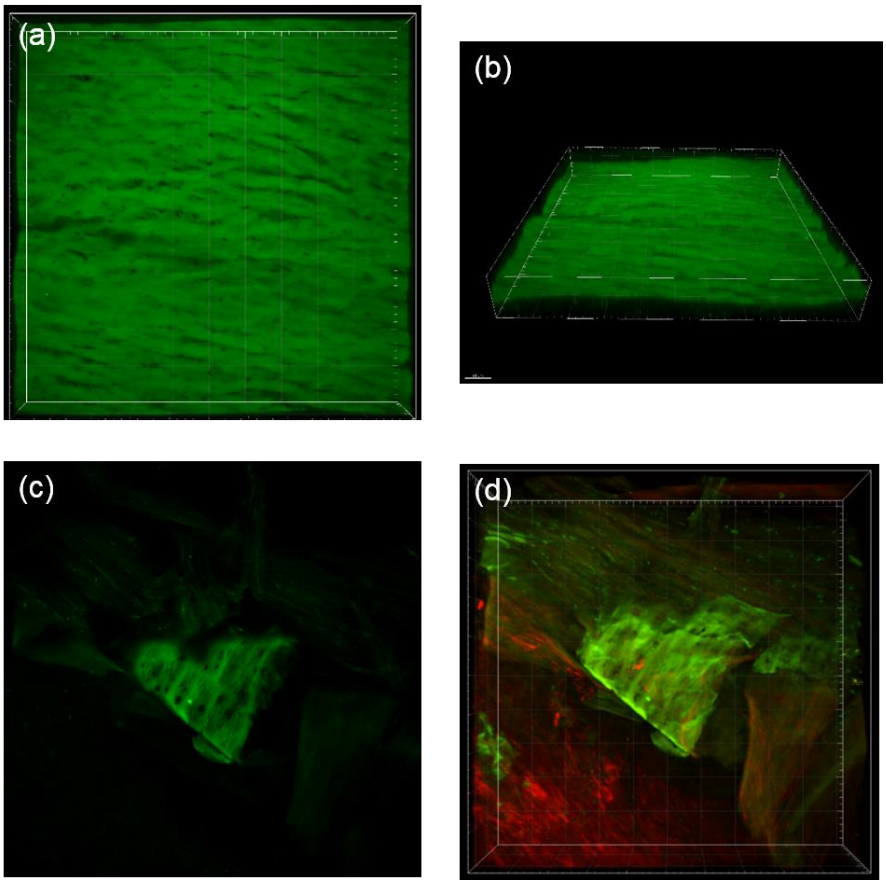

Figure 48 Internal Elastic Lamella (IEL). (a,b) Intact IEL at ROI 3; (c) Heart-shaped IEL fragment at ROI 4; (d) combined SHG and 2PI signal showing collagen and elastin.

Appendix C.3.2 Calcifications of Other Arteries

Micro-calcification with a size below 50 μm is easy to be detected under MPM, Figure 49. MPM imaging on one ICA (Figure 49, first row) showed that the micro-calcification concentrated at locations that collagen was absent. For other cases, micro-calcification entities were visible at gaps between fibers, Figure 49(f) and Figure 50(d). Large calcification clusters were found under adventitial collagen in highly calcified artery. The calcification located at different depths from collagen and formed a separate layer. Figure 50(f).

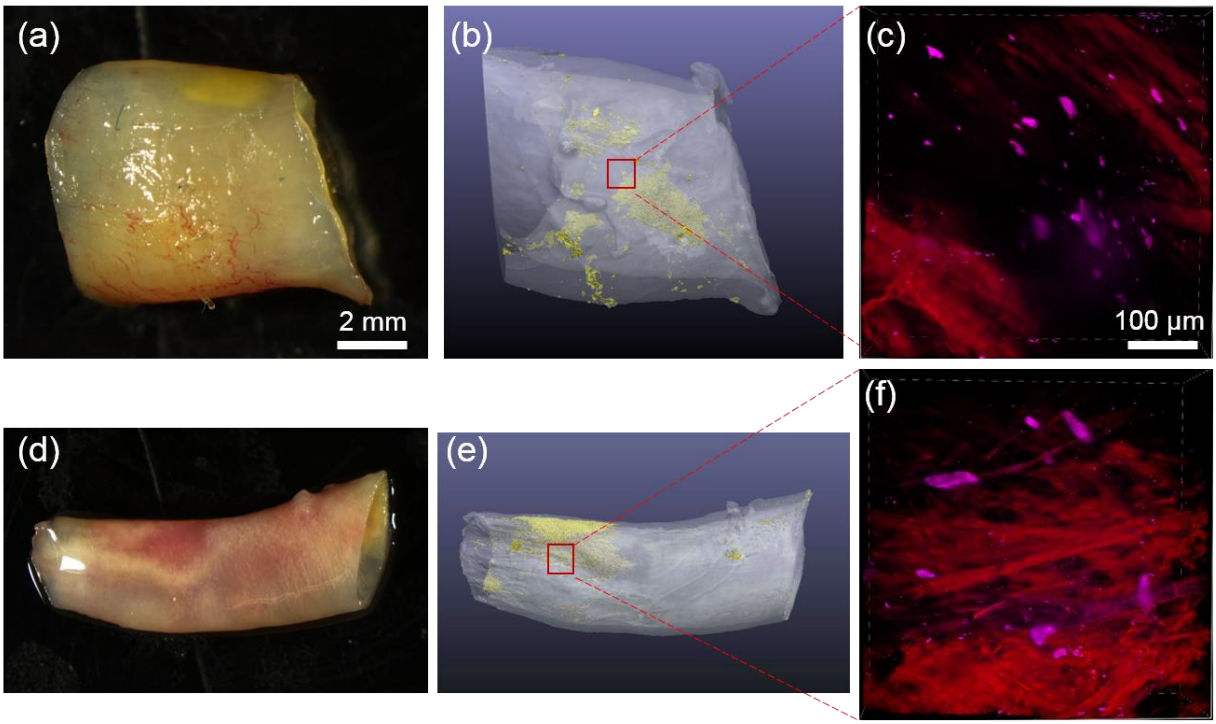

Figure 49 Calcifications in ICA and Vertebral artery (VA). First row represents one segment of ICA (CAF-18); second row represents one segment of vertebral artery (CW17-006). (a) Dissection scope image of ICA; (b) micro-CT reconstruction of ICA (calcifications with yellow color); (c) MPM image of sample at location identifed in (b) with Osteosense showing calcification in magenta; (d) Dissection scope image of VA; (e) micro-CT reconstruction of VA; (f) MPM image of sample at location identifed in (e).

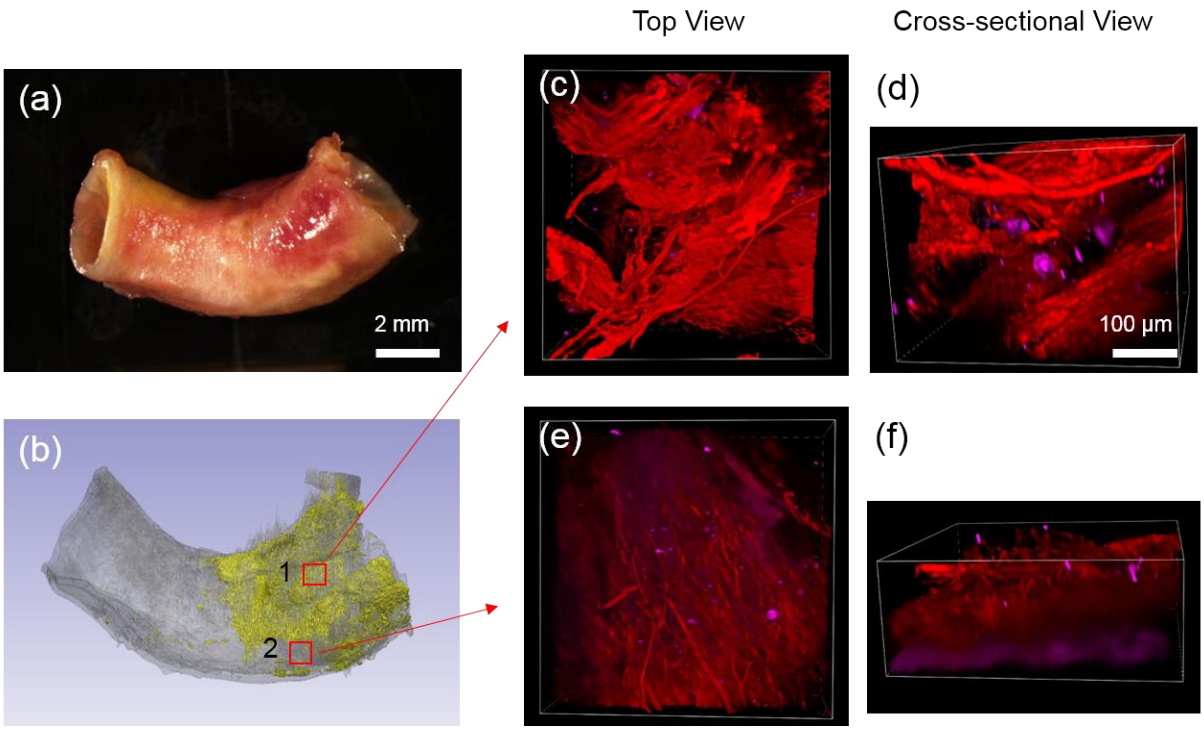

Figure 50 MPM images of highly calcified ICA (CW17-003). (a) Dissection scope image of ICA; (b) micro-CT reconstruction shows the highly calcified tissue; (c-f) MPM images of two ROIs.

Appendix C.4 Discussion

Micro-calcifications were widely distributed in the artery, both in the media and the adventitia, Figure 46 and Figure 49. The small particles were present at the space between collagen fibers. No particular interaction was found between collagen and micro-calcification. It seems unlikely, the presence of these isolated micro-calcifications would mechanically influence the collagen fibers. However, micro-calcification particles were found in collections of clusters which would be expected to alter the mechanical role of the collagen fibers in that region, possibly in a

manner similar to a single large calcification, Figure 47(a,c). Similar clusters were found in human aneurysms [146] and found to be associated with degenerated collagen fibers. For larger calcifications (with a size greater than 500 μm), the organization of the collagen fibers appeared to be altered by the calcification. For example, in one case, as fibers were traced back to the edge of the calcification, they were seen to change from an orthogonal to parallel alignment to the calcification, Figure 47(b,d). In another case, a macro-calcification was found to lie in a region between collagen layers, Figure 50(f).

Bibliography

[1] Juvela, S., Porras, M., and Poussa, K., 2008, "Natural History of Unruptured Intracranial Aneurysms: Probability of and Risk Factors for Aneurysm Rupture," J. Neurosurg., **108**, pp. 1052–1060.

[2] Fennell, V. S., Kalani, M. Y. S., Atwal, G., Martirosyan, N. L., and Spetzler, R. F., 2016, "Biology of Saccular Cerebral Aneurysms: A Review of Current Understanding and Future Directions," Front. Surg., **3**(July), p. 43.

[3] Wiebers, D. O., Whisnant, J. P., Sundt, T. M., and O'Fallon, W. M., 1987, "The Significance of Unruptured Intracranial Saccular Aneurysms," J. Neurosurg., **66**, pp. 23–29.

[4] Lall, R. R., Eddleman, C. S., Bendok, B. R., and Batjer, H. H., 2009, "Unruptured Intracranial Aneurysms and the Assessment of Rupture Risk Based on Anatomical and Morphological Factors: Sifting through the Sands of Data," Neurosurg. Focus, **26**(May), p. E2.

[5] Mitchell, P., Gholkar, A., Vindlacheruvu, R. R., and Mendelow, A. D., 2004, "Unruptured Intracranial Aneurysms: Benign Curiosity or Ticking Bomb?," Lancet Neurol., **3**(2), pp. 85–92.

[6] Xiang, J., Natarajan, S. K., Tremmel, M., Ma, D., Mocco, J., Hopkins, L. N., Siddiqui, A. H., Levy, E. I., and Meng, H., 2011, "Hemodynamic-Morphologic Discriminants for Intracranial Aneurysm Rupture," Stroke, **42**(1), pp. 144–152.

[7] Utter, B., and Rossmann, J. S., 2007, "Numerical Simulation of Saccular Aneurysm Hemodynamics: Influence of Morphology on Rupture Risk," J. Biomech., **40**(12), pp. 2716–2722.

[8] Ishibashi, T., Murayama, Y., Urashima, M., Saguchi, T., Ebara, M., Arakawa, H., Irie, K., Takao, H., and Abe, T., 2009, "Unruptured Intracranial Aneurysms: Incidence of Rupture and Risk Factors," Stroke, **40**(1), pp. 313–316.

[9] Raghavan, M. L., Ma, B., and Harbaugh, R. E., 2005, "Quantified Aneurysm Shape and Rupture Risk," J. Neurosurg., **102**(2), pp. 355–362.

[10] Frösen, J., Piippo, A., Paetau, A., Kangasniemi, M., Niemelä, M., Hernesniemi, J., and Jääskeläinen, J., 2004, "Remodeling of Saccular Cerebral Artery Aneurysm Wall Is Associated with Rupture: Histological Analysis of 24 Unruptured and 42 Ruptured Cases," Stroke, **35**(10), pp. 2287–2293.

[11] Robertson, A. M., Duan, X., Aziz, K. M., Hill, M. R., Watkins, S. C., and Cebral, J. R., 2015, "Diversity in the Strength and Structure of Unruptured Cerebral Aneurysms," Ann. Biomed. Eng., **43**(7), pp. 1502–1515.

[12] Duan, X., 2016, "The Link between Hemodynamics and Wall Structure in Cerebral Aneurysms," Doctoral Dissertation, University of Pittsburgh.

[13] Villablanca, J. P., Duckwiler, G. R., Jahan, R., Tateshima, S., Martin, N. A., Frazee, J., Gonzalez, N. R., Sayre, J., and Vinuela, F. V., 2013, "Natural History of Asymptomatic Unruptured Cerebral Aneurysms Evaluated at CT Angiography: Growth and Rupture Incidence and Correlation with Epidemiologic Risk Factors," Radiology, **269**(1), pp. 258–265.

[14] Brinjikji, W., Zhu, Y.-Q., Lanzino, G., Cloft, H. J., Murad, M. H., Wang, Z., and Kallmes, D. F., 2016, "Risk Factors for Growth of Intracranial Aneurysms: A Systematic Review and Meta-Analysis," Am. J. Neuroradiol., **37**(4), pp. 615–620.

[15] Leemans, E. L., Cornelissen, B. M. W., Said, M., Berg, R. van den, Slump, C. H., Marquering, H. A., and Majoie, C. B. L. M., 2019, "Intracranial Aneurysm Growth: Consistency of Morphological Changes," Neurosurg. Focus FOC, **47**(1), p. E5.

[16] Leemans, E. L., Cornelissen, B. M. W., Slump, C. H., Majoie, C. B. L. M., Cebral, J. R., and Marquering, H. A., 2019, "Comparing Morphology and Hemodynamics of Stable-versus-Growing and Grown Intracranial Aneurysms," Am. J. Neuroradiol., **40**(12), pp. 2102–2110.

[17] Yamano, A., Yanaka, K., Uemura, K., Onuma, K., Nakamura, K., and Ishikawa, E., 2018, "Bleb Formation in Small Unruptured Intracranial Aneurysm as a Predictor of Early Rupture," J. Surg. Case Reports, **2018**(5).

[18] Salimi Ashkezari, S. F., Detmer, F. J., Mut, F., Chung, B. J., Yu, A. K., Stapleton, C. J., See, A. P., Amin-Hanjani, S., Charbel, F. T., Rezai Jahromi, B., Niemelä, M., Frösen, J., Zhou, J., Maiti, S., Robertson, A. M., and Cebral, J. R., 2020, "Blebs in Intracranial Aneurysms: Prevalence and General Characteristics," J. Neurointerv. Surg., p. neurintsurg-2020-016274.

[19] Salimi Ashkezari, S. F., Mut, F., Chung, B. J., Robertson, A. M., and Cebral, J. R., 2020, "Hemodynamic Conditions That Favor Bleb Formation in Cerebral Aneurysms," J. Neurointerv. Surg., p. neurintsurg-2020-016369.

[20] Cebral, J. R., Duan, X., Chung, B. J., Putman, C., Aziz, K. M., and Robertson, A. M., 2015, "Wall Mechanical Properties and Hemodynamics of Unruptured Intracranial Aneurysms," Am. J. Neuroradiol., **36**(9), pp. 1695–1703.

[21] Cebral, J. R., Ollikainen, E., Chung, B. J., Mut, F., Sippola, V., Jahromi, B. R., Tulamo, R., Hernesniemi, J., Niemela, M., Robertson, A. M., and Frosen, J., 2017, "Flow Conditions in the Intracranial Aneurysm Lumen Are Associated with Inflammation and Degenerative Changes of the Aneurysm Wall," Am. J. Neuroradiol., **38**(1), pp. 119–126.

[22] The UCAS Japan Investigators, 2012, "The Natural Course of Unruptured Cerebral Aneurysms," Neurosurgery, **366**(26), pp. 2474–2482.

[23] Nyström, S. H. M., 1970, "On Factors Related to Growth and Rupture of Intracranial Aneurysms," Acta Neuropathol., **16**(1), pp. 64–72.

[24] Bhatia, S., Sekula, R. F., Quigley, M. R., Williams, R., and Ku, A., 2011, "Role of Calcification in the Outcomes of Treated, Unruptured, Intracerebral Aneurysms," Acta Neurochir. (Wien)., **153**(4), pp. 905–911.

[25] Gade, P. S., Tulamo, R., Lee, K., Mut, F., Ollikainen, E., Chuang, C.-Y., Jae Chung, B., Niemelä, M., Rezai Jahromi, B., Aziz, K., Yu, A., Charbel, F. T., Amin-Hanjani, S., Frösen, J., Cebral, J. R., and Robertson, A. M., 2019, "Calcification in Human Intracranial Aneurysms Is Highly Prevalent and Displays Both Atherosclerotic and Nonatherosclerotic Types," Arterioscler. Thromb. Vasc. Biol., **39**(10), pp. 2157–2167.

[26] Sang, C., Maiti, S., Fortunato, R., Kofler, J., and Robertson, A. M., 2018, "A Uniaxial Testing Approach for Consistent Failure in Vascular Tissues," J. Biomech. Eng., **140**(6), p. 061010.

[27] Adams, H. P., Butler, M. J., Biller, J., and Toffol, G. J., 1986, "Nonhemorrhagic Cerebral Infarction in Young Adults.," Arch. Neurol., **43**(8), pp. 793–6.

[28] Broderick, J. P., Brott, T., Tomsick, T., Miller, R., and Huster, G., 1993, "Intracerebral Hemorrhage More than Twice as Common as Subarachnoid Hemorrhage.," J. Neurosurg., **78**(2), pp. 188–91.

[29] Hart, R., and Easton, J., 1985, "Dissections.," Stroke, **16**, pp. 925–927.

[30] Kelly, P. J., Stein, J., Shafqat, S., Eskey, C., Doherty, D., Chang, Y., Kurina, a, and Furie, K. L., 2001, "Functional Recovery after Rehabilitation for Cerebellar Stroke.," Stroke., **32**(2), pp. 530–534.

[31] Upchurch, G. R., and Schaub, T. A., 2006, "Abdominal Aortic Aneurysm," Am. Fam. Physician, **73**(7), pp. 1198–1206.

[32] Shaw, C.-M., and Alvord, E., 1972, "Injury of the Basilar Artery Associated with Closed Head Trauma," J. Neurol. Neurosurg. Psychiatry, **35**(2), pp. 247–257.

[33] Claes, E., Atienza, J. M., Guinea, G. V, Rojo, F. J., Bernal, J. M., Revuelta, J. M., and Elices, M., 2010, "Mechanical Properties of Human Coronary Arteries," 2010 Annu. Int. Conf. IEEE Eng. Med. Biol., **2010**, pp. 3792–3795.

[34] Holzapfel, G. a, Holzapfel, G. a, Sommer, G., Sommer, G., Gasser, C. T., Gasser, C. T., Regitnig, P., Regitnig, P., A, G., and A, G., 2005, "Determination of Layer-Specfic Mechanical Properties of Human Coronary Arteries with Nonatherosclerotic Intimal Thickening and Related Constitutive Modeling," Hear. Circ. Physiol., **289**(5), pp. 2048–2058.

[35] Pichamuthu, J. E., Phillippi, J. A., Cleary, D. A., Chew, D. W., Hempel, J., Vorp, D. A., and Gleason, T. G., 2013, "Differential Tensile Strength and Collagen Composition in Ascending Aortic Aneurysms by Aortic Valve Phenotype.," Ann. Thorac. Surg., **96**(6), pp. 2147–54.

[36] Raghavan, M. L., Webster, M. W., and Vorp, D. A., 1996, "Ex Vivo Biomechanical Behavior of Abdominal Aortic Aneurysm: Assessment Using a New Mathematical Model," Ann Biomed Eng, **24**(5), pp. 573–582.

[37] Raghavan, M. L., Hanaoka, M. M., Kratzberg, J. A., Higuchi, M. de L., and da Silva, E. S., 2011, "Biomechanical Failure Properties and Microstructural Content of Ruptured and Unruptured Abdominal Aortic Aneurysms," J. Biomech., **44**(13), pp. 2501–2507.

[38] Teng, Z., Tang, D., Zheng, J., Woodard, P. K., and Hoffman, A. H., 2009, "An Experimental Study on the Ultimate Strength of the Adventitia and Media of Human Atherosclerotic Carotid Arteries in Circumferential and Axial Directions," J. Biomech., **42**(15), pp. 2535–2539.

[39] Vorp, D. A., Schiro, B. J., Ehrlich, M. P., Juvonen, T. S., Ergin, M. A., and Griffith, B. P., 2003, "Effect of Aneurysm on the Tensile Strength and Biomechanical Behavior of the Ascending Thoracic Aorta," Ann. Thorac. Surg., **75**(4), pp. 1210–1214.

[40] Ferrara, A., Morganti, S., Totaro, P., Mazzola, A., and Auricchio, F., 2016, "Human Dilated Ascending Aorta: Mechanical Characterization via Uniaxial Tensile Tests," J. Mech. Behav. Biomed. Mater., **53**, pp. 257–271.

[41] Forsell, C., Swedenborg, J., Roy, J., and Gasser, T. C., 2013, "The Quasi-Static Failure Properties of the Abdominal Aortic Aneurysm Wall Estimated by a Mixed Experimental-Numerical Approach," Ann. Biomed. Eng., **41**(7), pp. 1554–1566.

[42] García-Herrera, C. M., Atienza, J. M., Rojo, F. J., Claes, E., Guinea, G. V., Celentano, D. J., García-Montero, C., and Burgos, R. L., 2012, "Mechanical Behaviour and Rupture of Normal and Pathological Human Ascending Aortic Wall," Med. Biol. Eng. Comput., **50**(6), pp. 559–566.

[43] Mohan, D., and Melvin, J. W., 1982, "Failure Properties of Passive Human Aortic Tissue. I—Uniaxial Tension Tests," J. Biomech., **15**(11), pp. 887–902.

[44] Okamoto, R. J., Wagenseil, J. E., DeLong, W. R., Peterson, S. J., Kouchoukos, N. T., and Sundt, T. M., 2002, "Mechanical Properties of Dilated Human Ascending Aorta," Ann. Biomed. Eng., **30**(5), pp. 624–635.

[45] Korenczuk, C. E., Votava, L. E., Dhume, R. Y., Kizilski, S. B., Brown, G. E., Narain, R., and Barocas, V. H., 2017, "Isotropic Failure Criteria Are Not Appropriate for Anisotropic Fibrous Biological Tissues," J. Biomech. Eng., **139**(7), p. 071008.

[46] Stemper, B. D., Yoganandan, N., Stineman, M. R., Gennarelli, T. A., Baisden, J. L., and Pintar, F. A., 2007, "Mechanics of Fresh, Refrigerated, and Frozen Arterial Tissue," J. Surg. Res., **139**(2), pp. 236–242.

[47] Shah, S. B., Witzenburg, C., Hadi, M. F., Wagner, H. P., Goodrich, J. M., Alford, P. W., and Barocas, V. H., 2014, "Prefailure and Failure Mechanics of the Porcine Ascending Thoracic Aorta: Experiments and a Multiscale Model," J. Biomech. Eng., **136**(2), p. 021028.

[48] ASTM, 2006, "D412-06 Standard Test Methods for Vulcanized Rubber and Thermoplastic Elastomers–Tension," ASTM Int. West Conshohoken, PA, USA, (Reapproved 2013), pp. 1–14.

[49] Fortunato, R. N., Sang, C., Robertson, A. M., and Maiti, S., 2017, "Computational Study of Uniaxial Tension Testing," *5th International Conference on Computational and Mathematical Biomedical Engineering - CMBE2017*, P. Nithiarasu, and A. Robertson, eds., University of Pittsburgh, Pittsburgh, PA, pp. 1304–1307.

[50] Jacobs, N. T., Cortes, D. H., Vresilovic, E. J., and Elliott, D. M., 2013, "Biaxial Tension of Fibrous Tissue: Using Finite Element Methods to Address Experimental Challenges Arising from Boundary Conditions and Anisotropy.," J. Biomech. Eng., **135**(2), p. 021004.

[51] Sun, W., Sacks, M. S., and Scott, M. J., 2005, "Effects of Boundary Conditions on the Estimation of the Planar Biaxial Mechanical Properties of Soft Tissues," J. Biomech. Eng., **127**(4), p. 709.

[52] Hill, M. R., Duan, X., Gibson, G. A., Watkins, S., and Robertson, A. M., 2012, "A Theoretical and Non-Destructive Experimental Approach for Direct Inclusion of Measured Collagen Orientation and Recruitment into Mechanical Models of the Artery Wall.," J. Biomech., **45**(5), pp. 762–771.

[53] Nittur, P. G., Maiti, S., and Geubelle, P. H., 2008, "Grain-Level Analysis of Dynamic Fragmentation of Ceramics under Multi-Axial Compression," J. Mech. Phys. Solids, **56**(3), pp. 993–1017.

[54] Monson, K. L., Goldsmith, W., Barbaro, N. M., and Manley, G. T., 2005, "Significance of Source and Size in the Mechanical Response of Human Cerebral Blood Vessels," J. Biomech., **38**, pp. 737–744.

[55] Robertson, A. M., Duan, X., Maiti, S., Thunes, J. R., Gade, P., Aziz, K., Cebral, J. R., Frösen, J., Tulamo, R., Fortunato, R. N., Charbel, F., and Amin-Hanjani, S., 2017, "Role of Calcification in Aneurysm Failure-a Case Study," *5th International Conference on Computational and Mathematical Biomedical Engineering - CMBE2017*, A.M. Robertson, and P. Nithiarasu, eds., University of Pittsburgh, Pittsburgh, PA, pp. 52–55.

[56] Mohan, D., and Melvin, J. W., 1983, "Failure Properties of Passive Human Aortic Tissue. II-Biaxial Tension Tests," J. Biomech., **16**(1).

[57] Lacolley, P., Challande, P., Boumaza, S., Boutouyrie, P., Grimaud, J., Paulin, D., Lamaziere, J. D., and Li, Z., 2001, "Mechanical Properties and Structure of Carotid Arteries in Mice Lacking Desmin ´ ´," **51**(December), pp. 178–187.

[58] Louis, H., Kakou, A., Regnault, V., Labat, C., Bressenot, A., Gao-Li, J., Gardner, H., Thornton, S. N., Challande, P., Li, Z., and Lacolley, P., 2007, "Role of Alpha1beta1-Integrin in Arterial Stiffness and Angiotensin-Induced Arterial Wall Hypertrophy in Mice.," Am. J. Physiol. Heart Circ. Physiol., **293**(4), pp. H2597-604.

[59] Kim, J.-H., Avril, S., Duprey, A., and Favre, J.-P., 2012, "Experimental Characterization of Rupture in Human Aortic Aneurysms Using a Full-Field Measurement Technique.," Biomech. Model. Mechanobiol., **11**(6), pp. 841–53.

[60] Duprey, A., Trabelsi, O., Vola, M., Favre, J. P., and Avril, S., 2016, "Biaxial Rupture Properties of Ascending Thoracic Aortic Aneurysms," Acta Biomater., **42**, pp. 273–285.

[61] Bellini, C., Kristofik, N. J., Bersi, M. R., Kyriakides, T. R., and Humphrey, J. D., 2017, "A Hidden Structural Vulnerability in the Thrombospondin-2 Deficient Aorta Increases the Propensity to Intramural Delamination," J. Mech. Behav. Biomed. Mater., **71**(January), pp. 397–406.

[62] Romo, A., Badel, P., Duprey, A., Favre, J. P., and Avril, S., 2014, "In Vitro Analysis of Localized Aneurysm Rupture," J. Biomech., **47**(3), pp. 607–616.

[63] Stemper, B. D., Yoganandan, N., Sinson, G. P., Gennarelli, T. A., Stineman, M. R., and Pintar, F. A., 2007, "Biomechanical Characterization of Internal Layer Subfailure in Blunt Arterial Injury," Ann. Biomed. Eng., **35**(2), pp. 285–291.

[64] Iliopoulos, D. C., Deveja, R. P., Kritharis, E. P., Perrea, D., Sionis, G. D., Toutouzas, K., Stefanadis, C., and Sokolis, D. P., 2009, "Regional and Directional Variations in the Mechanical Properties of Ascending Thoracic Aortic Aneurysms," Med. Eng. Phys., **31**(1), pp. 1–9.

[65] Cebral, J. R., Duan, X., Gade, P. S., Chung, B. J., Mut, F., Aziz, K., and Robertson, A. M., 2016, "Regional Mapping of Flow and Wall Characteristics of Intracranial Aneurysms," Ann. Biomed. Eng., **44**(12), pp. 3553–3567.

[66] Ng, B. H., Chou, S. M., and Krishna, V., 2005, "The Influence of Gripping Techniques on the Tensile Properties of Tendons," Proc. Inst. Mech. Eng. Part H J. Eng. Med., **219**(5), pp. 349–354.

[67] Nye, K. S., Converse, M. I., Dahl, M. J., Albertine, K. H., and Monson, K. L., 2017, "Development of Mechanical and Failure Properties in Sheep Cerebral Arteries," Ann. Biomed. Eng., **45**(4), pp. 1101–1110.

[68] Robertson, A. M., Hill, M. R., and Li, D., 2012, "Structurally Motivated Damage Models for Arterial Walls. Theory and Application," *Modelling of Physiological Flows*, D. Ambrosi, A. Quarteroni, and G. Rozza, eds., Springer, Milano, pp. 143–185.

[69] Sang, C., Kallmes, D. F., Kadirvel, R., Durka, M. J., Ding, Y.-H., Dai, D., Watkins, S. C., and Robertson, A. M., 2020, "Adaptive Remodeling in the Elastase-Induced Rabbit Aneurysms," Exp. Mech.

[70] Naggara, O. N., Lecler, A., Oppenheim, C., Meder, J. F., and Raymond, J., 2012, "Endovascular Treatment of Intracranial Unruptured Aneurysms: A Systematic Review of the Literature on Safety with Emphasis on Subgroup Analyses," Radiology, **263**(3), pp. 828–835.

[71] Kotowski, M., Naggara, O., Darsaut, T. E., Nolet, S., Gevry, G., Kouznetsov, E., and Raymond, J., 2013, "Safety and Occlusion Rates of Surgical Treatment of Unruptured Intracranial Aneurysms: A Systematic Review and Meta-Analysis of the Literature from 1990 to 2011," J. Neurol. Neurosurg. Psychiatry, **84**(1), pp. 42–48.

[72] Nahed, B. V., DiLuna, M. L., Morgan, T., Ocal, E., Hawkins, A. A., Ozduman, K., Kahle, K. T., Chamberlain, A., Amar, A. P., and Gunel, M., 2005, "Hypertension, Age, and Location Predict Rupture of Small Intracranial Aneurysms.," Neurosurgery, **57**(4), pp. 676–683.

[73] Detmer, F. J., Chung, B. J., Jimenez, C., Hamzei-Sichani, F., Kallmes, D., Putman, C., and Cebral, J. R., 2019, "Associations of Hemodynamics, Morphology, and Patient Characteristics with Aneurysm Rupture Stratified by Aneurysm Location," Neuroradiology, **61**(3), pp. 275–284.

[74] Detmer, F. J., Mut, F., Slawski, M., Hirsch, S., Bijlenga, P., and Cebral, J. R., 2020, "Incorporating Variability of Patient Inflow Conditions into Statistical Models for Aneurysm Rupture Assessment," Acta Neurochir. (Wien)., **162**(3), pp. 553–566.

[75] Texakalidis, P., Hilditch, C. A., Lehman, V., Lanzino, G., Pereira, V. M., and Brinjikji, W., 2018, "Vessel Wall Imaging of Intracranial Aneurysms: Systematic Review and Meta-Analysis," World Neurosurg., **117**, pp. 453–458.

[76] Wang, G., Li, W., Lei, S., Ge, X. dong, Yin, J. bo, and Zhang, D., 2019, "Relationships between Aneurysmal Wall Enhancement and Conventional Risk Factors in Patients with Intracranial Aneurysm: A High-Resolution MRI Study," J. Neuroradiol., **46**(1), pp. 25–28.

[77] Quan, K., Song, J., Yang, Z., Wang, D., An, Q., Huang, L., Liu, P., Li, P., Tian, Y., Zhou, L., and Zhu, W., 2019, "Validation of Wall Enhancement as a New Imaging Biomarker of Unruptured Cerebral Aneurysm," Stroke, **50**(6), pp. 1570–1573.

[78] Vakil, P., Ansari, S. A., Cantrell, C. G., Eddleman, C. S., Dehkordi, F. H., Vranic, J., Hurley, M. C., Batjer, H. H., Bendok, B. R., and Carroll, T. J., 2015, "Quantifying Intracranial Aneurysm Wall Permeability for Risk Assessment Using Dynamic Contrast-Enhanced MRI: A Pilot Study," AJNR. Am. J. Neuroradiol., **36**(5), pp. 953–959.

[79] King, R. M., Marosfoi, M., Caroff, J., Ughi, G. J., Groth, D. M., Gounis, M. J., and Puri, A. S., 2019, "High Frequency Optical Coherence Tomography Assessment of Homogenous Neck Coverage by Intrasaccular Devices Predicts Successful Aneurysm Occlusion," J. Neurointerv. Surg., **11**(11), pp. 1150–1154.

[80] Hartmann, K., Stein, K. P., Neyazi, B., and Erol Sandalcioglu, I., 2019, "Aneurysm Architecture: First in Vivo Imaging of Human Cerebral Aneurysms with Extravascular Optical Coherence Tomography," Cerebrovasc. Dis., **48**(1–2), pp. 26–31.

[81] Robertson, A. M., and Watton, P. N., 2013, "Mechanobiology of the Arterial Wall," *Transport in Biological Media*, S. Becker, and A. Kuznetsov, eds., Elsevier, New York, pp. 275–347.

[82] Stehbens, W. E., 1963, "Histopathology of Cerebral Aneurysms," Arch. Neurol., **8**(3), pp. 272–285.

[83] Yong-Zhong, G., and Van Alphen, H. A. M., 1990, "Pathogenesis and Histopathology of Saccular Aneurysms: Review of the Literatutre," Neurol. Res., **12**(4), pp. 249–255.

[84] Schneiders, J. J., Marquering, H. A., Van Den Berg, R., VanBavel, E., Velthuis, B., Rinkel, G. J. E., and Majoie, C. B., 2014, "Rupture-Associated Changes of Cerebral Aneurysm Geometry: High-Resolution 3D Imaging before and after Rupture," Am. J. Neuroradiol., **35**(7), pp. 1358–1362.

[85] Vlak, M. H. M., Rinkel, G. J. E., Greebe, P., Van Der Bom, J. G., and Algra, A., 2011, "Trigger Factors and Their Attributable Risk for Rupture of Intracranial Aneurysms: A Case-Crossover Study," Stroke, **42**(7), pp. 1878–1882.

[86] Björkman, J., Frösen, J., Tähtinen, O., Backes, D., Huttunen, T., Harju, J., Huttunen, J., Kurki, M. I., Von Und Zu Fraunberg, M., Koivisto, T., Manninen, H., Jääskeläinen, J. E., and Lindgren, A. E., 2017, "Irregular Shape Identifies Ruptured Intracranial Aneurysm in Subarachnoid Hemorrhage Patients with Multiple Aneurysms," Stroke, **48**(7), pp. 1986–1989.

[87] Humphrey, J. D., and Rajagopal, K., 2002, "A Constrained Mixture Model for Growth and Remodeling of Soft Tissues," Math. Model. Methods Appl. Sci., **12**(3), pp. 407–430.

[88] Baek, S., Rajagopal, K. R., and Humphrey, J. D., 2006, "A Theoretical Model of Enlarging Intracranial Fusiform Aneurysms," J. Biomech. Eng., **128**(1), p. 142.

[89] Watton, P. N., Ventikos, Y., and Holzapfel, G. A., 2009, "Modelling the Growth and Stabilization of Cerebral Aneurysms," Math. Med. Biol., **26**(2), pp. 133–164.

[90] Gade, P., 2019, "Coupled Theoretical and Experimental Methods to Understand Growth and Remodeling of In Situ Engineered Vascular Grafts in Young and Aged Hosts," Doctoral Dissertation, University of Pittsburgh.

[91] Khosravi, R., Miller, K. S., Best, C. A., Shih, Y. C., Lee, Y.-U., Yi, T., Shinoka, T., Breuer, C. K., and Humphrey, J. D., 2015, "Biomechanical Diversity Despite Mechanobiological Stability in Tissue Engineered Vascular Grafts Two Years Post-Implantation," Tissue Eng. Part A, **21**(9–10), pp. 1529–1538.

[92] Doillon, C. J., Dunn, M. G., Bender, E., and Silver, F. H., 1985, "Collagen Fiber Formation in Repair Tissue: Development of Strength and Toughness," Coll. Relat. Res., **5**(6), pp. 481–492.

[93] Zeng, Z., Kallmes, D. F., Durka, M. J., Ding, Y., Lewis, D., Kadirvel, R., and Robertson, A. M., 2011, "Hemodynamics and Anatomy of Elastase-Induced Rabbit Aneurysm Models: Similarity to Human Cerebral Aneurysms?," Am. J. Neuroradiol., **32**(3), pp. 595–601.

[94] Wang, S., Dai, D., Kolumam Parameswaran, P., Kadirvel, R., Ding, Y.-H., Robertson, A. M., and Kallmes, D. F., 2018, "Rabbit Aneurysm Models Mimic Histologic Wall Types Identified in Human Intracranial Aneurysms," J. Neurointerv. Surg., **10**(4), pp. 411–415.

[95] Altes, T. A., Cloft, H. J., Short, J. G., DeGast, A., Do, H. M., Helm, G. A., and Kallmes, D. F., 2000, "Creation of Saccular Aneurysms in the Rabbit," Am. J. Roentgenol., **174**(2), pp. 349–354.

[96] Cheng, F., Birder, L. A., Kullmann, F. A., Hornsby, J., Watton, P. N., Watkins, S., Thompson, M., and Robertson, A. M., 2018, "Layer-Dependent Role of Collagen Recruitment during Loading of the Rat Bladder Wall," Biomech. Model. Mechanobiol., **17**(2), pp. 403–417.

[97] Humphrey, J. D., and Canham, P. B., 2000, "Structure, Mechanical Properties, and Mechanics of Intracranial Saccular Aneurysms," J. Elast., **61**(1–3), pp. 49–81.

[98] Bredfeldt, J. S., Liu, Y., Pehlke, C. A., Conklin, M. W., Szulczewski, J. M., Inman, D. R., Keely, P. J., Nowak, R. D., Mackie, T. R., and Eliceiri, K. W., 2014, "Computational Segmentation of Collagen Fibers from Second-Harmonic Generation Images of Breast Cancer," J. Biomed. Opt., **19**(1), p. 016007.

[99] Liu, Y., Keikhosravi, A., Mehta, G. S., Drifka, C. R., and Eliceiri, K. W., 2017, "Methods for Quantifying Fibrillar Collagen Alignment," *Fibrosis*, L. Rittié, ed., Humana Press, New York, NY, pp. 429–451.

[100] Sander, E. A., and Barocas, V. H., 2009, "Comparison of 2D Fiber Network Orientation Measurement Methods," J. Biomed. Mater. Res. - Part A, **88**(2), pp. 322–331.

[101] Parshin, D. V., Lipovka, A. I., Yunoshev, A. S., Ovsyannikov, K. S., Dubovoy, A. V., and Chupakhin, A. P., 2019, "On the Optimal Choice of a Hyperelastic Model of Ruptured and Unruptured Cerebral Aneurysm," Sci. Rep., **9**(1), pp. 1–11.

[102] Raghavan, M. L., Kratzberg, J., Castro de Tolosa, E. M., Hanaoka, M. M., Walker, P., and da Silva, E. S., 2006, "Regional Distribution of Wall Thickness and Failure Properties of Human Abdominal Aortic Aneurysm," J. Biomech., **39**(16), pp. 3010–3016.

[103] Lu, J., Hu, S., and Raghavan, M. L., 2013, "A Shell-Based Inverse Approach of Stress Analysis in Intracranial Aneurysms," Ann. Biomed. Eng., **41**(7), pp. 1505–1515.

[104] Miller, K., and Lu, J., 2013, "On the Prospect of Patient-Specific Biomechanics without Patient-Specific Properties of Tissues," J. Mech. Behav. Biomed. Mater., **27**, pp. 154–166.

[105] Betsch, P., Gruttmann, F., and Stein, E., 1996, "A 4-Node Finite Shell Element for the Implementation of General Hyperelastic 3D-Elasticity at Finite Strains," Comput. Methods Appl. Mech. Eng., **130**(1–2), pp. 57–79.

[106] Maas, S. A., Ellis, B. J., Ateshian, G. A., and Weiss, J. A., 2012, "FEBio: Finite Elements for Biomechanics," J. Biomech. Eng., **134**(1), p. 011005.

[107] Kurashina, T., Sakamaki, T., Yagi, A., and Nakamura, Tetsuya Sakamoto, Hironosuke Nushiro, N., 1994, "A New Device for Indirect Blood Pressure Measurement in Rabbits," Jpn. Circ. J., **58**(4), pp. 264–268.

[108] Lanir, Y., 1994, "Plausibility of Structral Constitutive Equations for Isotropic Soft Tissues in Finite Static Deformations," J. Appl. Mech., **61**(3), pp. 695–702.

[109] Schriefl, A. J., Reinisch, A. J., Sankaran, S., Pierce, D. M., and Holzapfel, G. A., 2012, "Quantitative Assessment of Collagen Fibre Orientations from Two-Dimensional Images of Soft Biological Tissues," J. R. Soc. Interface, **9**(76), pp. 3081–3093.

[110] Wulandana, R., and Robertson, A. M., 2005, "An Inelastic Multi-Mechanism Constitutive Equation for Cerebral Arterial Tissue," Biomech. Model. Mechanobiol., **4**(4), pp. 235–248.

[111] Li, D., and Robertson, A. M., 2009, "A Structural Multi-Mechanism Constitutive Equation for Cerebral Arterial Tissue," Int. J. Solids Struct., **46**(14–15), pp. 2920–2928.

[112] Cebral, J. R., and Raschi, M., 2013, "Suggested Connections between Risk Factors of Intracranial Aneurysms: A Review," Ann. Biomed. Eng., **41**(7), pp. 1366–1383.

[113] Watton, P. N., Selimovic, A., Raberger, N. B., Huang, P., Holzapfel, G. A., and Ventikos, Y., 2011, "Modelling Evolution and the Evolving Mechanical Environment of Saccular Cerebral Aneurysms," Biomech. Model. Mechanobiol., **10**(1), pp. 109–132.

[114] Zeinali-Davarani, S., Chow, M.-J., Turcotte, R., and Zhang, Y., 2013, "Characterization of Biaxial Mechanical Behavior of Porcine Aorta under Gradual Elastin Degradation.," Ann. Biomed. Eng., **41**(7), pp. 1528–38.

[115] Langille, B. L., Bendeck, M. P., and Keeley, F. W., 1989, "Adaptations of Carotid Arteries of Young and Mature Rabbits to Reduced Carotid Blood Flow," Am. J. Physiol. Circ. Physiol., **256**(4), pp. H931–H939.

[116] Hayashi, K., Makino, A., and Kakoi, D., 2018, "Remodeling of Arterial Wall : Response to Changes in Both Blood Flow and Blood Pressure," J. Mech. Behav. Biomed. Mater., **77**, pp. 475–484.

[117] Jackson, Z. S., Gotlieb, A. I., and Langille, B. L., 2002, "Wall Tissue Remodeling Regulates Longitudinal Tension in Arteries.," Circ. Res., **90**(8), pp. 918–925.

[118] Gleason, R. L., Wilson, E., and Humphrey, J. D., 2007, "Biaxial Biomechanical Adaptations of Mouse Carotid Arteries Cultured at Altered Axial Extension," J. Biomech., **40**(4), pp. 766–776.

[119] Cicchi, R., Pavone, F. S., Massi, D., and Sampson, D. D., 2005, "Contrast and Depth Enhancement in Two-Photon Microscopy of Human Skin Ex Vivo by Use of Optical Clearing Agents," Opt. Express, **13**(7), p. 2337.

[120] Genina, E. A., Bashkatov, A. N., and Tuchin, V. V., 2010, "Tissue Optical Immersion Clearing," Expert Rev. Med. Devices, **7**(6), pp. 825–842.

[121] Marosfoi, M., Langan, E. T., Strittmatter, L., Van Der Marel, K., Vedantham, S., Arends, J., Lylyk, I. R., Loganathan, S., Hendricks, G. M., Szikora, I., Puri, A. S., Wakhloo, A. K., and Gounis, M. J., 2017, "In Situ Tissue Engineering: Endothelial Growth Patterns as a Function of Flow Diverter Design," J. Neurointerv. Surg., **9**(10), pp. 994–998.

[122] Kallmes, D. F., Ding, Y. H., Dai, D., Kadirvel, R., Lewis, D. A., and Cloft, H. J., 2007, "A New Endoluminal, Flow-Disrupting Device for Treatment of Saccular Aneurysms," Stroke, **38**(8), pp. 2346–2352.

[123] Ravindran, K., Casabella, A. M., Cebral, J., Brinjikji, W., Kallmes, D. F., and Kadirvel, R., 2020, "Mechanism of Action and Biology of Flow Diverters in the Treatment of Intracranial Aneurysms," Neurosurgery, **86**(1), pp. S13–S19.

[124] Amann, K., 2008, "Media Calcification and Intima Calcification Are Distinct Entities in Chronic Kidney Disease," Clin. J. Am. Soc. Nephrol., **3**(6), pp. 1599–1605.

[125] Daniela, Q., Federica, B., and Lofaro, F. D., 2020, "The Biology of Vascular Calcification," Int. Rev. Cell Mol. Biol., **354**.

[126] Demer, L. L., and Tintut, Y., 2014, "Inflammatory, Metabolic, and Genetic Mechanisms of Vascular Calcification," Arterioscler. Thromb. Vasc. Biol., **34**(4), pp. 715–723.

[127] Stary, H. C., 2000, "Natural History and Histological Classification of Atherosclerotic Lesions an Update," Arterioscler. Thromb. Vasc. Biol., **20**(5), pp. 1177–1178.

[128] Lanzer, P., Boehm, M., Sorribas, V., Thiriet, M., Janzen, J., Zeller, T., St Hilaire, C., and Shanahan, C., 2014, "Medial Vascular Calcification Revisited: Review and Perspectives," Eur. Heart J., **35**(23), pp. 1515–1525.

[129] O'Neill, W. C., Han, K. H., Schneider, T. M., and Hennigar, R. A., 2015, "Prevalence of Nonatheromatous Lesions in Peripheral Arterial Disease," Arterioscler. Thromb. Vasc. Biol., **35**(2), pp. 439–447.

[130] Kemmeren, J. M., Van Noord, P. A. H., Beijerinck, D., Fracheboud, J., Banga, J. D., and Van der Graaf, Y., 1998, "Arterial Calcification Found on Breast Cancer Screening Mammograms and Cardiovascular Mortality in Women the Dom Project," Am. J. Epidemiol., **147**(4), pp. 333–341.

[131] Iribarren, C., Sidney, S., Sternfeld, B., and Browner, W. S., 2000, "Calcification of the Aortic Arch: Risk Factors and Association with Coronary Heart Disease, Stroke, and Peripheral Vascular Disease," J. Am. Med. Assoc., **283**(21), pp. 2810–2815.

[132] Hollander, M., Hak, A. E., Koudstaal, P. J., Bots, M. L., Grobbee, D. E., Hofman, A., Witteman, J. C. M., and Breteler, M. M. B., 2003, "Comparison between Measures of Atherosclerosis and Risk of Stroke: The Rotterdam Study," Stroke, **34**(10), pp. 2367–2372.

[133] Wayhs, R., Zelinger, A., and Raggi, P., 2002, "High Coronary Artery Calcium Scores Pose an Extremely Elevated Risk for Hard Events," J. Am. Coll. Cardiol., **39**(2), pp. 225–230.

[134] Rennenberg, R. J. M. W., Kessels, A. G. H., Schurgers, L. J., Van Engelshoven, J. M. A., De Leeuw, P. W., and Kroon, A. A., 2009, "Vascular Calcifications as a Marker of Increased Cardiovascular Risk: A Meta-Analysis," Vasc. Health Risk Manag., **5**, pp. 185–197.

[135] Bos, D., Portegies, M. L. P., Van Der Lugt, A., Bos, M. J., Koudstaal, P. J., Hofman, A., Krestin, G. P., Franco, O. H., Vernooij, M. W., and Ikram, M. A., 2014, "Intracranial Carotid Artery Atherosclerosis and the Risk of Stroke in Whites: The Rotterdam Study," JAMA Neurol., **71**(4), pp. 405–411.

[136] Buijs, R. V. C., Willems, T. P., Tio, R. A., Boersma, H. H., Tielliu, I. F. J., Slart, R. H. J. A., and Zeebregts, C. J., 2013, "Calcification as a Risk Factor for Rupture of Abdominal Aortic Aneurysm," Eur. J. Vasc. Endovasc. Surg., **46**(5), pp. 542–548.

[137] Volokh, K. Y., and Aboudi, J., 2016, "Aneurysm Strength Can Decrease under Calcification.," J. Mech. Behav. Biomed. Mater., **57**, pp. 164–74.

[138] Sakaguchi, M., Hasegawa, T., Ehara, S., Matsumoto, K., Mizutani, K., Iguchi, T., Ishii, H., Nakagawa, M., Shimada, K., and Yoshiyama, M., 2016, "New Insights into Spotty Calcification and Plaque Rupture in Acute Coronary Syndrome: An Optical Coherence Tomography Study," Heart Vessels, **31**(12), pp. 1915–1922.

[139] Nerlekar, N., Ha, F. J., Cheshire, C., Rashid, H., Cameron, J. D., Wong, D. T., Seneviratne, S., and Brown, A. J., 2018, "Computed Tomographic Coronary Angiography-Derived Plaque Characteristics Predict Major Adverse Cardiovascular Events: A Systematic Review and Meta-Analysis," Circ. Cardiovasc. Imaging, **11**(1), p. e006973.

[140] Vengrenyuk, Y., Carlier, S., Xanthos, S., Cardoso, L., Ganatos, P., Virmani, R., Einav, S., Gilchrist, L., and Weinbaum, S., 2006, "A Hypothesis for Vulnerable Plaque Rupture Due to Stress-Induced Debonding around Cellular Microcalcifications in Thin Fibrous Caps.," Proc. Natl. Acad. Sci. U. S. A., **103**(40), pp. 14678–83.

[141] Barrett, H. E., Van der Heiden, K., Farrell, E., Gijsen, F. J. H., and Akyildiz, A. C., 2019, "Calcifications in Atherosclerotic Plaques and Impact on Plaques Biomechanics," J. Biomech., **87**(April), pp. 1–12.

[142] Kelly-Arnold, A., Maldonado, N., Laudier, D., Aikawa, E., Cardoso, L., and Weinbaum, S., 2013, "Revised Microcalcification Hypothesis for Fibrous Cap Rupture in Human Coronary Arteries," Proc. Natl. Acad. Sci., **110**(26), pp. 10741–10746.

[143] Yilmaz, A., Akpinar, E., Topcuoglu, M. A., and Arsava, E. M., 2015, "Clinical and Imaging Features Associated with Intracranial Internal Carotid Artery Calcifications in Patients with Ischemic Stroke," Neuroradiology, **57**(5), pp. 501–506.

[144] Kockelkoren, R., Vos, A., Hecke, W. Van, Vink, A., Bleys, R. L. A. W., Verdoorn, D., Mali, W. P. T. M., Hendrikse, J., Koek, H. L., De Jong, P. A., and De Vis, J. B., 2017, "Computed Tomographic Distinction of Intimal and Medial Calcification in the Intracranial Internal Carotid Artery," PLoS One, **12**(1), pp. 1–11.

[145] Vos, A., Van Hecke, W., Spliet, W. G. M., Goldschmeding, R., Isgum, I., Kockelkoren, R., Bleys, R. L. A. W., Mali, W. P. T. M., De Jong, P. A., and Vink, A., 2016, "Predominance of Nonatherosclerotic Internal Elastic Lamina Calcification in the Intracranial Internal Carotid Artery," Stroke, **47**(1), pp. 221–223.

[146] Gade, P. S., Robertson, A. M., and Chuang, C. Y., 2019, "Multiphoton Imaging of Collagen, Elastin, and Calcification in Intact Soft-Tissue Samples," Curr. Protoc. Cytom., **87**(1), pp. 1–14.

[147] Golshani, K., Ferrell, A., Zomorodi, A., Smith, T., and Britz, G., 2010, "A Review of the Management of Posterior Communicating Artery Aneurysms in the Modern Era," Surg. Neurol. Int., **1**, p. 88.

[148] Gupta, S. K., Khosla, V. K., Chhabra, R., Mohindra, S., Bapuraj, J. R., Khandelwal, N., Mukherjee, K. K., Tewari, M. K., Pathak, A., and Mathuriya, S. N., 2007, "Internal Carotid Artery Bifurcation Aneurysms: Surgical Experience," Neurol. Med. Chir. (Tokyo)., **47**(4), pp. 153–157.

[149] Van Rooij, W. J., Sluzewski, M., and Beute, G. N., 2008, "Internal Carotid Bifurcation Aneurysms: Frequency, Angiographic Anatomy and Results of Coiling in 50 Aneurysms," Neuroradiology, **50**(7), pp. 583–587.

[150] Lehecka, M., Dashti, R., Romani, R., Çelik, Ö., Navratil, O., Kivipelto, L., Kivisaari, R., Shen, H., Ishii, K., Karatas, A., Lehto, H., Kokuzawa, J., Niemelä, M., Rinne, J., Ronkainen, A., Koivisto, T., Jääskelainen, J. E., and Hernesniemi, J., 2009, "Microneurosurgical Management of Internal Carotid Artery Bifurcation Aneurysms," Surg. Neurol., **71**(6), pp. 649–667.

[151] Cebral, J. R., Mut, F., Gade, P., Cheng, F., Tobe, Y., Frosen, J., and Robertson, A. M., 2018, "Combining Data from Multiple Sources to Study Mechanisms of Aneurysm Disease: Tools and Techniques," Int. j. numer. method. biomed. eng., **34**(11).

[152] Antiga, L., Piccinelli, M., Botti, L., Ene-Iordache, B., Remuzzi, A., and Steinman, D. A., 2008, "An Image-Based Modeling Framework for Patient-Specific Computational Hemodynamics," Med. Biol. Eng. Comput., **46**(11), pp. 1097–1112.

[153] Antiga, L., and Steinman, D. A., 2004, "Robust and Objective Decomposition and Mapping of Bifurcating Vessels," IEEE Trans. Med. Imaging, **23**(6), pp. 704–713.

[154] Krabbe-Hartkamp, M. J., van der Grond, J., de Leeuw, F. E., de Groot, J. C., Algra, A., Hillen, B., Breteler, M. M. B., and Mali, W. P. T. M., 1998, "Circle of Willis: Morphologic Variation on Three-Dimensional Time-of-Flight MR Angiograms.," Radiology, **207**(1), pp. 103–111.

[155] Kamath, S., 1981, "Observations on the Length and Diameter of Vessels Forming the Circle of Willis," J. Anat., **133**(Pt 3), pp. 419–423.

[156] Ramezanpour, M., Fortunato, R. N., Sang, C., Maiti, S., and Robertson, A. M., 2020, "Quantitative Analysis of Arterial Calcifications and Lipid Pools: A Set of High-Fidelity Protocols."

[157] Newman, A. B., Naydeck, B. L., Sutton-tyrrell, K., Feldman, A., Edmundowicz, D., and Kuller, L. H., 2001, "Coronary Artery Calcification in Older Adults to Age 99 Prevalence and Risk Factors."

[158] McClelland, R. L., Chung, H., Detrano, R., Post, W., and Kronmal, R. A., 2006, "Distribution of Coronary Artery Calcium by Race, Gender, and Age: Results from the Multi-Ethnic Study of Atherosclerosis (MESA)," Circulation, **113**(1), pp. 30–37.

[159] Leopold, J. A., 2013, "Vascular Calcification an Age-Old Problem of Old Age," Circulation, **127**(24), pp. 2380–2382.

[160] Chung, B. J., Doddasomayajula, R., Mut, F., Detmer, F., Pritz, M. B., Hamzei-Sichani, F., Brinjikji, W., Kallmes, D. F., Jimenez, C. M., Putman, C. M., and Cebral, J. R., 2017, "Angioarchitectures and Hemodynamic Characteristics of Posterior Communicating Artery Aneurysms and Their Association with Rupture Status," Am. J. Neuroradiol., **38**(11), pp. 2111–2118.

[161] Fortunato, R. N., Robertson, A. M., Sang, C., Duan, X., and Maiti, S., 2020, "Effect of Macro-Calcification on the Failure Mechanics of Intracranial Aneurysmal Wall Tissue," Exp. Mech.

[162] Mardia, K. V., and Jupp, P. E., 2000, *Directional Statistics*, John Wiley & Sons, New York.

[163] Freed, A. D., 2008, "Anisotropy in Hypoelastic Soft-Tissue Mechanics, I: Theory," J. Mech. Mater. Struct., **3**(5), pp. 911–928.